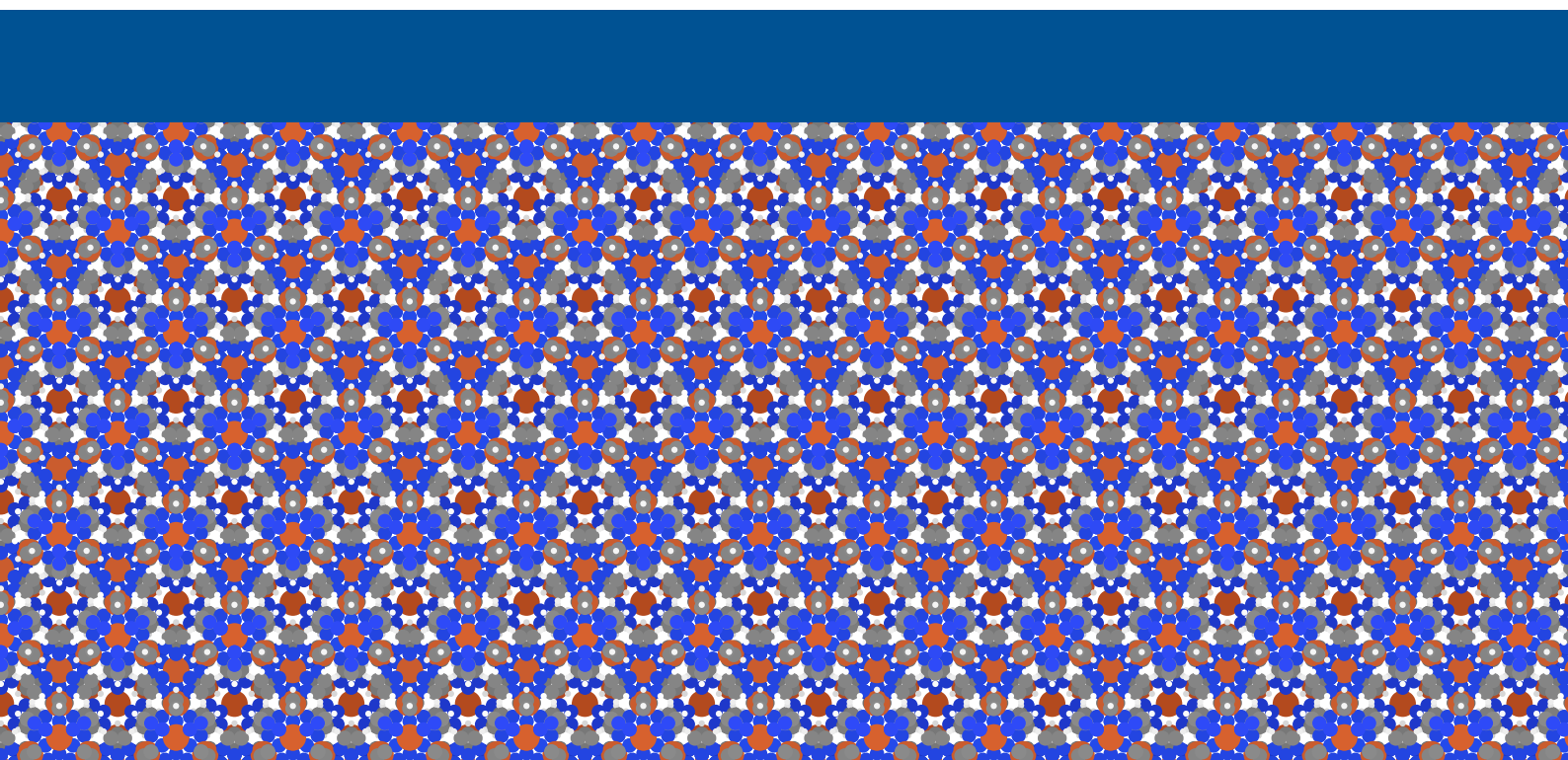


Technische Universität München
Fakultät für Chemie
Lehrstuhl für Theoretische Chemie

On the Charge Carrier Mobility and its Underlying Material Properties in the Context of Metal-Organic Frameworks

Christoph Johannes Muschielok

Dissertation





Technische Universität München
Fakultät für Chemie
Lehrstuhl für Theoretische Chemie

On the Charge Carrier Mobility and its Underlying Material Properties in the Context of Metal-Organic Frameworks

Christoph Johannes Muschielok

Vollständiger Abdruck der von der Fakultät für Chemie der Technischen Universität München zur Erlangung des akademischen Grades eines

Doktors der Naturwissenschaften (Dr. rer. nat.)

genehmigten Dissertation.

Vorsitzender: Prof. Dr. Karsten Reuter

Prüfer der Dissertation:

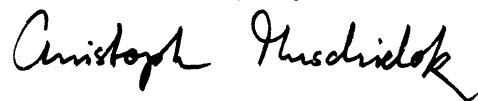
1. Priv.-Doz. Dr. Harald Oberhofer
2. Prof. Dr. Achim Wixforth (Universität Augsburg)

Die Dissertation wurde am 25.05.2020 bei der Technischen Universität München eingereicht und durch die Fakultät für Chemie am 06.07.2020 angenommen.

Preface

All work presented in this doctoral thesis was performed between October 2016 and April 2020 at the Chair of Theoretical Chemistry of the Technical University of Munich (TUM), under the supervision of PD Dr. Harald Oberhofer. Parts of this dissertation have been published before in ref. [1].

Hausham, May 2020

A handwritten signature in black ink, reading "Christoph Muschielok". The signature is written in a cursive style with a prominent loop at the end of the last name.

Christoph Muschielok

Abstract

Metal-organic frameworks (MOFs) are (poly-)crystalline compounds which consist of metal centers or nodes coordinated by organic ligands called linkers. They often show permanent porosity. As these network-like compounds tend to self-assemble, the molecular building blocks can be chosen to downright design certain features of the MOF. Considering the vast design space offered by the possible metal centers organic molecules, it seems peculiar that only a minority of MOFs shows electrical conductivity. To begin to understand, why this is the case, the physical quantities underlying the conductivity are studied exemplarily for the family of metal triazoles, $M(\text{ta})_2$. Considering the large band gaps of many pristine MOFs and in particular of the $M(\text{ta})_2$ crystals, one assumes that one of the quantities necessary for a non-zero conductivity, namely a non-zero mobile charge carrier density, is ascribed to defects in the real crystal. As the conductivity is given as the product of this density and the charge carrier mobility, through this hypothesis it is possible to focus on the latter, where the Bardeen–Shockley deformation potential theory is used to give an upper limit expression for the mobility. The in-depth study thus focusses on the three material parameters which appear in the Bardeen–Shockley mobility. First, the effective mass of the charge carriers in the crystal which measures their delocalization. Second, the bulk modulus, measuring the stiffness of the crystal and the group velocity of the acoustic phonons therein. Third, the deformation potential which measures an effective coupling between the charge carriers and the (acoustic) phonons in the crystal. In a first theoretical study, the effect of metal center substitution is studied under the premise that the differing Lewis acidity and thus polarizability of the metal atoms changes the electronic coupling elements influencing the band dispersion and thus the effective mass. The metal triazoles used therefore, are iron, zinc, and ruthenium triazolate. The former two are known to exhibit a finite electrical conductivity or being an electrical isolator respectively. The ruthenium triazolate crystal, which so far has not been synthesized, is predicted to have an even better conductivity compared to $\text{Fe}(\text{ta})_2$. A second study then looks at the influence of different weakly interacting gases (argon and carbon dioxide) on the mobility descriptors in a $\text{Fe}(\text{ta})_2$ crystal. It could be shown that the main effect of such an absorption is a change of the deformation potential. This may suggest a negative effect which weakly bound absorbates, also commonly found in air, could have on the electrical conductivity. In a short third study, it is realized that the arguments brought forward so far for the explicit crystalline framework may be taken to a much simpler metal-linker surrogate model which emphasizes the importance of different aspects of the metal-linker bond in the description of the three Bardeen–Shockley mobility descriptors.

Zusammenfassung

Metallorganische Gerüstverbindungen (metal-organic frameworks, MOFs) sind (poly-)kristalline, oft permanent poröse Verbindungen, die sich aus Metallzentren, welche durch organische Liganden (Linker) koordiniert werden. Die Synthese erfolgt meist aus einer die Metallspezies enthaltenden Vorstufe und den Linkerverbindungen durch Selbstassemblierung. Dieses Zusammensetzen molekularer Bausteine lässt sich zum gezielten Entwerfen bestimmter MOF-Eigenschaften nutzen. Bei der zur Verfügung stehenden Vielfalt an Metall-Linker-Kombinationen, ist es erstaunlich, dass aus dieser Masse an Gerüstverbindungen bisher nur einige wenige elektrische Leitfähigkeit zeigen. Um zu verstehen, warum dies so ist, werden im Folgenden die der elektrischen Leitfähigkeit zugrundeliegenden physikalischen Größen untersucht. Dies geschieht am Beispiel der kubischen Metall(II)-triazolate, $M(\text{ta})_2$, insbesondere dem Eisen(II)-triazolat. Die elektrische Leitfähigkeit hängt direkt von zwei Größen ab: der mobilen Ladungsträgerdichte und ihrer Beweglichkeit oder Mobilität. Erstere ist durch eine Bandlücke von mehreren Elektronvolt für die idealen $M(\text{ta})_2$ -Kristalle bei Raumtemperatur null. Daher wird auf die Hypothese zurückgegriffen, dass im realen Material die mobilen Ladungsträger durch unterschiedliche Defekte in der Kristallstruktur eingeführt werden. Dies erlaubt es weiters nurmehr Argumente bezüglich der Mobilität vorzubringen. Hierfür wird der Ausdruck verwendet, welcher sich aus der Deformationspotentialtheorie von Bardeen und Shockley ergibt. Daraus folgt eine Abhängigkeit der Mobilität von drei Größen: Erstens von der effektiven Masse der mobilen Ladungsträger, welche ein Maß für die Delokalisation der mobilen Ladungsträger ist. Zweitens vom Kompressionsmodul des Kristalls, welche die mechische Belastbarkeit und eine effektive Gruppengeschwindigkeit der akustischen Phononen angibt. Drittens vom Deformationspotential, welches eine effektive Kopplung zwischen den Ladungsträgern und den (akustischen) Phononen misst. Untersucht werden die Einflüsse auf diese drei Deskriptoren durch den Austausch der Metallzentren einerseits und durch Absorption schwach wechselwirkender Gase in die MOF-Poren andererseits. Für die Mobilität können so experimentelle Befunde für die Leitfähigkeit von $\text{Fe}(\text{ta})_2$ (leitet bei Raumtemperatur) und $\text{Zn}(\text{ta})_2$ (elektrischer Isolator) reproduziert werden. Für $\text{Ru}(\text{ta})_2$, wird eine noch größere Mobilität vorhergesagt als für $\text{Fe}(\text{ta})_2$. Diese Effekte sind hauptsächlich bedingt durch eine Änderung der effektiven Masse. Unter Gasabsorption zeigt sich für $\text{Fe}(\text{ta})_2$ ein negativer Effekt von physisorbiertem Gas auf die Mobilität durch eine Erhöhung des Deformationspotentials. Dies könnte auf einen starken Einfluss jeglicher Atmosphäre auf Leitfähigkeitsmessungen bei MOFs hindeuten. Abschließend werden die Überlegungen, die für die einzelnen Netzwerke angestellt wurden, auf ein Komplex-Ersatzmodell übertragen und die besondere Rolle verschiedener Eigenschaften der Metall-Linker-Bindung im Hinblick auf die drei Deskriptoren diskutiert.

Contents

1	Introduction	1
2	Theoretical Background	5
2.1	The many-body problem of the solid	5
2.2	Density-functional theory	7
2.2.1	Reformulating the electronic many-body problem	7
2.2.2	Approximating the exchange-correlation functional	9
2.2.3	Self-interaction error in Kohn–Sham density-functional theory	10
2.3	Lattices and the Bloch theorem	10
2.3.1	Bravais lattices	11
2.3.2	The reciprocal lattice	11
2.3.3	Bloch’s theorem	12
2.4	Introduction to the theory of the harmonic solid	13
2.4.1	Classical theory of lattice vibrations	13
2.4.2	Classical theory of elasticity	17
2.4.3	Hydrostatic deformation	18
2.4.4	Quantization of the collective excitations	19
2.5	Semiclassical electron motion and the effective mass	20
2.5.1	Quasiclassical equations of motion	20
2.5.2	Effective mass tensor	21
2.5.3	Angular effective mass	22
2.6	Electron-phonon coupling	23
2.6.1	Deformation potential coupling	23
2.6.2	Coupling matrix elements and transition rates	26
2.7	Charge transport	29
2.7.1	Transition probabilities and Boltzmann equation	29
2.7.2	The relaxation time approximation	31
2.7.3	The Bardeen–Shockley relaxation time	31
2.7.4	A generalization of the Bardeen–Shockley relaxation time	33
2.7.5	Conductivity and mobility	36
2.7.6	Mobility and relaxation time	38

3	Metal-organic frameworks	41
3.1	A versatile family of compounds	41
3.2	Electrical conductivity in metal-organic framework crystals	42
4	Aspects of semiconductivity in soft, porous, metal-organic framework crystals	45
4.1	Methodology	45
4.1.1	Computational details	45
4.1.2	Generation of the crystal structures	46
4.1.3	Band structure calculations and the mean effective mass	46
4.1.4	Elasticity and deformation potential tensors	47
4.2	Results and discussion	52
4.2.1	Carrier effective masses in $M(\text{ta})_2$	55
4.2.2	$M(\text{ta})_2$ crystal stiffness	55
4.2.3	Effective carrier-phonon coupling in $M(\text{ta})_2$	58
4.3	Conclusions	59
5	Influence of Gas Absorption on the Charge Mobility and its Descriptors in Iron Triazolate	61
5.1	Methodology	62
5.1.1	Bulk modulus from hydrostatic deformations	62
5.1.2	First and second order deformation potentials from hydrostatic deformations	63
5.1.3	Sampling the geometric pore structure of a metal-organic framework (MOF)	63
5.1.4	Higher-order samplings of a pore	65
5.1.5	Density-Functional Theory	66
5.1.6	Generation of the Absorbate Structures	66
5.2	Results and discussion	67
5.2.1	Sampling of $\mathcal{M}_1(G, \text{Fe}(\text{ta})_2)$	67
5.2.2	Absorption energies of CO_2 and Ar in $\text{Fe}(\text{ta})_2$	69
5.2.3	Absorbate influence on the elasticity	70
5.2.4	Densities of states and deformation potential	71
5.2.5	Effective Masses	74
5.3	Conclusion and outlook	74
6	Pseudo-inverse error cancellation and apparent coupling constants	79
6.1	Compensating for the quadratic coupling error in the pseudo-inverse method . .	79
6.2	Why some deformation potentials seem to be small	81
6.3	Electron-phonon couplings from phonon displacement patterns—an outlook . . .	85
6.4	Conclusion	86
7	Overall Conclusions	87

Appendix I Highlights of density-functional theory	89
Exchange-correlation holes	89
The adiabatic connection formula	91
Appendix II Wannier functions and the equivalent Schrödinger equation	93
Wannier representation of the Schrödinger equation	93
Appendix III Notes on strain tensors and elasticity	97
Differences introduced through the deformation gradient	97
Total energy changes in cubic crystals	98
Appendix IV Introduction to quaternions	99
Bibliography	101
List of publications	107
Acknowledgements	109

List of Illustrations

Figures

2.1	Illustration of warped bands	22
3.1	Some general features of metal-organic frameworks.	42
4.1	Metal(II) (1,2,3)-triazolate structures	46
4.2	Workflow for the Bardeen–Shockley descriptors	52
4.3	Total energies for strained metal triazolate crystals	53
4.4	Band structures and densities of states for various metal triazolates	54
4.5	The warped conduction band minimum of $\text{Fe}(\text{ta})_2$ and $\text{Ru}(\text{ta})_2$	56
4.6	Angular effective mass plots for the different metal triazolates	57
4.7	Spider web plot of Bardeen–Shockley parameters	59
5.1	Illustration of the Boolean criterion	64
5.2	Low and high load absorbate structures	68
5.3	Pore identification	68
5.4	Some $\text{Fe}(\text{ta})_2$ absorbate structures	68
5.5	Total energies of the strained cell high load absorbate structures	70
5.6	Pore loading effects on the bulk modulus	70
5.7	Electronic and phononic densities of states for absorbate structures	72
5.8	Energetic band edge extremum shifts versus strain magnitude	73
5.9	Deformation potential couplings for the absorbate structures	73
5.10	Angular effective mass plots for different absorbate structures	75
5.11	Radar plots of Bardeen–Shockley descriptors for absorbate structures	76
5.12	Hole mobilities for the various absorbates	77
6.1	Band extremum shifts for different metal triazolate crystals	82
6.2	Projected densities of states for $\text{M}(\text{ta})_2$ crystals and $\text{Fe}(\text{ta})_2$ absorbates	83
6.3	Phonon band structures for iron triazolate and its high-loading CO_2 absorbate	83
6.4	Vicinal metal-nitrogen and nitrogen-nitrogen distances for $\text{Fe}(\text{ta})_2$ and $\text{Zn}(\text{ta})_2$	84

Tables

4.1 Band gaps and effective masses for the various metal triazolates	55
4.2 Bardeen–Shockley parameters and mobilities	55
4.3 Elastic constants for the different metal triazolate crystals	56
4.4 Deformation potential constants for the different metal triazolate crystals . .	58
5.1 Bardeen–Shockley parameters for absorbate structures	67
5.2 Pore centers for the Ar pore of $\text{Fe}(\text{ta})_2$	69
5.3 Absorption energies for Ar and CO_2 into $\text{Fe}(\text{ta})_2$	69
5.4 Cell constant of absorbate crystals	71
5.5 First and second order deformation potential couplings	71
5.6 Mobilities referenced to the mobility in the low loading structure.	78
6.1 Comparison of pseudo-inverse and least squares fitted couplings	81

List of Abbreviations

AU	atomic units	HEG	homogeneous electron gas
BE	Boltzmann equation	HF	Hartree–Fock
BET	Brunauer–Emmet–Teller	HK	Hohenberg–Kohn
BOA	Born–Oppenheimer approximation	HL	high loading
BS	Bardeen–Shockley	HSE	Heyd–Scuseria–Ernzerhof
BZ	Brillouin zone	IUPAC	International Union of Pure and Applied Chemistry
CB	conduction band	KS	Kohn–Sham
CBM	conduction band minimum	KS-DFT	Kohn–Sham density-functional theory
CSD	Cambridge Crystallographic Database	LA	longitudinal acoustic
DC	direct current	LDA	local density approximation
DFA	density-functional approximation	LL	low loading
DFT	density-functional theory	LSDA	local spin density approximation
DoF	degree of freedom	MB	many-body
DOS	density of states	MC	Monte Carlo
EoM	equation of motion	MOF	metal-organic framework
FCC	face-centered cubic	NAO	numeric atom-centered orbital
FF	force field	PBE	Perdew–Burke–Ernzerhof
GEA	gradient expansion approximation	PDOS	projected density of states
GGA	generalized gradient approximation	PLC	pore loading configuration
		RTA	relaxation time approximation
		SAM	self-assembled monolayer

SBU	secondary building unit	TS	Tkatchenko–Scheffler
SCF	self-consistent field	VB	valence band
SE	Schrödinger equation	VBM	valence band maximum
SI	international system of units	vdW	van der Waals
SIE	self-interaction error	WFT	wavefunction theory
TA	transversal acoustic	XC	exchange-correlation
TB	tight-binding		

1 Introduction

The coordinative bonding between metal centers and certain organic ligands with multiple coordination sites, can lead to the formation of self-assembled, net-like or framework compounds with permanent porosity[2–4], which are then called MOFs.[5] Utilizing this molecular building block principle, it has been possible to synthesize many thousands of different framework materials, most often designed for a specific purpose.[6, 7] The initial interest lying in gas sorption,[2–4, 8] has long since been expanded to many other fields of application, e. g. fuel cell membranes[9, 10] and catalyst materials[11, 12].

Another interesting application for MOFs, in particular with regards to their porosity, are chemical sensors.[13] Those can function in different ways, by exploiting different features of the sensor material and the analyte.[14] For example, a color change, or more generally the change of the absorption or emission spectrum, upon absorption of a compound into the MOF could indicate its presence in a substrate. Another possibility, is to exploit the change of electrical resistance or conductivity of a sensor material[15] under adsorption of an analyte onto the (inner) surface.

The latter approach requires at least some inherent conductivity in the sensor material, for the whole device to function. Unfortunately, within the vast design space of possible metal-linker combinations, only few *intrinsically* electrically conducting MOFs have been found so far.[16–18] One reason for this may also be that the active research interest in this area is only approximately ten years[19] old. Still, the number of publications in the field of electrically conducting MOFs is only in the order of magnitudes of hundreds.

One way to go is thus to find out the reasons, why MOFs so often are bad electrical conductors. At this point, this means semi-conductivity, so that a good intrinsic electrical conductor must have a high density of mobile charge carriers, which in turn have to show a high mobility.[20–22] For the latter to be analyzed more deeply, one has to assume some model for the charge transport mechanism. Oberhofer et al. have reviewed[23] theoretical models to describe the mobility of charge carriers in organic semiconductor crystals. They discuss that, concerning the localization of the charge carriers, there are two extremal regimes: one in which so-called hopping models are valid, where the charge carriers are localized on some site, and one governed by the band transport model, in which the charge carriers are assumed as delocalized. Furthermore, they state that the gross of such compounds will have to be treated within models using a partial delocalization of charge. However, they disclose that, irrespective of the choice of mechanism, the order of magnitude of the resulting mobility is comparable.

By means of this, one can argue that although mobile charge carriers in an average MOF would be expected to be rather localized, one can estimate their mobility by using a band transport model. Note, that this choice is not made deliberately. It gives the freedom to not choose localization sites for the mobile charge carriers, which is, given the potentially three-dimensional network of a MOF, not as straightforward as for e. g. a molecular crystal bound by van der Waals (vdW) forces, where each molecule can be easily used as a center.

Within a continuum model of a three-dimensional solid, the mobility in the band-transport regime is given by an expression[23, 24] first derived by Bardeen and Shockley for classic semiconductors like silicon or germanium. This was done in the course of developing a simple theory of electron-phonon coupling, commonly called deformation potential theory.[24, 25] In this model, the charge carrier mobility is governed by an effective electron-phonon coupling, the eponymous deformation potential, the effective mass of the carrier particle, and the bulk modulus of the semiconductor crystal. A high mobility semiconductor has a high bulk modulus, its charge carriers have a low effective mass, and their effective coupling to the phonons of the crystal should be weak.

The compound-wise focus of this work lies on the family of transition metal(II) (1,2,3)-triazolate crystals, $M(\text{ta})_2$, of which the iron compound has been shown experimentally by others[26] to exhibit a finite electrical conductivity. That is, for $\text{Fe}(\text{ta})_2$, a conductivity of $1 \times 10^{-6} \text{ S cm}^{-1}$ at 300 K under nitrogen atmosphere and in the dark is found.[26] This has to be put in relation to the conductivities of $1 \times 10^{-14} \text{ S cm}^{-1}$ to $1 \times 10^{-6} \text{ S cm}^{-1}$ found for the other compounds which were synthesized and measured in their study (various metal centers were paired with different linkers, $\text{Fe}(\text{ta})_2$ giving the best result) and to a range[27] of $1 \times 10^{-9} \text{ S cm}^{-1}$ to $1 \times 10^{-3} \text{ S cm}^{-1}$ covered by MOFs which one might call conductive.

The basic outline of this thesis is as follows: in the first part, the theoretical foundation for the studies presented in the second part is laid. The first part comprises a short introduction to density-functional theory (DFT) which is used to calculate any of the material properties of interest, the description of periodic structures using Bravais lattices and Bloch's theorem on the more elementary side.

Ensuing this are the introductions to the three main aspects found again in the Bardeen–Shockley mobility formula: the vibrational properties of a harmonic crystal and the theory of elasticity, the electronic structure of a crystal and the effective mass, and finally the coupling of the charge carriers and phonons using Bardeen's and Shockley's deformation potential theory of this interaction. In another chapter on charge transport those aspects are then brought into a common context and the expression for the relaxation time and the mobility in the Bardeen–Shockley theory is derived as well as a generalized expression giving expression for the relaxation time which depends on the reciprocal spatial direction.

In the second part of this thesis, the different studies on various influences on the charge carrier mobility and in particular on the three underlying material properties are presented. The first focus lies on the effects exerted by exchanging the metal centers of a cubic metal(II) triazolate crystal. This changes mainly the polarizability of the metal nodes and should

keep the effect on the phonon-related properties low, so that predominantly the electronic ones are influenced.

Next to the charge carrier mobility of triazolate crystals with different metal centers, the influence of gas absorption is discussed for the example of physisorption into $\text{Fe}(\text{ta})_2$. The limitation to weakly interacting gases was done, so that the influence on the transport properties of the network could be studied independently from those which might be inflicted by a strongly interacting absorbate (cf. guest-mediated transport in ref. [19]).

Finally, building on the collected results, the effect of the meta-structure, i. e. the coordinative metal-linker bonding which gives rise to the net-like structure of a MOF, on the parameters which enter the Bardeen–Shockley mobility—putting a focus on the deformation potential—is discussed.

2 Theoretical Background

This chapter serves as an introduction to the most important pieces of solid state physics with regard to the mobility of charge carriers in an ideal crystalline solid. Therefore, this has to encompass the dynamic properties of both matter constituents: electrons and nuclei, where the latter will be sometimes called ions in the following discussion. Both labels shall be used interchangeably. The presentation is kept rather succinct as most information contained in this chapter can be found in one or another textbook[20–22, 28–47].

2.1 The many-body problem of the solid

The general Hamiltonian operator* H of any system consisting of electrons and nuclei can be written as a sum of three principal parts: the Hamiltonian of the ions, the Hamiltonian of the electrons, and the Hamiltonian of the interaction between ions and electrons,

$$H = H^{\text{ion}} + H^{\text{el}} + H^{\text{el-ion}}. \quad (2.1)$$

These three terms can be broken down into functions of the corresponding canonical degrees of freedom (DoFs). For each ion A there are positions and momenta, denoted as R_A and P_A , as well as for each electron, for which they are labelled by r_i and p_i^\dagger . In the following, the individual terms are introduced, starting with the ionic one:

$$H^{\text{ion}} = \sum_{A=1}^N \frac{1}{2M_A} P_A \cdot P_A + \frac{1}{2} \sum_{\substack{A,B=1 \\ A \neq B}}^N \frac{Z_A Z_B}{|R_A - R_B|}, \quad (2.2)$$

*In the following, the explicit mentioning that the Hamiltonian is an operator will be dropped. Also, every equation will be assumed to be written in atomic units (AU), that is: distances are measured in multiples of the Bohr radius a_0 , masses are measured in electron masses m_e , charges are measured in elementary charges e , energy is measured in multiples of the Hartree energy E_h , and action is measured in multiples of the reduced Planck constant \hbar . All other units are written as combinations of these basic units, if possible. For a further explanation and explicit conversion factors to the units of the international system of units (SI), refer to the book by Szabo and Ostlund.[28]

[†]Here, each canonical DoF is to be understood as a vector operator, e. g. $R_A = (R_A^1, R_A^2, R_A^3)$, with components R_A^i .

where M_A is the mass of ion A and Z_A its charge. A similar expression is written down for the Hamiltonian of the electrons:

$$H^{\text{el}} = \sum_{i=1}^n \frac{1}{2} p_i \cdot p_i + \frac{1}{2} \sum_{\substack{i,j=1 \\ i \neq j}}^n \frac{1}{|r_i - r_j|}. \quad (2.3)$$

Finally, the electron-ion interaction is given by the term

$$H^{\text{el-ion}} = \sum_{i=1}^n \sum_{A=1}^N \frac{Z_A}{|r_i - R_A|}. \quad (2.4)$$

The clamped nuclei and the adiabatic approximation[44, 48, 49] are used to separate the electronic and the ionic DoFs. This leads to the electronic Hamiltonian

$$H^{\text{elec}} = H^{\text{el}} + H^{\text{el-ion}}, \quad (2.5)$$

$$= \sum_i \left\{ \frac{1}{2} p_i \cdot p_i + \frac{1}{2} \sum_{i \neq j} \frac{1}{|r_i - r_j|} + \underbrace{\sum_A \frac{Z_A}{|r_i - R_A|}}_{v(r_i)} \right\}. \quad (2.6)$$

Eigenstates of this Hamiltonian see the ions as a static configuration which only parametrically enters through the electron-ion interaction. For the potential energy of a single electron in the field of all ions, $v(r_i)$, one often reads the term external potential.

One might at this point already guess that the general many-body (MB) problem of quantum mechanics is not exactly solvable and tackling it numerically is also not easily feasible. Even for the electronic problem, one is still restricted to more or less small systems depending on more or less sophisticated methods. One possibility to perform calculations on larger systems is to change from a wavefunction theory (WFT) to a DFT (cf. section 2.2). This means a change from a theory, where the central object—the MB wavefunction $\Psi(x_1, \dots, x_n)$ —depends on $4n$ variables* to a theory, where the central object—the (electron) density $\rho(x)$ is an observable which only depends on three or four variables, depending on the treatment of the electron spin. Clearly this change involves a trade-off in accuracy, as state of the art DFT is not an exact theory†.

A problem arises for systems with particle numbers in the order of the Avogadro constant. Especially for the cases considered in condensed matter physics, i. e. in liquids and solids, this can limit a simulation to more or less sophisticated methods. In case of the solid matter, one finds the large class of crystalline solids which show translational symmetry of the atomic positions to a large extent. This periodicity allows for a huge simplification by which one can afford to carry out calculations on these systems as described in the next section. Note, however, that also here there is a trade-off in the sense that real materials

*Three spatial and one spin DoF for each electron.

†Even though in principle it could be one (cf. section 2.2).

cannot be described in the picture of an ideal crystal. The real crystal will show several sorts of defects, the most severe one being probably its truncation at a surface. Nevertheless, the possibility to grasp the physical properties of large systems has lead and continues to lead to interesting and insightful results.

2.2 Density-functional theory

2.2.1 Reformulating the electronic many-body problem

There exists a different approach to the electronic MB problem which does express quantum mechanical expectation values not in terms of a state vector or wavefunction functional, but in terms of one of the (groundstate) electron density ρ , where

$$\rho(r) = N \int \cdots \int |\Phi(\underline{x})|^2 ds_1 d^4x_2 d^4x_3 \cdots d^4x_N . \quad (2.7)$$

Here, x_i subsumes the spatial DoFs r_i and the electron spin s_i . A spin-resolved density can be obtained, if the integral $\int \cdots ds_1$ is omitted.

Such a reformulation is possible and is exact as shown by Hohenberg and Kohn (HK) in their first theorem.[50] Furthermore, they could show in their second theorem[50] that for any correctly normalized, positive-valued trial density a variational principle holds for the total energy of the system. The proofs of the HK theorems are well-presented and discussed throughout literature[29, 32, 51] and will not be repeated here. Instead, the expression for the total energy E as a functional of the electron density ρ is given:

$$E[\rho] = \int \rho(x) v(x) d^3r + (\langle T \rangle[\rho] + \langle V^{ee} \rangle[\rho]) = \int \rho v d^3r + F[\rho] . \quad (2.8)$$

where, $F = \langle T \rangle + \langle V^{ee} \rangle$ is the universal functional. It is universal in the sense that it is independent of the configuration of nuclei of any given system. The term in (2.8) which is written as an integral comes from the remaining term in the Hamiltonian, the interaction between electrons and nuclei. Its average can be represented as an integral over space of the electron density and a potential v ,

$$\langle V^{eN} \rangle = \langle \Psi | \sum_i \sum_\alpha \frac{Z_\alpha}{|r_i - R_\alpha|} | \Psi \rangle = \int \rho v d^3r . \quad (2.9)$$

The two Hohenberg–Kohn theorems provide the basis of DFT as they enable one to find the groundstate electron density of any system. However, this is only true in theory, as an explicit expression for F in (2.8) is unknown. Kohn and Sham (KS)[52] tackled this problem by two means. At first, they rewrote the universal functional using the classical

electrostatic energy $J[\rho]$ contained therein, where

$$J[\rho] = \frac{1}{2} \iint \rho(r_1) r_{12}^{-1} \rho(r_2) d^3r_1 d^3r_2 . \quad (2.10)$$

Second, they introduced a system of non-interacting electrons which is assumed to have the same groundstate density as the real system. This allows for a rewriting of the kinetic term $T[\rho]$ as the kinetic energy T_s of the non-interacting system and a rest which contains the electron correlation. Overall, one writes

$$F[\rho] = T^s[\rho] + J[\rho] + E^{\text{xc}}[\rho] , \quad (2.11)$$

where E^{xc} is the exchange-correlation (XC) energy which is defined as the sum of the exchange and correlation energy,

$$E^{\text{xc}}[\rho] = E^{\text{x}}[\rho] + E^{\text{c}}[\rho] , \quad (2.12)$$

such that (2.11) is fulfilled. It is furthermore possible to rewrite the exchange energy E^{x} using the adiabatic connection formula[31, 32] (cf. appendix I) as

$$\langle \Psi_0^{\text{KS}} | \widehat{V}^{\text{ee}} | \Psi_0^{\text{KS}} \rangle = J[\rho] + \int \rho \left[\int_0^1 v_\lambda^{\text{x}} d\lambda \right] d^3r , \quad (2.13)$$

$$= J[\rho] + E^{\text{x}}[\rho] , \quad (2.14)$$

where $0 \leq \lambda \leq 1$ is the adiabatic switching parameter which regulates the strength of the electron-electron interaction* By approximating the λ -integral in (2.14), one finds that it is possible to get a part of the exchange energy from the Hartree–Fock (HF)-exchange term,

$$E^{\text{x,HF}} = \frac{1}{2} \sum_{b>a} \iint \psi_a^*(r_1) \psi_b^*(r_2) r_{12}^{-1} \psi_b(r_1) \psi_a(r_2) d^3r_1 d^3r_2 . \quad (2.15)$$

At least up to (2.11), Kohn-Sham density-functional theory (KS-DFT) is still an exact mean field theory. However, the somewhat coy definition of E^{xc} already suggests that its exact form remains unknown to this day. Over the years, numerous approximations of E^{xc} have appeared. A few of these density-functional approximations (DFAs) are introduced in the next section. Considering this discussion, there are two quantities, the XC potential v^{xc} and the XC kernel f^{xc} which should be introduced. They are formally defined by

$$E^{\text{xc}} = \int \rho v^{\text{xc}} d^3r = \int f^{\text{xc}} d^3r . \quad (2.16)$$

*One uses the modified electronic MB Hamiltonian $\widehat{H}_\lambda^{\text{elec}} = \widehat{T}^{\text{el}} + \widehat{V}_\lambda^{\text{eN}} + \lambda \widehat{V}^{\text{ee}}$. The dependency of $\widehat{V}_\lambda^{\text{eN}}$ on λ compensates the changes in the density, so that the switching takes place for a fixed density.

2.2.2 Approximating the exchange-correlation functional

One of the standard approaches to sort the different DFAs is by setting up a loose hierarchy or “heuristic characterization”[31] based on the content of physical information used to define one of them. J. P. Perdew termed the picture of “Jacob’s ladder” for this hierarchy. At its first rung, there is the local density approximation (LDA), the XC energy of which is locally modeled as a homogeneous electron gas (HEG),

$$E^{\text{xc,LDA}}[\rho] = \int \rho(r) \mathcal{E}^{\text{xc,HEG}}(\rho(r)) d^3r . \quad (2.17)$$

The HEG is a well-studied system and the XC energy can be almost solved exactly. Therefore, also LDA is a good approximation for extended systems in which the electrons are more delocalized, thus showing a spatially slowly varying electron density. Such systems are e. g. prototypic metals, such as the alkali metals, and the classical semiconductors like silicon or germanium. There exists a spin-polarized form of the LDA functional which is called local spin density approximation (LSDA).

A straightforward idea to improve the LDA is by using a Taylor expansion with respect to the local density,

$$E^{\text{xc}} = \int \left\{ \rho(r) v^{\text{xc},(0)}(\rho(r)) + \nabla \rho(r) v^{\text{xc},(1)}(\rho(r)) + \dots \right\} d^3r . \quad (2.18)$$

This is the gradient expansion approximation (GEA). Unfortunately, by such an ad-hoc introduction of the gradient terms, much of the two-electron physics included in the LDA is lost*, so that e. g. a order-1 GEA can perform even worse than LDA. However, by enforcing the correct restrictions, it is possible to restore these aspects.[32] This leads to the functionals of the second rung, the generalized gradient approximation (GGA) functionals, for which the XC kernel depends on the local density and the local density gradient,[32]

$$E^{\text{xc,GGA}}[\rho] = \int f^{\text{xc,GGA}}(\rho(r), \nabla \rho(r)) d^3r . \quad (2.19)$$

A popular example for a GGA functional which is free of semi-empirical parameters is the Perdew–Burke–Ernzerhof (PBE) functional.[53] Further improvement can sometimes be achieved by including the Laplacian[†] of the density or any other orbital information.[31] Such functionals are then called meta-GGA.

On the next rung of Jacob’s ladder there are hybrid functionals which contain a portion of exact exchange energy $E^{\text{x,HF}}$, which has the formal expression of the mean HF exchange energy. This is motivated by the adiabatic connection formula (cf. appendix I

*This centers around the notion of the XC hole, i. e. a depletion of the probability density to find two electrons in direct vicinity, which is not discussed here. The reader is referred to the book by Koch and Holthausen[32] or the book by Jensen[31].

[†]That is the divergence of the gradient, $\text{div grad } \rho \sim \nabla \cdot \nabla \rho$.

and section 2.2.1). Consequently, one writes for the XC energy

$$E^{\text{xc}}[\rho] = \alpha E^{\text{x,HF}} + (1 - \alpha) \int \rho v_1^{\text{x}} d^3r + E^{\text{c}}[\rho]. \quad (2.20)$$

The integral term in (2.20) is the exchange energy, which is not exactly known and often approximated by the exchange energy of LSDA.[31] Frequently, this inclusion of a part of $E^{\text{x,HF}}$ improves the results for non-metallic systems. This can be attributed either to a reduction of the so-called SI error (cf. section 2.2.3) or to what is commonly called error cancelation, i. e. the systematic errors introduced by the LSDA XC energy and the HF exact exchange energy compensate each other numerically.

2.2.3 Self-interaction error in Kohn–Sham density-functional theory

The use of the classical electron-electron interaction in KS-DFT without the knowledge of the exact exchange functional, leads to an artificial contribution to the ground state energy. This error is called the self-interaction error as, in a one-electron system, it means that the electron-electron interaction (2.10) does not disappear despite no other electron being present.[54] Thus, it formally describes the interaction, i. e. a repulsion, of this single electron with itself, leading to an over-delocalization of the KS states and thus the charge density.

This error is preeminent in particular for the states of the angular momentum shells higher than the d -shell and thus commonly encountered when dealing with transition metals.[55]

To overcome this error, no exact way is known except for model systems. Commonly, as highlighted in section 2.2.2, a portion of exact HF-exchange energy, is included into the exchange functional. Depending on the amount of HF-exchange energy, this compensates the self-interaction error or leads to an over-localization of the states as new errors are introduced. Therefore, the amount of HF-exchange energy included is fitted, so that the total energies of the KS-DFT model reproduce sophisticated theoretical or experimental results.[31]

There are, of course, a number of other methods aimed at compensating the self-interaction error (SIE). The interested reader is pointed to the review by Cohen et al.[56].

2.3 Lattices and the Bloch theorem

This section is a very compact introduction into the terminology of Bravais lattices and the associated reciprocal lattice, the Bloch theorem, and periodic boundary conditions. More extensive presentations of the matter can be found in almost any book on solid state or condensed matter physics, like e. g. the one by Ashcroft and Mermin[22]. The accounts given by Kittel[20] and Marino[41] were also found to be concise and appealing.

2.3.1 Bravais lattices

A Bravais lattice is a set of points

$$\mathcal{BL} = \{L_{\underline{m}} \mid L_{\underline{m}} = m_1 a_1 + m_2 a_2 + m_3 a_3, \quad \underline{m} = (m_1, m_2, m_3) \in \mathbb{Z}^3\}. \quad (2.21)$$

The vectors a_i are called the primitive basis vectors of the lattice and clearly, the points in the set are repeated periodically. Any translation of a lattice point by an integer linear combination of basis vectors maps this point onto another lattice point, that is the lattice is invariant under the operation

$$L_{\underline{m}} \rightarrow L_{\underline{m}} + T, \quad T = l a_1 + m a_2 + n a_3. \quad (2.22)$$

The volume spanned by the a_i which contains exactly one unique lattice point is called the primitive unit cell of the Bravais lattice. It is defined as

$$\mathcal{UC} = \{r \mid r = x_1 a_1 + x_2 a_2 + x_3 a_3, \quad x_i \in [0, 1)\} \quad (2.23)$$

and has the value

$$V_{\mathcal{UC}} = |(a_1 \times a_2) \cdot a_3|. \quad (2.24)$$

In general, a crystal will not only have a lattice basis $\{a_1, a_2, a_3\}$ but also a basis of atoms $A \in \mathcal{UC}$. The positions R_A are per convention either given in cartesian coordinates relative to the origin of \mathcal{UC} or in terms of *fractional coordinates* in the basis of the primitive lattice basis a_i . Technically, a crystal is described by several Bravais lattices which are shifted according to the atomic positions in one unit cell which is taken as reference. Thus, to account for this, the atomic basis and the Bravais lattice together are said to constitute the crystal lattice (in contrast to a single Bravais lattice).

2.3.2 The reciprocal lattice

In the following, the so-called reciprocal basis vectors b_i which span the reciprocal lattice $\overline{\mathcal{BL}}$ are introduced. The need for those quantities suggests itself when studying the Fourier components of a quantity $f(x)$ which has the translational symmetry of an underlying \mathcal{BL} (\mathcal{BL} -symmetry), that is

$$f(x + L_{\underline{m}}) = f(x). \quad (2.25)$$

One introduces the reciprocal basis vectors* b_i , so that their relation to the lattice basis of \mathcal{BL} is given by

$$a_i \cdot b_j = 2\pi\delta_{ij}. \quad (2.26)$$

They may be expressed in terms of the lattice basis vectors a_i as

$$b_1 = \frac{2\pi}{V_{\mathcal{UC}}} a_2 \times a_3, \quad b_2 \text{ and } b_3 \text{ through cyclic permutation.} \quad (2.27)$$

Clearly, the reciprocal basis constitutes a Bravais lattice

$$\overline{\mathcal{BL}} = \{G_{\underline{n}} | G_{\underline{n}} = n_1 b_1 + n_2 b_2 + n_3 b_3, \quad \underline{n} = (n_1, n_2, n_3) \in \mathbb{Z}^3\}, \quad (2.28)$$

Analogous to \mathcal{UC} , $\overline{\mathcal{BL}}$ has the reciprocal cell $\overline{\mathcal{UC}}$. In general, the space spanned by the b_i is called reciprocal space.

Note, that any point x in the crystal can be specified by a position $r \in \mathcal{UC}$ and a lattice vector $L \in \mathcal{BL}$, $x = r + L$. Then, the Fourier component $f(G)$ of the \mathcal{BL} -symmetric function $f(x)$ can be written not as an integral over the complete domain of x , but only as an integral over \mathcal{UC} ,

$$f(G) = \mathcal{N} \int_{\mathcal{UC}} f(r) e^{-iq \cdot r} d^3r. \quad (2.29)$$

\mathcal{N} is the number of Bravais lattice points. Furthermore, take notice that in the Fourier expansion of a \mathcal{BL} -symmetric function only reciprocal lattice vectors appear.

2.3.3 Bloch's theorem

Bloch's theorem defines the correct quantum numbers for and the overall form of the eigenfunctions of a \mathcal{BL} -symmetric Hamiltonian. The two propositions of the Bloch theorem are:

1. Good quantum numbers for an eigenstate of the Hamiltonian are

$$k_i = \frac{2\pi}{|a_i|} n_i, \quad -\frac{\mathcal{N}_i}{2} \leq n_i < \frac{\mathcal{N}_i}{2}, \quad (2.30)$$

where \mathcal{N}_i is the number of lattice points in the spatial dimension i .

2. The eigenfunction $\psi_k(r)$ factorizes into a \mathcal{BL} -symmetric function $u(r)$ and a plane wave,

$$\psi_k(r) = e^{ik \cdot r} u(r). \quad (2.31)$$

*They are called reciprocal as their physical dimension is a reciprocal length.

According to this, the wavevector k can take on only discrete values. However, as the number of lattice points $\mathcal{N} = \mathcal{N}_1\mathcal{N}_2\mathcal{N}_3$ increases, k can as well be assumed to take on continuous values.[48]

2.4 Introduction to the theory of the harmonic solid

2.4.1 Classical theory of lattice vibrations

Conventionally, what is understood as the Born–Oppenheimer approximation (BOA) is actually the Born–Huang or adiabatic approximation. As Maurer[48] points out, it is an instruction on how to propagate the nuclear and electronic states based on an updated energy functional of the other group. For the ionic problem, this means that the dynamics is subject to the potential

$$\mathcal{U}(\underline{R}) = E^{\text{elec}}(\underline{R}) + \frac{1}{2} \sum_{\substack{A,B \\ A \neq B}} \sum_{\underline{m}, \underline{n}} \frac{Z_A Z_B}{|R_{\underline{m}A} - R_{\underline{n}B}|}, \quad (2.32)$$

where $E^{\text{elec}}(\underline{R})$ is the potential energy surface, i. e. the hypersurface of the electronic energy in configuration space. The position R_A of an ion is now assumed to lie within \mathcal{UC} . The overall position, including the unit cell in which the ion lies, is specified by a lattice vector $L_{\underline{m}}$. Notationally, this is expressed by the additional index \underline{m} , so that

$$R_A \rightarrow R_{\underline{m}A} = R_A + L_{\underline{m}}. \quad (2.33)$$

Considering the masses of nuclei, it is possible to take this as a potential of a Lagrangean function

$$\mathcal{L}(\underline{R}, \dot{\underline{R}}) = \mathcal{T}(\dot{\underline{R}}) - \mathcal{U}(\underline{R}), \quad (2.34)$$

where $\mathcal{T}(\underline{P})$, the kinetic energy of the system, is given by

$$\mathcal{T}(\dot{\underline{R}}) = \sum_{\underline{m}, A} \frac{1}{2} M_A \dot{R}_{\underline{m}A} \cdot \dot{R}_{\underline{m}A}. \quad (2.35)$$

Conveniently, one expands $\mathcal{U}(\underline{R})$ in terms of displacement vectors $U_{\underline{m}A}$,

$$U_{\underline{n}A} = R_{\underline{n}A} - R_{\underline{n}A}^{\circ}, \quad (2.36)$$

where $R_{\underline{m}A}^\circ$ is the equilibrium position of the ion, which then yields*[†]

$$\mathcal{U}(\underline{R}) = \mathcal{U}(\underline{R}^\circ) + \frac{1}{2} \sum_{\underline{m},A} \sum_{\underline{n},B} G_{\underline{m}\underline{n}ABij} U_{\underline{m}A}^i U_{\underline{n}B}^j + O(U^4). \quad (2.37)$$

Here, G is the force constant matrix which is defined by

$$G_{\underline{m}\underline{n}ABij} = \left[\frac{\partial^2 \mathcal{U}}{\partial U_{\underline{m}A}^i \partial U_{\underline{n}B}^j} \right]_{\underline{R}^\circ}. \quad (2.38)$$

The expression for the kinetic energy is unchanged by the transformation to displacement vectors as

$$\dot{U}_{\underline{m}A} = \frac{d}{dt} [R_{\underline{m}A}(t) - R_{\underline{m}A}^\circ] = \dot{R}_{\underline{m}A}. \quad (2.39)$$

In this so-called harmonic approximation—hence one speaks of the harmonic solid—of the potential, the Lagrangean function reads

$$\mathcal{L} = \frac{1}{2} \sum_{\underline{m},A} M_A \dot{U}_{\underline{m}A}^i \dot{U}_{\underline{m}A}^i - \frac{1}{2} \sum_{\underline{m},A} \sum_{\underline{n},B} G_{\underline{m}\underline{n}ABij} U_{\underline{m}A}^i U_{\underline{n}B}^j, \quad (2.40)$$

where the constant shift of $\mathcal{U}(\underline{R}^\circ)$ is used as reference energy. Typically, mass-weighted coordinates are introduced,

$$U_{\underline{m}A} \longrightarrow M_A^{-1/2} U_{\underline{m}A}, \quad (2.41)$$

$$\dot{U}_{\underline{m}A} \longrightarrow M_A^{-1/2} \dot{U}_{\underline{m}A}, \quad (2.42)$$

leading to the expression

$$\mathcal{L} = \frac{1}{2} \sum_{\underline{m},A} \dot{U}_{\underline{m}A}^i \dot{U}_{\underline{m}A}^i - \frac{1}{2} \sum_{\underline{m},A} \sum_{\underline{n},B} \frac{1}{\sqrt{M_A M_B}} G_{\underline{m}\underline{n}ABij} U_{\underline{m}A}^i U_{\underline{n}B}^j, \quad (2.43)$$

*Summation over pairs of vector (or tensor) indices will be always be implied in the following. Other labels or indices will in general not be automatically included in this convention, e. g. the indices of the atomic basis of the unit cell or the lattice vector labels. Indices will be grouped type-wise, i. e. if the object G has two indices i and j , two atomic basis indices A and B , and two lattice indices \underline{m} and \underline{n} , will be labeled $G_{\underline{m}\underline{n}ABij}$. The order of the individual groups will always be: lattice indices, basis indices, tensor indices. Note, that the position (co- or contravariant) of the repeated indices is not really important here, as the underlying space is just the Euclidean one and the metric is just δ_{ij} . That means, indices may switch position arbitrarily.

[†]All odd terms vanish as the configuration $\underline{R}^\circ = \{R_{A\underline{m}}^\circ\}$ is assumed to be in a minimum of the potential surface \mathcal{U} .

where the same notation for the mass-weighted coordinates is used as for the non-mass-weighted ones. From this form of \mathcal{L} , one obtains the Euler–Lagrange equations

$$\ddot{U}_{\underline{m}A}^i = - \sum_{\underline{n},B} \frac{1}{\sqrt{M_A M_B}} G_{\underline{m}\underline{n}ABij} U_{\underline{n}B}^j. \quad (2.44)$$

As Ziman remarks[21], the force terms on the right-hand side of (2.44) cannot depend on the absolute values for \underline{m} and \underline{n} , but only on their difference $\underline{m} - \underline{n}$. This means,

$$G_{\underline{m}\underline{n}ABij} = G_{\underline{m}-\underline{n},0ABij} =: G_{ABij}(\underline{m} - \underline{n}). \quad (2.45)$$

With this notation, the equations of motion (EoMs) become

$$\ddot{U}_{\underline{m}A}^i = - \sum_{\underline{n},B} \frac{1}{\sqrt{M_A M_B}} G_{AB}{}^i{}_j(\underline{n}) U_{\underline{m}+\underline{n},B}^j. \quad (2.46)$$

Any solution $U_{\underline{m}A}^i$ to this system of equations must obey the Bloch theorem, that is

$$U_{\underline{m}A}^i(t) = U_{\underline{0}A}^i(t) e^{iq \cdot L_{\underline{m}}} = U_A^i(t, q) e^{iq \cdot L_{\underline{m}}}, \quad (2.47)$$

where q is a wave vector and the notation $U_A^i(q)$ means that this is a solution for a particular q . Inserting this into (2.46), one finds

$$\ddot{U}_A^i(q) = - \sum_B \left\{ \sum_{\underline{n}} \frac{1}{\sqrt{M_A M_B}} G_{AB}{}^i{}_j(\underline{n}) e^{iq \cdot L_{\underline{n}}} \right\} U_B^j(q). \quad (2.48)$$

The term in braces is the dynamical matrix, that is the Fourier transform of the (mass-weighted) force constant matrix. In the following, its elements are denoted by $D_{ABij}(q)$, giving

$$\ddot{U}_A^i(q) = - \sum_B D_{AB}{}^i{}_j(q) U_B^j(q). \quad (2.49)$$

Note, that by imposing the validity of the Bloch theorem through (2.47), the displacement vector $U_A^i(t, q)$ is the same in each cell, that means that in each cell of the crystal, the atom A moves in the same direction with the same amplitude, but with varying phase.[21, 33] Assuming, that the time dependence of $U_A^i(t, q)$ is the classical one, that is

$$U_A^i(t, q) = \epsilon_A^i(q) e^{-i\omega t}, \quad (2.50)$$

where $\epsilon_A^i(q)$ subsumes amplitude and polarization vector of the vibrational displacement pattern or mode, the EoMs (2.49) then become

$$\epsilon_A^i(q) \frac{d^2}{dt^2} e^{-i\omega t} = - \sum_B D_{AB}{}^i{}_j(q) \epsilon_B^j(q) e^{i\omega t}, \quad (2.51)$$

$$-\omega^2 \epsilon_A^i(q) = - \sum_B D_{AB}{}^i{}_j(q) \epsilon_B^j(q). \quad (2.52)$$

Now, this is just the eigenproblem of the dynamic matrix,

$$\sum_B \{D_{AB}{}^i{}_j(q) - \omega^2 \delta_{AB} \delta_j^i\} \epsilon_B^j(q) = 0, \quad (2.53)$$

yielding the eigenpairs $(\omega_s(q), \epsilon_{As}^i(q))$, where s labels the individual $3N$ modes. This means that by expressing the displacement vectors $U_{A\bar{m}}(t)$ through $\epsilon_{As}(q)$ (using expansion coefficients $a_s(q)$),

$$U_{A\bar{m}}^i(t) = \frac{1}{\sqrt{N}} \sum_{qs} a_s(q) \epsilon_{As}^i(q) e^{i[q \cdot L_{\bar{m}} - \omega_s(q)t]}, \quad (2.54)$$

together with the corresponding generalized velocities one can bring the Lagrangean into a form, where it yields a set of decoupled EoMs. Introducing the normal mode Q_s ,

$$Q_s(t, q) = a_s(q) e^{-i\omega_s(q)t}, \quad (2.55)$$

so that

$$U_{A\bar{m}}^i(t) = \frac{1}{\sqrt{N}} \sum_{qs} Q_s(t, q) e^{iq \cdot L_{\bar{m}}}, \quad (2.56)$$

one finds for the Lagrangean

$$\mathcal{L} = \frac{1}{2} \sum_{qs} \left\{ \dot{Q}_s(t, -q) \dot{Q}_s(t, q) - \omega_s^2(q) Q_s(t, -q) Q_s(t, q) \right\}. \quad (2.57)$$

In this form, still, the two momenta q and $-q$ couple. However, as the $U_{A\bar{m}}$ must be real per definition, one finds the following identities for the new—complex—DoFs:

$$Q_s(t, -q) = Q_s^*(t, q) \quad (2.58)$$

and

$$\epsilon_{As}^i(-q) = [\epsilon_{As}^i]^*(q). \quad (2.59)$$

Therefore, the Lagrangean becomes

$$\mathcal{L} = \frac{1}{2} \sum_{qs} \left\{ \dot{Q}_s^*(t, q) \dot{Q}_s(t, q) - \omega_s^2(q) Q_s^*(t, q) Q_s(t, q) \right\}. \quad (2.60)$$

2.4.2 Classical theory of elasticity

To derive the classical theory of elasticity from the model of the harmonic solid as discussed in section 2.4.1, one starts with the potential energy for a distorted configuration in the harmonic approximation,

$$\mathcal{U} = \frac{1}{2} \sum_{\underline{m}, A} \sum_{\underline{n}, B} G_{\underline{m}\underline{n}ABij} U_{\underline{m}A}^i U_{\underline{n}B}^j. \quad (2.61)$$

In the following, the form of the displacements is now restricted to homogeneous deformations, i. e. those deformation which do not break the \mathcal{BL} -symmetry.[44] The reason for this can be easily understood, if one realizes that the goal of this derivation are the equations which describe the deformation of a volume element in a macroscopic solid. The deformations have to be such that the microscopic deformation can lead to the macroscopic deformation. This is the case if every point in the volume element undergoes the same deformation, i. e. a shift and some kind of stretching of the position vector.

Thus, homogeneous deformations can be decomposed into two terms,

$$U_{\underline{m}A}^i = U_A^i + u^i_k R_{\underline{m}A}^{ok} \quad (2.62)$$

The first term shifts the whole sublattice of A ions and the second term changes the relative positions of the ions within one sublattice. Inserting (2.62), into the potential energy expression and dividing by the unit cell volume, one finds the expression for the potential energy density due to the homogeneous deformation to be

$$\mathcal{U} = \frac{1}{2V_{uc}} \sum_{\underline{m}, A} \sum_{\underline{n}, B} G_{\underline{m}\underline{n}ABij} U_A^i U_B^j \quad (2.63a)$$

$$+ \frac{1}{2V_{uc}} \sum_{\underline{m}, A} \sum_{\underline{n}, B} G_{\underline{m}\underline{n}ABij} \left\{ U_A^i u^i_k R_{\underline{m}A}^{ok} + U_B^j u^j_l R_{\underline{n}B}^{ol} \right\} \quad (2.63b)$$

$$+ \frac{1}{2V_{uc}} \sum_{\underline{m}, A} \sum_{\underline{n}, B} G_{\underline{m}\underline{n}ABij} R_{\underline{m}A}^{ok} R_{\underline{n}B}^{ol} u^i_k u^j_l. \quad (2.63c)$$

The term in (2.63a) is the contribution to the potential energy due to shifts of the ion sublattices against each other.[44] These shifts do not change the macroscopic shape of the crystal and are thus called internal strains.[44] The tensor u is then for the corresponding reason called the external strain tensor. The second term describes how the internal strains couple to the external ones.

As Born and Huang remark[44], the internal strains are fixed by the conditions

$$\frac{\partial \mathcal{U}}{\partial U_A^i} = \sum_{\underline{m}, \underline{n}, B} G_{\underline{m}\underline{n}ABij} \left\{ U_B^i + R_{\underline{n}B}^{ol} u_l^i \right\} = 0. \quad (2.64)$$

The tensor elements appearing in the purely external term (2.63c),

$$c_{ijkl} = \frac{1}{V_{\mathcal{UC}}} \sum_{\underline{m}A} \sum_{\underline{n}B} G_{\underline{m}\underline{n}ABij} R_{\underline{m}A}^{ok} R_{\underline{n}B}^{ol}, \quad (2.65)$$

are the elastic constants of the crystal. The tensor c is totally symmetric and together with the (external) strain tensor lies at the heart of the theory of elasticity. The term (2.63c) is thus called the elastic energy density,

$$\mathcal{U}^{\text{elast}} = \frac{1}{2} c_{ijkl} u^{ij} u^{kl}. \quad (2.66)$$

The contraction $c_{ijkl} u^{kl}$ can be interpreted as a linear response relation,

$$s_{ij} = c_{ijkl} u^{kl}. \quad (2.67)$$

This is Hooke's law which links the strains u^{ij} on the crystal to the stresses s^{ij} , the divergence of which is the force density acting on the crystal.

Similarly, the internal strains will lead to internal stresses which give rise to another force density. Within elasticity theory, one assumes[43] that these forces are in equilibrium, so that the elastic energy is the only term to be considered. This assumption is justified given that the internal strains are small and the crystal structure should adapt fast, compared to the time scale of macroscopic deformations.

2.4.3 Hydrostatic deformation

A subclass of the homogeneous deformation is the hydrostatic deformation which is named for the fact that this is the only deformation one typically can consider for a simple continuum model of a liquid. The strain tensor can always be formally divided into a pure shear and the hydrostatic part,

$$u_{ij} = \underbrace{\left(u_{ij} - \frac{1}{3} \delta_{ij} u_l^l \right)}_{\text{pure shear}} + \underbrace{\frac{1}{3} \delta_{ij} u_l^l}_{\text{hydrostatic}}. \quad (2.68)$$

Considering a pure hydrostatic deformation, i. e. a strain tensor without a shear strain. Then, the elastic energy density becomes

$$\mathcal{U}^{\text{elast}} = \frac{1}{2} c^{ijkl} u_{ij} u_{kl}, \quad (2.69)$$

$$= \frac{1}{2} \left(\frac{1}{9} c^{ijkl} \delta_{ij} \delta_{kl} \right) (u_l^l)^2, \quad (2.70)$$

$$= \frac{1}{2} c_{i k}^{i k} (u_l^l)^2, \quad (2.71)$$

$$= \frac{1}{2} C_o g^2. \quad (2.72)$$

The elastic energy thus depends quadratically on a parameter g , which can be termed the magnitude of the deformation. The remaining elastic constant is the bulk modulus

$$C_o = \frac{1}{9} c_{i k}^{i k}. \quad (2.73)$$

2.4.4 Quantization of the collective excitations

Having discussed the microscopic, classical theory of lattice vibrations and how the physics behind this leads the long range behaviour as seen in the theory of elasticity, what is left to discuss is the quantum physics of the ion vibrations. This serves to introduce the creation and annihilation operator formalism which will simplify the understanding of the electron-phonon interaction in section 2.6.2.

Within the formalism of canonical quantization, one takes the classical Hamiltonian which is obtained through the usual Legendre transformation from the Lagrangian function,

$$\mathcal{H} = \frac{1}{2} \sum_{s q} \{ P_s^*(t, q) P_s(t, q) + Q_s^*(t, q) Q_s(t, q) \}, \quad (2.74)$$

where $P_s = \dot{Q}_s$ in mass-weighted coordinates, and imposes the canonical commutation relations of the Schrödinger picture*

$$[Q_s(q), Q_{s'}(q')] = [P_s(q), P_{s'}(q')] = 0, \quad (2.75)$$

$$[Q_s(q), P_{s'}(q')] = i \delta_{ss'} \delta(q - q'). \quad (2.76)$$

Thereby, the canonical degrees of freedom are represented by their respective operators. Now, writing these operators in terms of phonon creation operators, $a_s^\dagger(q)$, and annihilation operators, $a_s(q)$, one finds similar to the simple harmonic oscillator[30, 37]

$$Q_s(q) = \frac{1}{\sqrt{2\omega_s(q)}} \left(a_s^\dagger(-q) + a_s(q) \right) \quad (2.77)$$

*Briefly: operators do not have time dependence, only the wavefunction has.

and

$$P_s(q) = i \sqrt{\frac{\omega_s(q)}{2}} \left(a_s^\dagger(q) - a_s(-q) \right). \quad (2.78)$$

together with

$$H = \sum_{sq} \omega_s(q) \left[a_s^\dagger(q) a_s(q) + \frac{1}{2} \right] = \sum_{sq} H_{sq}. \quad (2.79)$$

$a_s^\dagger(q)$ creates a phonon in state sq and $a_s(q)$ destroys one. The corresponding states are symmetric under particle exchange as phonons are bosonic pseudoparticles. One denotes them using the occupation number formalism as $|\dots, N_s(q_i), \dots\rangle = |\{N_s(q)\}\rangle$, where $N_s(q)$ is the number of sq -phonons in the state. The following rules[30, 37] apply:

$$a_s^\dagger(q) |\dots, N_s(q), \dots\rangle = \sqrt{N_s(q) + 1} |\dots, N_s(q) + 1, \dots\rangle, \quad (2.80)$$

$$a_s(q) |\dots, N_s(q), \dots\rangle = \sqrt{N_s(q)} |\dots, N_s(q) - 1, \dots\rangle, \quad (2.81)$$

and specifically

$$a_s(q) |\dots, 0, \dots\rangle = 0. \quad (2.82)$$

2.5 Semiclassical electron motion and the effective mass

2.5.1 Quasiclassical equations of motion

In appendix II it is shown, that, using Wannier functions, one can write down an equation which formally resembles a Schrödinger equation (SE) for the dynamics of the Wannier envelopes f_n : [21]

$$\left[\epsilon_n(-i\nabla) - i \frac{\partial}{\partial t} \right] f_n(t, r) + \sum_{n', \underline{m}'} U_{nn'}(L_{\underline{m}}, L'_{\underline{m}}) f'_n(t, L_{\underline{m}}) = 0. \quad (2.83)$$

In this expression, f_n takes the place of the wavefunction and the one-electron Hamiltonian is replaced by the so-called equivalent Hamiltonian $\epsilon_n(-i\nabla)$, that is the expression of the one-electron energies in terms of the electron wavevector k , where k is substituted by an effective momentum operator $-i\nabla$. [21] Assuming that the potential term is a rather weak perturbation, such that only the diagonal elements of the potential term, $U_{nn'}(L_{\underline{m}}, L_{\underline{m}}) = U_n(r = L_{\underline{m}})$, enter the Hamiltonian, the effective SE becomes

$$\left[\epsilon_n(-i\nabla) + U_n(r) - i \frac{\partial}{\partial t} \right] f_n(t, r) = 0. \quad (2.84)$$

One makes use of the correspondence principle and describes a moving electron in a crystal as a wavepacket which moves with a group velocity $v(k)$ which is localized at some point k in reciprocal space.[21, 35] Descending to classical mechanics, one substitutes the momentum operator by a classical momentum function k :

$$-i\nabla \rightarrow k. \quad (2.85)$$

Then, the Hamiltonian function is formally given by

$$\mathcal{H} = \epsilon_n(k) + U(r). \quad (2.86)$$

The Hamiltonian EoMs are then given through

$$\dot{r} = \frac{\partial \mathcal{H}}{\partial k}, \quad (2.87a)$$

$$\dot{k} = -\frac{\partial \mathcal{H}}{\partial r}. \quad (2.87b)$$

From (2.87a) follows an equation for the group velocity of the wavepacket:

$$v(k) = \nabla_k \epsilon_n(k). \quad (2.88)$$

The second equation (2.87b) is just Newton's equation for the potential U_n ,

$$\dot{k} = -\nabla U_n(r). \quad (2.89)$$

Now, let the crystal be subject to an external electric field E . Then, (2.89) becomes

$$\dot{k} = -E. \quad (2.90)$$

From a classical point of view, the acceleration of the electron wavepacket, $\dot{v}(k)$, is of interest. It is given, using another differential expansion, i. e. $\dot{v}(k) = [\nabla_k \otimes v(k)] \cdot \dot{k}$, as well as (2.88):

$$\dot{v}(k) = [\nabla_k \otimes \nabla_k \epsilon(k)] \cdot \dot{k}. \quad (2.91)$$

The object $\nabla_k \otimes \nabla_k \epsilon(k)$ is the Hessian matrix of $\epsilon(k)$ and has elements $\partial^2 \epsilon(k) / \partial k_i \partial k_j$. One inverts (2.91) and inserts the inverted equation into (2.90) to find

$$[\nabla_k \otimes \nabla_k \epsilon(k)]^{-1} \cdot \dot{v}(k) = -E. \quad (2.92)$$

2.5.2 Effective mass tensor

By analogy to the equation of motion for the classical electron in an electric field which reads $m_e \dot{v} = -E$ —using the same symbols and explicitly writing the electron mass—one

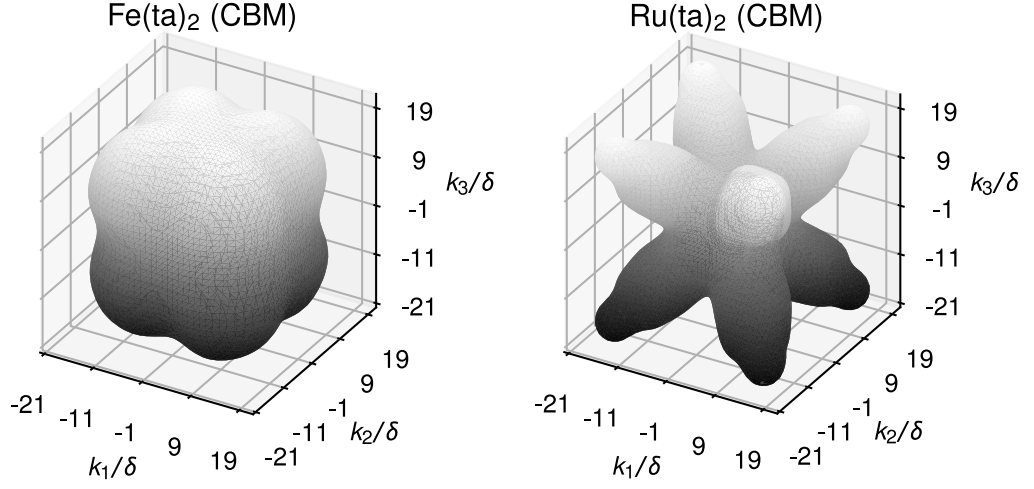


Figure 2.1: Illustration of warped bands. Shown is the interpolated ($\delta = 8 \times 10^{-4} a_0$) energy isosurface 0.85 meV above the conduction band minimum of iron 1,2,3-triazolate and ruthenium 1,2,3-triazolate. Reproduced with permission from ref. [1], © 2019 AIP Publishing.

terms the inverse of the Hessian matrix of $\epsilon(k)$ the effective mass tensor $m^*(k)$,

$$m^*(k) := [\nabla_k \otimes \nabla_k \epsilon(k)]^{-1}. \quad (2.93)$$

Note that this effective mass depends on the point in k space. Around a band extremum at k_o , one can write the second-order* expansion, using $\Delta k = k - k_o$, $\epsilon(k)$ (regard $\nabla_k \epsilon(k_o) = 0$, so all odd-power terms vanish) as

$$\epsilon(k) = \epsilon(k_o) + \frac{1}{2} \Delta k^\top [m^*(k_o)]^{-1} \Delta k + \mathcal{O}(\Delta k^4). \quad (2.94)$$

That means the effective mass which was previously derived from a case where an external electric field was assumed to be present, appears within the expansion of the eigenstates, even without the presence of an external field.

2.5.3 Angular effective mass

Note, that (2.94) cannot be applied to so-called warped bands (Figure 2.1), where ϵ is not necessarily differentiable twice for each direction in k space.[46, 57] Mecholsky *et al.* [57] try to circumvent this problem by using spherical coordinates $(\kappa, \vartheta, \varphi)$ in k space, taking a band extremum as the origin. κ is the distance to the coordinate origin, ϑ the azimuthal

*That is second order in the crystal momentum $\hbar k$. Thus, in unit systems not measuring action in multiples of the Planck constant \hbar , a factor of \hbar^2 has to be added in the quadratic term of (2.94). Note that this applies for the same reason to the ansatz of Mecholsky *et al.* in (2.95).

angle, and φ the polar angle. Then, they expand the state energy in powers of κ ,

$$\epsilon(\kappa, \vartheta, \varphi) = \epsilon(k_o) - \kappa f_1(\vartheta, \varphi) + \frac{1}{2} \kappa^2 f_2(\vartheta, \varphi) + \mathcal{O}(\kappa^3). \quad (2.95)$$

At high-symmetry points of the Brillouin zone (BZ), the linear term vanishes[57] and the function $f_2(\vartheta, \varphi)$ can be interpreted as the inverse effective mass in the direction (ϑ, φ) ,

$$m^*(\vartheta, \varphi) = \frac{1}{f_2(\vartheta, \varphi)}. \quad (2.96)$$

This gives the expression for the band energy

$$\Delta\epsilon(\kappa, \vartheta, \varphi) = \epsilon(\kappa, \vartheta, \varphi) - \epsilon(k_o), \quad (2.97)$$

$$= \frac{1}{2} f_2(\vartheta, \varphi) \kappa^2, \quad (2.98)$$

$$= \frac{1}{2} \frac{\kappa^2}{m^*(\vartheta, \varphi)}, \quad (2.99)$$

provided, that $f_2(\vartheta, \varphi)$ does not become zero for any direction.

2.6 Electron-phonon coupling

In section 2.5, the movement of an electron wavepacket through a crystal was described using a set of semiclassical EoMs. This is an overly simplified picture as a displaced charge in a crystal implicates a polarization of the surrounding lattice, thus generating displacement patterns which move with the charge, i. e. the naked charge carrier is shielded by a phonon cloud.[34] This composite particle is called a polaron. In the following it is assumed that the average number of phonons surrounding the charge carrier is much smaller than unity, so that the approximation as a naked carrier makes sense. Nevertheless, the electron interacts with the phonons states and the interaction potential energy is

$$V(\underline{R}^\circ) = \langle \Psi | H^{\text{el-ion}} | \Psi \rangle. \quad (2.100)$$

2.6.1 Deformation potential coupling

Taylor expanding the potential energy (2.100) up to first order in terms of the ion displacements leads to

$$V(\underline{R}) = V(\underline{R}^\circ) - \sum_{\underline{m}A} \left[\frac{\partial V}{\partial U_{\underline{m}A}^i} \right]_{\underline{R}^\circ} U_{\underline{m}A}^i + O(U^2). \quad (2.101)$$

The change in the potential energy under deformation of the crystal conformation is thus

$$\mathcal{V} = - \sum_{\underline{m}A} \left[\frac{\partial V}{\partial U_{\underline{m}A}^i} \right]_{\underline{R}^0} U_{\underline{m}A}^i. \quad (2.102)$$

Similar to the classical theory of elasticity, one now assumes that the displacements are given by a homogeneous deformation (2.62) of the crystal, i. e. for convenience

$$U_{\underline{m}A}^i = U_A^i + u^i_k R_{\underline{m}A}^{\circ k} = U_A^i + u^i_k R_A^{\circ k} + u^i_k L_{\underline{m}}^k. \quad (2.103)$$

Plugging this into (2.102) yields

$$\mathcal{V} = - \sum_{\underline{m}A} \left[\frac{\partial V}{\partial U_{\underline{m}A}^i} \right]_{\underline{R}^0} U_A^i - \underbrace{\sum_{\underline{m}A} \left[\frac{\partial V}{\partial U_{\underline{m}A}^i} \right]_{\underline{R}^0} R_{\underline{m}A}^{\circ k} u^{ij}}_{D_{ij}}. \quad (2.104)$$

The first term is again the change in the potential energy due to internal strain, \mathcal{V}^I . The second term the potential energy change due to external strain on the crystal, \mathcal{V}^E . The tensor D is the deformation potential tensor. Conceptually the deformation potential was introduced as a scalar by Bardeen and Shockley[24] and extended to a tensor by Herring and Vogt[58].

Note that this potential energy change is the change in the first order perturbation correction term due to external strain. That is, if the internal term is small up to first order to an external strain, the electronic eigenvalues are given as

$$\epsilon(u, k') = \epsilon(0, k) - D_{ij}(k) u^{ij}. \quad (2.105)$$

It is obvious that due to the dependence of the eigenenergies on the electron wavevector k , where k' is the wavevector under strain, D has to depend on k as well. In the following, it is shown that this is not nitpicking but an important subtlety.[59]

To see this, one writes down the expression for the state energy with respect to a strain-dependent reference energy, $\delta\epsilon(u, k') = \epsilon(k', u) - \epsilon_{\text{ref}}(u)^*$ and considers the differential of the state energy $\delta\epsilon(u, k')$,

$$d\epsilon(u, k') = \left[\frac{\partial \epsilon}{\partial u_{ij}} \right]_{u=0} du_{ij} + \left[\frac{\partial \epsilon}{\partial k'_i} \right]_{u=0} dk'_i. \quad (2.106)$$

*In the following derivation, the δ in front of $\delta\epsilon$ is omitted to improve readability.

The wavevector under strain is roughly $k'_i = (\delta_{ij} - u_{ij})k_j$, so that for the differentials dk'_i one finds

$$dk'_i = -k_j du_{ij} + (\delta_{ij} - u_{ij}) dk_j. \quad (2.107)$$

Plugging this into (2.106) yields

$$d\epsilon(u, k') = \left[\frac{\partial \epsilon}{\partial u_{ij}} \right]_{u=0} du_{ij} + \left[\frac{\partial \epsilon}{\partial k'_i} \right]_{u=0} k_j du_{ij} + \left[\frac{\partial \epsilon}{\partial k'_i} \right]_{u=0} (\delta_{ij} - u_{ij}) dk_j. \quad (2.108)$$

Using an expansion up to first order in u one writes[34]

$$\epsilon(u, k') = \epsilon(0, k) - \left[\frac{d\epsilon(u, k')}{du_{ij}} \right]_{u=0} u_{ij}, \quad (2.109)$$

$$= \epsilon(0, k) - \left\{ \left[\frac{\partial \epsilon}{\partial u_{ij}} \right]_{u=0} + \left[\frac{\partial \epsilon}{\partial k'_i} \right]_{u=0} k_j \right\} u_{ij}. \quad (2.110)$$

The third term from (2.108) becomes zero upon differentiation with respect to a strain tensor component, as dk_j/du_{ij} ; k is independent of u . The sum inside the braces in (2.110) is called the deformation potential,

$$D_{ij}(k) = \left[\frac{\partial \epsilon}{\partial u_{ij}} \right]_{u=0} + \left[\frac{\partial \epsilon}{\partial k'_i} \right]_{u=0} k_j. \quad (2.111)$$

Note, that the second term in D_{ij} vanishes if k is a band extremum k_\circ . Only then, is

$$\left[\frac{\partial \epsilon}{\partial k'_i} \right]_{u=0, k=k_\circ} = \left[\frac{\partial \epsilon}{\partial k_i} \right]_{u=0, k=k_\circ} = 0 \quad \Longrightarrow \quad D_{ij}(k_\circ) = \left[\frac{d\epsilon}{du_{ij}} \right]_{u=0} = \left[\frac{\partial \epsilon}{\partial u_{ij}} \right]_{u=0}. \quad (2.112)$$

The values of $D_{ij}(k_\circ)$ measure how much the band energy $\delta\epsilon$ shifts at the band extremum k_\circ under a certain strain of the unit cell. In the isotropic case of $u_{ij} = \delta_{ij}/3 u^l_l$, i. e. under hydrostatic deformation (cf. section 2.4.3), one gets

$$\delta\epsilon(u, k'_\circ) = \delta\epsilon(0, k_\circ) - \frac{1}{3} D_{ij}(k_\circ) \delta_{ij} u^l_l, \quad (2.113)$$

$$= \delta\epsilon(0, k_\circ) - \frac{1}{3} D^i_i(k_\circ) u^l_l, \quad (2.114)$$

which was first recognized by Bardeen and Shockley.[24]

The shift scales with the volume dilation u^l . For later convenience, one defines

$$D^{\text{BS}}(k_o) := \frac{1}{3} D^i_i(k_o), \quad (2.115)$$

the Bardeen–Shockley deformation potential. The shift of the band energies upon dilation of the unit cell volume can be compared to the effect on the eigenenergies for a particle in a box* when the box size varies.[1]

2.6.2 Coupling matrix elements and transition rates

In an ideal crystal, devoid of impurities and defects, the only interaction of the charge carriers leading to a finite electric resistance is with the phonons. The latter are quantized collective excitations of the crystal normal modes. Within this section, the electronic eigenstates $\epsilon(k)$ shall be denoted as $\mathcal{E}(k)$, to clearly distinguish them from the phonon polarization vectors $\epsilon_s(q)$.

The deformation potential interaction is given by the term $D_{ij}u^{ij}$, where u is the strain tensor *operator* in this case. It is given by the symmetrized derivative of the displacement vector operator $U(x)$,

$$U^i(x) = \sum_{sq} \frac{1}{\sqrt{2\mathcal{N}\omega_s(q)}} \left\{ a_s(q) + a_s^\dagger(-q) \right\} e^{iq \cdot x} \epsilon_s^i(q). \quad (2.116)$$

Note, that this operator is obtained from the classical displacements by changing the normal mode to the operator (2.77). Then, the strain tensor operator can be written down as

$$u^{ij} = \sum_{sq} \frac{i}{2\sqrt{2\mathcal{N}\omega_s(q)}} \left[\epsilon_s^i(q)q^j + \epsilon_s^j(-q)q^i \right] \left\{ a_s(q)e^{iq \cdot x} + a_s^\dagger(q)e^{-iq \cdot x} \right\}. \quad (2.117)$$

Note, that the sign of the crystal momentum in the phonon creation operator was switched compared to (2.116) by relabeling the summation index. The deformation potential interaction then reads

$$D_{ij}u^{ij} = \sum_{sq} \frac{ig_s(q)}{\sqrt{2\mathcal{N}\omega_s(q)}} \left\{ a_s(q)e^{iq \cdot x} + a_s^\dagger(q)e^{-iq \cdot x} \right\}, \quad (2.118)$$

where the coupling constants are given by

$$g_s(q) = \frac{1}{2} D_{ij} \left[\epsilon_s^i(q)q^j + \epsilon_s^j(-q)q^i \right]. \quad (2.119)$$

*They are repeated here for convenience: $E_n = \frac{1}{2m} \left(\frac{n\pi}{L} \right)^2$. This means, the spacing between two neighboring states decreases with rising L and vice versa.

Using the identity from (2.59) this becomes

$$g_s(q) = \frac{1}{2} D_{ij} \{ \epsilon_s^i(q) q^j + [\epsilon_s^j(q)]^* q^i \}. \quad (2.120)$$

When calculating the transition rate $W_{k'k}$ from a state $|k; \{N_s(q)\}\rangle$ into $|k'; \{N'_s(q')\}\rangle$, given by Fermi's golden rule,

$$W_{k'k} = 2\pi |\langle k'; \{N'_s(q)\} | D_{ij} u^{ij} | k; \{N_s(q)\} \rangle|^2 \delta(\mathcal{E}(k') - \mathcal{E}(k) + \omega(k' - k)), \quad (2.121)$$

one needs the corresponding matrix elements, $M(k' \{N'_s(q)\}, k \{N_s(q)\})$. With $\Delta k = k' - k$, their evaluation yields

$$\begin{aligned} M(k' \{N'_s(q)\}, k \{N_s(q)\}) &= \langle k'; \{N'_s(q')\} | D_{ij} u^{ij} | k; \{N_s(q)\} \rangle, \\ &= \sum_s \frac{i g_s(\Delta k)}{\sqrt{2\mathcal{N}\omega_s(\Delta k)}} \left\{ \sqrt{N_s(\Delta k)} \delta(N_s(\Delta k) - N'_s(\Delta k) - 1) \right. \\ &\quad \left. + \sqrt{N_s(\Delta k) + 1} \delta(N_s(\Delta k) - N'_s(\Delta k) + 1) \right\} e^{i\Delta k \cdot x}. \end{aligned} \quad (2.122)$$

Realize that, under the assumption of this type of interaction, the number of phonons can change only by one. That is, either through absorption or by emission.

Consider, now, the coupling constants $g_s(q)$ for a cubic crystal, that is $D_{ij} = D\delta_{ij}$,

$$g_s(q) = D \Re \epsilon_s^i(q) q_i, \quad (2.123)$$

where $\Re \epsilon_s(q)$ is the real part of the phonon polarization vector. For the longitudinal acoustic (LA) branch, the polarization vector is just the unit wavevector \hat{q} and for the transversal acoustic (TA) branches the polarization vectors are either perpendicular to it or almost perpendicular.[22] This means, that the coupling between charge carriers and acoustic phonons has to be written as

$$g_s(q) = \begin{cases} D|q| & s = \text{LA}, \\ 0 & s = \text{TA}_1, \text{TA}_2. \end{cases} \quad (2.124)$$

With this, the matrix element becomes

$$\begin{aligned} M(k' \{N'_s(\Delta k)\}, k \{N_s(\Delta k)\}) &= \\ &= \frac{iD|\Delta k|}{\sqrt{2\mathcal{N}\omega_{\text{LA}}(\Delta k)}} \left\{ \sqrt{N_{\text{LA}}(\Delta k)} \delta(N_{\text{LA}}(\Delta k) - N'_{\text{LA}}(\Delta k) - 1) \right. \\ &\quad \left. + \sqrt{N_{\text{LA}}(\Delta k) + 1} \delta(N_{\text{LA}}(\Delta k) - N'_{\text{LA}}(\Delta k) + 1) \right\} e^{i\Delta k \cdot x}. \end{aligned} \quad (2.125)$$

One can write this as the sum of a matrix element associated with the absorption of a longitudinal acoustic phonon and a matrix element associated with the emission of one, according to the delta functions. That is,

$$M_{k'k}^a = \frac{iD|\Delta k|}{\sqrt{2\mathcal{N}\omega_{\text{LA}}(\Delta k)}} \sqrt{N_{\text{LA}}(\Delta k)} \quad (2.126)$$

and

$$M_{k'k}^e = \frac{iD|\Delta k|}{\sqrt{2\mathcal{N}\omega_{\text{LA}}(\Delta k)}} \sqrt{N_{\text{LA}}(\Delta k) + 1}. \quad (2.127)$$

For the total transition rate $W_{k'k}$ this means it can be written as the sum of an absorption and an emission transition rate,

$$W_{k'k} = 2\pi (|M_{k'k}^a|^2 + |M_{k'k}^e|^2) \delta(\mathcal{E}(k') - \mathcal{E}(k) + \omega_{\text{LA}}(\Delta k)), \quad (2.128)$$

$$= \frac{\pi D^2 |\Delta k|^2}{\mathcal{N}\omega_{\text{LA}}(\Delta k)} (2N_{\text{LA}}(\Delta k) + 1) \delta(\mathcal{E}(k') - \mathcal{E}(k) + \omega_{\text{LA}}(\Delta k)). \quad (2.129)$$

Further assumptions are made: first, the phonons are assumed to provide a heat bath, so that one can write the Bose–Einstein occupation number for $N_{\text{LA}}(\Delta k)$ and second, one assumes that the temperature is high enough that one can make the high temperature approximation[46] for this occupation number:

$$N_{\text{LA}}(\Delta k) = \frac{1}{e^{\beta\omega_{\text{LA}}(\Delta k)} - 1}, \quad (2.130)$$

$$\approx \frac{1}{1 + \beta\omega_{\text{LA}} + \frac{1}{2}\beta^2\omega_{\text{LA}}^2 - 1}, \quad (2.131)$$

$$\approx \frac{1}{\beta\omega_{\text{LA}}} \left(1 - \frac{1}{2}\beta\omega\right), \quad (2.132)$$

$$= \frac{1}{\beta\omega_{\text{LA}}(\Delta k)} - \frac{1}{2}. \quad (2.133)$$

With this, and assuming that the scattering is elastic and thus the phonon energy in the argument of the δ -distribution vanishes, the transition rate $W_{k'k}$ in (2.129) becomes

$$W_{k'k} = \frac{2\pi D^2 |\Delta k|^2}{\beta\mathcal{N}\omega_{\text{LA}}^2(\Delta k)} \delta(\mathcal{E}(k') - \mathcal{E}(k)). \quad (2.134)$$

Typically, one substitutes the number of points in the reciprocal cell \mathcal{N} by the volume of the unit cell V_{UC} . This yields a quite general expression for the transition rate:

$$W_{k'k} = \frac{2\pi D^2 |\Delta k|^2}{\beta V_{\text{UC}} \omega_{\text{LA}}^2(\Delta k)} \delta(\mathcal{E}(k') - \mathcal{E}(k)). \quad (2.135)$$

This expression will be further simplified using the approximations made by Bardeen and Shockley in section 2.7.3. However, before this is done, the Boltzmann transport equation and the relaxation time approximation shall be discussed first in section 2.7.1 and 2.7.2.

2.7 Charge transport

2.7.1 Transition probabilities and Boltzmann equation

Transport is always a non-equilibrium N -particle phenomenon. In terms of classical mechanics, the state of such a system can be formulated as a point $X \in \mathbb{R}^{2Nd}$ in a $2Nd$ -dimensional phase space.[39] According to Boltzmann, alternatively, one can imagine a swarm of N particles moving in a $2d$ -dimensional phase space. Let X be the coordinate vector in this phase space and introduce[39]

$$f(X, t) d^d X . \quad (2.136)$$

This measure contains the number density $f(X, t)$ in the volume $d^d X$ around the phase space coordinate X , with the normalization

$$\int f(X, t) d^d X = N . \quad (2.137)$$

Averages of some function H over the ensemble of particles are calculated according to

$$\langle H \rangle = \frac{\int f(X, t) H(X) d^d X}{\int f(X, t) d^d X} . \quad (2.138)$$

For charge transport in the semi-classical picture, the N -particle phase space becomes six-dimensional, with the volume element $d^3 r d^3 k$. [21, 42] The averages for a homogeneous system in this case become

$$\langle H \rangle = \frac{\int f(k) H(k) d^3 k}{\int f(k) d^3 k} , \quad (2.139)$$

$$= \frac{2}{(2\pi)^3 n} \int f(k) H(k) d^3 k . \quad (2.140)$$

Here, $n = N/V_{\mathcal{UC}}$ and the normalization was chosen such[46], that

$$\frac{2V_{\mathcal{UC}}}{(2\pi)^3} \int f(k, t) d^3 k = N \quad \iff \quad \int f(k, t) d^3 k = \frac{(2\pi)^3 n}{2} . \quad (2.141)$$

One can derive the so-called Boltzmann equation (BE), the core statement of which is, that $f(r, k, t)$ will assume a stationary state under external influence. External influences can either be fields (labeled by field), (un-)directed diffusion (diff) or collisions with other (pseudo-)particles (coll). The equation reads[21, 36]

$$\left. \frac{df(r, k, t)}{dt} \right)_{\text{tot}} = \left. \frac{\partial f}{\partial t} \right)_{\text{coll}} + \left. \frac{\partial f}{\partial t} \right)_{\text{field}} + \left. \frac{\partial f}{\partial t} \right)_{\text{diff}} = 0. \quad (2.142)$$

For the collision or scattering term, one can in the case of elastic scattering write

$$\left. \frac{\partial f}{\partial t} \right)_{\text{coll}} = \sum_{k'} \underbrace{[f(k')(1 - f(k))W_{kk'}]}_{\text{rate in}} - \underbrace{[f(k)(1 - f(k'))W_{k'k}]}_{\text{rate out}}. \quad (2.143)$$

This is just a balance of processes which scatter into state k and those which scatter out of k . The transition probabilities are given here through (2.135). In the regime, where there are only few charge carriers ($f_k \ll 1$), e. g. in semi-conductors, the collision term can be approximately written as[36]

$$\left. \frac{\partial f}{\partial t} \right)_{\text{coll}} = \sum_{k'} [f(k')W_{kk'} - f(k)W_{k'k}]. \quad (2.144)$$

Next, for the field term, one uses a variant of Liouville's theorem on phase space volume invariance and the semi-classical EoM (2.90) to write[21]

$$f(r, k, t) = f(r, k - \dot{k}t, 0), \quad (2.145)$$

so that

$$\left. \frac{\partial f}{\partial t} \right)_{\text{field}} = -q \nabla_k f \cdot \dot{k} = -q \nabla_k f \cdot E. \quad (2.146)$$

Here, q is the charge of the carrier particle and ∇_k means the gradient with respect to the semiclassical momentum coordinates. A similar argument can be used for the diffusion term, by which it becomes

$$\left. \frac{\partial f}{\partial t} \right)_{\text{diff}} = -\langle v \rangle(k) \cdot \nabla f. \quad (2.147)$$

For small field strengths and if the number of charge carriers is small, the distribution function f will not differ much from the equilibrium quantity, i. e. the Fermi-Dirac distribution, so that one can write

$$f = f^\circ + g, \quad (2.148)$$

where f° is the Fermi–Dirac distribution,

$$f^\circ(k) = \frac{1}{e^{\beta\epsilon(k)-\mu} + 1}, \quad (2.149)$$

and g contains all non-equilibrium information on the swarm of charge carriers.

Using all these approximations, the BE becomes

$$v(k) \cdot \left(\nabla g + qE \frac{df^\circ}{d\epsilon} \right) + qE \cdot \nabla_k g = \sum_{k'} (f(k') - f(k)) W_{k'k}. \quad (2.150)$$

Instead of a direct solution of this equation, in the following the so-called relaxation time approximation (RTA) will be discussed. A direct solution using Monte Carlo (MC) techniques can be found in ref. [60] by Jacoboni and Reggiani. A further discussion of the BE is given in refs. [47] by Jünger and [46] by Jacoboni.

2.7.2 The relaxation time approximation

The relaxation time approximation states, that one can write for the collision term of the BE in the manner of a difference quotient like[21, 36]

$$\left. \frac{\partial f}{\partial t} \right)_{\text{coll}} = -\frac{g}{\mathcal{T}}. \quad (2.151)$$

This means, one makes the approximation that if all other sources for changing f are switched off and only scattering remains, the distribution f will return to the equilibrium distribution f° during the eponymous relaxation time \mathcal{T} . For the form of the collision term this implies[36]

$$\left. \frac{\partial f}{\partial t} \right)_{\text{coll}} = \sum_{k'} g(k') W_{kk'} - g(k) \sum_k W_{k'k} = \frac{-g(k)}{\mathcal{T}} \implies \frac{1}{\mathcal{T}} = \sum_{k'} W_{k'k}. \quad (2.152)$$

This is equivalent to the assumption that there is no back scattering into the state k . Moreover, if the transition rates $W_{k'k}$ are known, the relaxation time can be calculated.

2.7.3 The Bardeen–Shockley relaxation time

To calculate a relaxation time for the deformation potential interaction, one returns to the transition rate expression (2.135),

$$W_{k'k} = \frac{2\pi D^2 |\Delta k|^2}{\beta V_{\mathcal{UC}} \omega_{\text{LA}}^2(\Delta k)} \delta(\mathcal{E}(k') - \mathcal{E}(k)).$$

This goes back to the seminal work of Bardeen and Shockley.[24] There, they made simple assumptions on the dispersion relation of the longitudinal acoustic phonon and the form

of the band energies, which are introduced in the following. The whole derivation follows closely the one given by Jacoboni[46].

First, one requires that $|\Delta k|$ is small. Then, using a linear approximation, one can express the phonon dispersion relation as $\omega_{\text{LA}}(\Delta k) \approx c_s |\Delta k|$, where c_s is the sound velocity in the crystal, i. e. the group velocity of the phonon:

$$W_{k'k} = \frac{2\pi D^2}{\beta V_{\text{UC}} c_s^2} \delta(\mathcal{E}(k') - \mathcal{E}(k)), \quad (2.153)$$

Next, one can use the expression for the bulk modulus in an isotropic medium,

$$C_o = \rho c_s^2 \implies c_s^2 = \frac{C_o}{\rho}. \quad (2.154)$$

However, here, the mass-weighted expression for the displacement operator $U^i(x)$ was used, so the substitution is even simpler: one factor of $\rho^{-1/2}$ is then already absorbed in the sound velocity c_s , so that one arrives at

$$W_{k'k} = \frac{2\pi D^2}{\beta V_{\text{UC}} C_o} \delta(\mathcal{E}(k') - \mathcal{E}(k)). \quad (2.155)$$

Turning to the charge carriers: the band energies are assumed to have the simple form

$$\mathcal{E}(k) = \frac{(k - k_o)^2}{2m^*} = \frac{\kappa^2}{2m^*}, \quad (2.156)$$

giving the transition rate expression

$$W_{k'k} = \frac{2\pi D^2}{\beta V_{\text{UC}} C_o} \delta\left(\frac{(k' - k_o)^2}{2m^*} - \frac{(k - k_o)^2}{2m^*}\right), \quad (2.157)$$

$$= \frac{4\pi |m^*| D^2}{\beta V_{\text{UC}} C_o} \delta((\kappa')^2 - \kappa^2). \quad (2.158)$$

Here, an identity for the δ -distribution was used:

$$\delta(ax) = \frac{1}{|a|} \delta(x). \quad (2.159)$$

In (2.158), κ and κ' are the distances to the band extremum in reciprocal space.

Finally, one uses another identity for the δ -distribution:

$$\delta(f(x)) = \sum_i \frac{\delta(x - x_n)}{|f'(x_n)|}, \quad (2.160)$$

where the x_n are the roots of f , i. e. where $f(x_n) = 0$, and f' denotes the first derivate of f .

This yields the expression

$$\delta((\kappa')^2 - (\kappa)^2) = \frac{1}{2\kappa} \delta(\kappa' - \kappa). \quad (2.161)$$

Using this, gives the following transition rate:

$$W_{k'k} = \frac{2\pi|m^*|D^2}{\beta V_{uc} C_o \kappa} \delta(\kappa' - \kappa). \quad (2.162)$$

This expression (it is only meaningful within an integral) can be used to calculate the relaxation time, where the sum over k' is replaced by an integral over spherical coordinates*:

$$\frac{1}{\mathcal{T}(\kappa)} = \frac{V_{uc}}{(2\pi)^3} \iiint \frac{2\pi|m^*|D^2}{\beta V_{uc} C_o \kappa} \delta(\kappa' - \kappa) (\kappa')^2 \sin \vartheta \, d\kappa' \, d\vartheta \, d\varphi, \quad (2.163)$$

$$= \frac{|m^*|D^2 \kappa}{\pi \beta C_o}. \quad (2.164)$$

After eliminating the integral over κ' using the attribute of the δ -distribution, what remains is a trivial integral over the angular coordinates which yields 4π .

The expression for the relaxation time is thus

$$\mathcal{T}(\kappa) = \frac{\pi \beta C_o}{|m^*|D^2} \frac{1}{\kappa}. \quad (2.165)$$

Solving (2.156) for κ and inserting this into (2.165), gives

$$\mathcal{T}(\mathcal{E}) = \frac{\pi \beta C_o}{\sqrt{2}|m^*|^{3/2} D^2} \frac{1}{\mathcal{E}^{1/2}}. \quad (2.166)$$

The expression in (2.166) is used in section 2.7.6 to give the expression for the mobility of charge carriers scattering with LA phonons. Before this, a generalization of the Bardeen–Shockley deformation potential model for a direction dependent relaxation time will be introduced.

2.7.4 A generalization of the Bardeen–Shockley relaxation time

Consider the case, in which the deformation potential tensor has up to three non-degenerate eigenvalues as done e. g. by Herring and Vogt[58]. In this case, the analog to (2.124) is

$$g_s(q) = \begin{cases} D_{ij} \hat{q}^i \hat{q}^j |q| & s = \text{LA}, \\ 0 & s = \text{TA}_1, \text{TA}_2. \end{cases} \quad (2.167)$$

*The radius is measured as the distance from k_o , ϑ is the angle between $k' - k_o$ and $k - k_o$ measured from $k - k_o$ and φ is a polar angle defined accordingly.

For the expression $D_{ij}\hat{q}^i\hat{q}^j$ the following short notation is introduced:

$$D(\hat{q}) = D_{ij}\hat{q}^i\hat{q}^j. \quad (2.168)$$

The total transition rate(2.135) becomes in this case, writing $q = \Delta k$,

$$W_{k'k} = \frac{2\pi D^2(\hat{q})|q|^2}{\beta V_{uc}\omega^2(q)}\delta(\mathcal{E}(k') - \mathcal{E}(k)). \quad (2.169)$$

Instead of the bulk modulus, now, Young's modulus $Y(\hat{q})$ is introduced,

$$\omega^2(q) \approx c_s^2(\hat{q})|q|^2, \quad (2.170)$$

$$= c_{ijrs}\hat{q}^i\hat{q}^j\hat{q}^r\hat{q}^s|q|^2, \quad (2.171)$$

$$= Y(\hat{q})|q|^2, \quad (2.172)$$

yielding the transition rate

$$W_{k'k} = \frac{2\pi D^2(\hat{q})}{\beta V_{uc}Y(\hat{q})}\delta(\mathcal{E}(k') - \mathcal{E}(k)). \quad (2.173)$$

For the band energies in the argument of the δ -distribution, write

$$\mathcal{E}(k) = \frac{(k - k_o)^2}{2m^*(\vartheta, \varphi)} = \frac{\kappa^2}{m^*(\vartheta, \varphi)}. \quad (2.174)$$

The root of the δ -distribution argument is

$$\frac{(\kappa')^2}{2m^*(\vartheta, \varphi)} - \frac{\kappa^2}{2m^*(0, \varphi)} = 0 \implies \kappa' = \frac{m^*(\vartheta, \varphi)}{m^*(0, \varphi)}\kappa. \quad (2.175)$$

Then, using the two identities for the δ -distribution from section 2.7.3, one finds

$$W_{k'k} = \frac{2\pi D^2(\hat{q})m^*(0, \varphi)}{\beta V_{uc}Y(\hat{q})} \frac{1}{\kappa} \delta\left(\kappa' - \frac{m^*(\vartheta, \varphi)}{0, \varphi}\kappa\right). \quad (2.176)$$

With this, one calculates the reciprocal relaxation time:

$$\frac{1}{\mathcal{T}} = \frac{1}{(2\pi)^2\beta} \iiint \frac{D(\hat{q})m^*(0, \varphi)}{Y(\hat{q})} \frac{(\kappa')^2}{\kappa} \sin(\vartheta) \delta\left(\kappa' - \frac{m^*(\vartheta, \varphi)}{m^*(0, \varphi)}\kappa\right) d\kappa' d\vartheta d\varphi. \quad (2.177)$$

Calculating the κ' -integral yields

$$\frac{1}{\mathcal{T}} = \frac{\kappa}{(2\pi)^2\beta} \iint \frac{D(\hat{q})[m^*(\vartheta, \varphi)]^2}{Y(\hat{q})m^*(0, \varphi)} \sin \vartheta d\vartheta d\varphi. \quad (2.178)$$

Writing unit vectors, $\widehat{k k_o} = \frac{k - k_o}{|k - k_o|}$ and $\widehat{k' k_o}$, instead of spherical angles and introducing the area element $d^2\Omega' = \sin(\vartheta) d\vartheta d\varphi$, one has the reciprocal relaxation time

$$\frac{1}{\mathcal{T}} = \frac{\kappa}{(2\pi)^2\beta} \iint \frac{D(\widehat{k' k_o} - \widehat{k k_o}) [m^*(\widehat{k' k_o})]^2}{Y(\widehat{k' k_o}) m^*(\widehat{k k_o})} d^2\Omega' . \quad (2.179)$$

For convenience, the a shorthand notation for the integral is introduced:

$$\mathcal{I}(\widehat{k k_o}) = \frac{1}{4\pi} \iint \frac{D(\widehat{k' k_o} - \widehat{k k_o}) [m^*(\widehat{k' k_o})]^2}{Y(\widehat{k' k_o}) m^*(\widehat{k k_o})} d^2\Omega' . \quad (2.180)$$

So, finally, the expression for the (reciprocal) relaxation time is given by

$$\frac{1}{\mathcal{T}(\kappa, \widehat{k k_o})} = \frac{\kappa \mathcal{I}(\widehat{k k_o})}{\pi\beta} \iff \mathcal{T}(\kappa, \widehat{k k_o}) = \frac{\pi\beta}{\kappa \mathcal{I}(\widehat{k k_o})} . \quad (2.181)$$

Inserting isotropic values for Young's modulus, the deformation potential, and the effective mass gives the expression of (2.165).

Note, that the value of having this expression may not be as great as it may initially seem. That is, because of the breakdown of Matthiesen's rule,

$$\frac{1}{\mathcal{T}} = \sum_s \frac{1}{\mathcal{T}_s}, \quad s : \text{scattering sources} , \quad (2.182)$$

in the case of a dependence of the relaxation time on the carrier wave vector k . Without the dependence on k , the Bardeen–Shockley relaxation time for scattering with LA phonons would give an upper limit for the relaxation time if all other scattering sources are neglected. This feature is lost if the relaxation time depends on k . However, if one assumes that the scattering of LA phonons is predominant, the regions of high \mathcal{T} and low \mathcal{T} should still have a meaning insofar favoured directions of charge carrier mobility are concerned. For the connection between mobility and relaxation time refer to section 2.7.6.

Another case shall be discussed here: the case of isotropic Young modulus and deformation potential, i. e. $Y(\hat{q}) = C_o$ and $D(\hat{q}) = D$, when the effective mass is still described by the anisotropic model for a warped band. Then, the integral \mathcal{I} becomes

$$\mathcal{I} = \frac{1}{4\pi} \frac{D^2}{C_o} \iint \frac{[m^*(\vartheta, \varphi)]^2}{m^*(0, \varphi)} \sin \vartheta d\vartheta d\varphi . \quad (2.183)$$

The integral

$$\bar{m}^* = \frac{1}{4\pi} \iint \frac{[m^*(\vartheta, \varphi)]^2}{m^*(0, \varphi)} \sin \vartheta d\vartheta d\varphi , \quad (2.184)$$

defines a mean effective mass.

If the changes of $m^*(\vartheta, \varphi)$ are not too large in the direction of ϑ , the expression

$$\bar{m}^* = \frac{1}{4\pi} \iint m^*(\vartheta, \varphi) \sin \vartheta \, d\vartheta \, d\varphi, \quad (2.185)$$

which one intuitively assigns for a mean effective mass, is a good approximation.

Note that this formulation of a generalized, k direction dependent relaxation time was specifically derived for this thesis to be able to account for the situation in complex solids such as MOFs.

2.7.5 Conductivity and mobility

In the case of an external electric field E in which the charge carriers of the crystal move, one has the general BE:

$$\left. \frac{\partial f}{\partial t} \right)_{\text{field}} + \left. \frac{\partial f}{\partial t} \right)_{\text{coll}} = 0. \quad (2.186)$$

Using the approximations introduced in section 2.7.1 and 2.7.2, one finds[36]

$$-qE \cdot \nabla_k f^\circ - \frac{g(k)}{\mathcal{T}} = 0, \quad (2.187)$$

which can be reformulated to

$$g(k) = -q\mathcal{T}E \cdot \underbrace{\nabla_k \mathcal{E}(k)}_{v(k)} \frac{df^\circ}{d\mathcal{E}} = -q\mathcal{T}E \cdot v(k) \frac{df^\circ}{d\mathcal{E}}. \quad (2.188)$$

This is used in the expression for the current density j , which describes the charge carrier density qn moving with an average velocity $\langle v \rangle$:

$$j^n = qn \langle v^n \rangle, \quad (2.189)$$

$$= \frac{q}{(2\pi)^3} \int v^n(k) f(k) \, d^3k, \quad (2.190)$$

$$= \frac{q}{(2\pi)^3} \int v^n(k) g(k) \, d^3k. \quad (2.191)$$

In the linear response regime, the tensor with the elements

$$\sigma_{mn} = \frac{\partial j_n}{\partial E^m} = -\frac{q^2}{(2\pi)^3} \int \mathcal{T}(k) v_n(k) v_m(k) \frac{df^\circ}{d\mathcal{E}} \, d^3k, \quad (2.192)$$

is the conductivity tensor*. Conversely, this means the conductivity links the electric field E to the current density j , so that[35]

$$j_i = \sigma_{il} E_l. \quad (2.193)$$

The source of the mean velocity in (2.189) is the electric field and one defines[23] the quantity moderating between the two as the charge carrier mobility[†],

$$\mu_{ij} = \frac{\langle v_i \rangle}{E_j}. \quad (2.194)$$

Note, that the mobility may depend on the electric field itself as the drift velocity is a linear function of the latter only at small field strengths.[23] For this regime, one may expand the drift velocity in terms of the electric field as

$$\langle v_i \rangle(E) = \langle v_i \rangle(0) + \left[\frac{\partial \langle v_i \rangle}{\partial E_j} \right]_{E=0} E_j + \mathcal{O}(E^2) \quad (2.195)$$

which, together with $\langle v_i \rangle(0) = 0$, leads to the linearized expression

$$\mu_{ij} = \left[\frac{\partial \langle v_i \rangle}{\partial E_j} \right]_{E=0} \quad (2.196)$$

or equivalently to the tensor equation

$$\langle v_i \rangle = \mu_{ij} E_j. \quad (2.197)$$

With this, it is possible to derive an equation which relates the conductivity and the mobility:

$$\sigma_{il} = \frac{\partial j}{\partial E_l} = \frac{\partial j_i}{\partial \langle v_k \rangle} \frac{\partial \langle v_k \rangle}{\partial E_l} = \frac{\partial j_i}{\partial \langle v_k \rangle} \mu_{kl}. \quad (2.198)$$

In a last step, one uses (2.189) and relabels the indices to yield

$$\sigma_{ij} = qn\mu_{ij}. \quad (2.199)$$

This means, that although the conductivity is also determined by the charge carrier density, the important bit to consider, if one assumes that the carrier density is constant, is the mobility. Through this it is possible to make qualitative comparisons between a measured conductivity and a calculated mobility.

*Its elements are given in units of $\Omega^{-1} \text{cm}^{-1}$ or in atomic units of $e^2 \hbar^{-1} a_0^{-1}$.

†In $\text{cm}^2 \text{V}^{-1} \text{s}^{-1}$ or in atomic units ea_0^2/\hbar .

2.7.6 Mobility and relaxation time

In the following, the connection between mobility and relaxation time shall be highlighted. To arrive there, one considers at first an expression for the drift velocity.

$$\langle v \rangle = -\frac{2q}{(2\pi)^3 n} E_m \int \mathcal{T}(k) v_n(k) v^m(k) \frac{df^\circ}{d\mathcal{E}} d^3k . \quad (2.200)$$

The mobility tensor elements are then

$$\mu_{nl} = \frac{\partial \langle v_n \rangle}{\partial E_l} , \quad (2.201)$$

$$= -\frac{2q}{(2\pi)^3 n} \delta_{ml} \int v_n(k) v^m(k) \mathcal{T}(k) \frac{df^\circ}{d\mathcal{E}} d^3k , \quad (2.202)$$

$$= -\frac{2q}{(2\pi)^3 n} \int v_n(k) v_l(k) \mathcal{T}(k) \frac{df^\circ}{d\mathcal{E}} d^3k , \quad (2.203)$$

and the scalar mobility is hence given by

$$\mu = \frac{1}{3} \mu_i^i = -\frac{2q}{3(2\pi)^3 n} \int \mathcal{T}(k) v^2(k) \frac{df^\circ}{d\mathcal{E}} d^3k . \quad (2.204)$$

For the squared semiclassical velocity $v^2(k)$ in the case of a parabolic band $\mathcal{E}(\kappa) = \kappa^2/(2m^*)$, one can write

$$v^2(k) = \frac{2}{m^*} \left(\frac{\kappa^2}{2m^*} \right) = \frac{2}{m^*} \mathcal{E} . \quad (2.205)$$

Substituting this into (2.204) yields

$$\mu = -\frac{4q}{3(2\pi)^3 n m^*} \int \mathcal{T} \mathcal{E} \frac{df^\circ}{d\mathcal{E}} d^3k . \quad (2.206)$$

In section 2.7.1 the requirement was used that $f(k) \ll 1$. In this case, the Fermi–Dirac equilibrium distribution may be approximated by a Maxwell-distribution. Thus,

$$\mu = \frac{4q\beta}{3(2\pi)^3 n m^*} \int \mathcal{T} \mathcal{E} f^\circ(\mathcal{E}) d^3k . \quad (2.207)$$

Next use the well-known expression $\langle \mathcal{E} \rangle = 3/(2\beta)$ to write

$$\mu = \frac{2q}{(2\pi)^3 n m^* \langle \mathcal{E} \rangle} \int \mathcal{T} \mathcal{E} f^\circ(\mathcal{E}) d^3k . \quad (2.208)$$

Then, writing the remaining integral as an average, the mobility is given by

$$\mu = \frac{q}{m^*} \frac{\langle \mathcal{T} \mathcal{E} \rangle}{\langle \mathcal{E} \rangle} = \frac{q\tau}{m^*} . \quad (2.209)$$

It is convenient, to consider $\langle \mathcal{T}\mathcal{E} \rangle / \langle \mathcal{E} \rangle$ as a mean relaxation time τ .

For the Bardeen–Shockley expression of the relaxation time, $\langle \mathcal{T}\mathcal{E} \rangle$ can be calculated as

$$\langle \mathcal{T}\mathcal{E} \rangle = \frac{2}{(2\pi)^3 n} \int \mathcal{T}\mathcal{E} K e^{-\beta\mathcal{E}} d^3k, \quad (2.210)$$

$$= \frac{2C_0 K}{\pi n D^2} \int_0^\infty \xi^3 e^{-\beta\xi^2} d\xi, \quad (2.211)$$

$$= \frac{C_0 K}{\pi \beta n D^2}. \quad (2.212)$$

The constant K can be calculated from

$$n = \frac{N}{V_{uc}} = \frac{1}{V_{uc}} \frac{V_{uc}}{(2\pi)^3} \int K e^{-\beta\mathcal{E}} d^3k, \quad (2.213)$$

$$= \frac{\sqrt{8}|m^*|^{3/2} K}{\pi^2} \int_0^\infty \xi^2 e^{-\beta\xi^2} d\xi, \quad (2.214)$$

$$= \frac{|m^*|^{3/2} K}{\sqrt{2\pi}\beta^{3/2}}. \quad (2.215)$$

This yields

$$n = \frac{|m^*|^{3/2}}{\sqrt{8\pi^{3/2}}\beta^{3/2}} K \iff K = \frac{\sqrt{8\pi^{3/2}}\beta^{3/2}}{|m^*|^{3/2}} n. \quad (2.216)$$

Putting everything together one finds the relaxation time given by Bardeen and Shockley[24]:

$$\tau = \frac{\langle \mathcal{T}\mathcal{E} \rangle}{\mathcal{E}} = \frac{\sqrt{8\pi}\beta^{3/2}C_0}{3D^2|m^*|^{3/2}}. \quad (2.217)$$

Substitution into (2.209) yields

$$\mu = \frac{\sqrt{8\pi}q\beta^{3/2}C_0}{3D^2|m^*|^{5/2}}. \quad (2.218)$$

The scalar mobility of the charge carriers which is restricted through the scattering of carrier particles and LA phonons is thus mainly determined by three quantities: the bulk modulus C_0 , the deformation potential D , and the effective mass m^* . One wants the latter two to be small and the first one to be large.

3 Metal-organic frameworks

3.1 A versatile family of compounds

MOFs[61–63] are a class of network materials built from metal centers and organic ligands. As an example, a part of the well-known HKUST-1 MOF is shown in figure 3.1a. There is some MOF jargon: the ligands are commonly called linkers in the field. Furthermore, the metal centers, which can be metal ions, small metal clusters or even specifically designed metal-organic precursors, are called secondary building units (SBUs)[62].

The general term for the various synthetic approaches yielding net-like materials is called reticular* chemistry or synthesis.[61, 64] It often relies on the self assembly of the metal species with the linker molecules under solvothermal† conditions.[62] However, various specialized approaches can be taken, like a layer-by-layer approach atop a self-assembled monolayer (SAM)[65] or a post-synthetic exchange of the metal species[66, 67], to name only two explicitly.

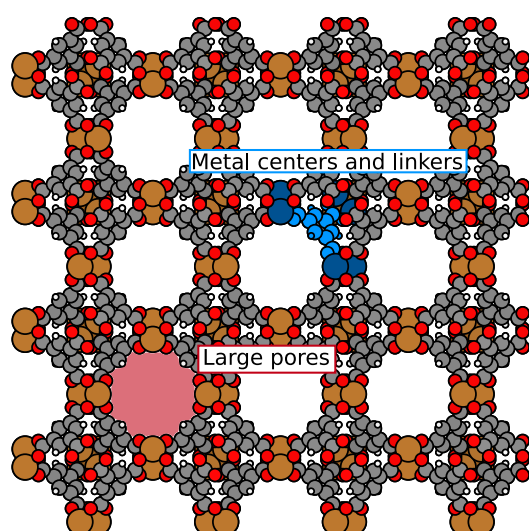
The building-block principle underlying MOF design manifests itself in the isorecticular principle, which states that one may change the linkers and SBUs—and thus the chemical nature of the MOF—but the net topology will stay the same if the connectivity properties of those components does not change.[6] A simple example for this behavior is studied in chapter 4 for a series of MOFs with a common linker and different (atomic) metal centers.

A striking feature of many MOFs are their large pores (figure 3.1a). This is included as a possible but not necessary feature into the 2013 definition of the International Union of Pure and Applied Chemistry (IUPAC).[5] Typically, the porosity is greater than 50 %, with internal surface areas in the order of magnitude of about $1 \times 10^3 \text{ m}^2 \text{ g}^{-1}$ to $1 \times 10^4 \text{ m}^2 \text{ g}^{-1}$. [6] This illustrates the original interest in MOF research as an organometallic equivalent to zeolites.[8] For the last two decades, the interest here, lies in particular in fuel storage and filtering applications.[6]

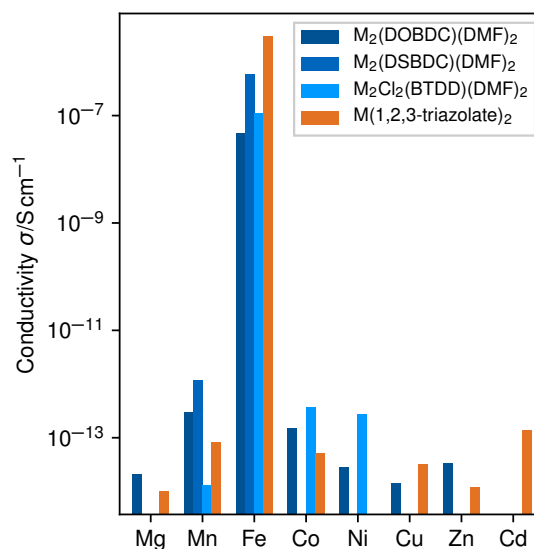
However, the field of MOF research is not limited to this, due to the structural diversity of these hybrid materials: further applications include catalyst materials[11, 12], proton conducting membranes for fuel cells[9, 10] and last but not least: various sorts of sensing applications[14, 68]. The usages and limitations of MOFs in these cases shall be shortly discussed in the following section.

*From the latin word *reticulum*, meaning net. Thus, reticular synthesis can be understood as the synthesis of netlike materials. A net, in this case, can also be a three-dimensional interconnected structure.

†Within a solvent at elevated temperature.



(a) Constitution of a metal-organic framework. Metal centers are marked in dark blue, linker atoms in light blue. In this example, copper ions are linked via trimesic acid (1,3,5 benzene tricarboxylic acid, BTA) anions to the form one of the well-known HKUST-1, $\text{Cu}_3(\text{BTA})_2$, framework.



(b) Conductivities of various metal organic frameworks. Data taken from the supplement of ref. [26].

Figure 3.1: Some general features of metal-organic frameworks.

3.2 Electrical conductivity in metal-organic framework crystals

Considering sensors in general, one of the features one can exploit is the electrical conductivity and specifically, how it changes under influence of some analyte.[15] One speaks of a chemiresistor.[15] Without any problem one can accept, that the state of the sensor prior to usage should be well-defined. However, establishing such a state should also become increasingly difficult with increasing complexity of the sensor material.

This requirement calls for an elaborate purification procedure *post synthesis*. Nevertheless, there will be many defects, i. e. deviations from the pristine crystal. Among those, there could be different absorbed species in the pores of the network, linkers or SBUs may be missing or other impurities may be present. Furthermore, the material could be difficult to crystallize. Due to all of these difficulties with the real material, one has to define a point of reference for the theoretical models. In the case of three-dimensionally interconnected framework materials, which are the chemical basis for the studies in this thesis, this is provided by a bulk unit cell. Note, that the surface will likely play an important part for a MOF, however it was omitted for the studies presented in this thesis.

The majority of MOFs does not show electrical conductivity, which is illustrated for a small group of compounds in Figure 3.1b. Even though, the number of electrically

conductive MOFs which are found has been increasing for the last few years, they are still a sparse subset of MOF design space. In particular iron MOFs seemed to be ideal candidates for conductive framework materials at that time.[26, 69] In the meanwhile, also other materials have been found which look promising.[19]

In the following, the focus lies on metal triazolate crystals and in particular on iron triazolate and absorbate structures thereof. This class of compounds was chosen for these studies as notably iron triazolate showed high electrical conductivity[26] for a MOF (Figure 3.1b).

4 Aspects of semiconductivity in soft, porous, metal-organic framework crystals

Large parts of this chapter are already published in ref. [1]. Text, figures, and tables are reproduced or reproduced in parts from ref. [1] with permission. Copyright 2019 AIP Publishing.

In the first part of this thesis, Bardeen–Shockley deformation potential theory for the interaction of charge carriers with LA phonons of low crystal momentum (sections 2.6.1 and 2.6.2) has been established. Furthermore, a formula for the charge carrier mobility from this theory based on an expression for the relaxation time (sections 2.7.3 and 2.7.6) has been derived, which yields the mobility given by 2.218. The following chapter deals with the application of this theory to a specific set of MOF crystals, namely cubic transition metal(II) 1,2,3-triazolates, $M(\text{ta})_2$, of space group $Fd\bar{3}m$, no. 227, where the elemental species of the metal center is either iron, ruthenium or zinc. For the linker anion the abbreviation ta^- , following the convention of Sun et al.[26], is used.

4.1 Methodology

4.1.1 Computational details

DFT calculations were performed using the all-electron numeric atom-centered orbital (NAO) basis DFT code FHI-aims*.[70] We use the NAO “light” basis sets implemented therein.[70] Electronic XC is treated using the GGA functional PBE[53] for structural optimizations. For all other electronic structure calculations, the revised Heyd–Scuseria–Ernzerhof (HSE)[71, 72] hybrid functional (HSE06) is employed with standard parameters.

All data evaluation is performed using homemade Python codes. This small package is mainly based on the Numpy,[73] Scipy,[74] Matplotlib,[75], and ASE[76] packages. Furthermore, the Quadpy[77] package is used to generate spherical Lebedev integration grids. Parts of the Pymatgen package[78] are used for structural analysis.

*Fritz-Haber-Institute *ab initio* molecular simulations.

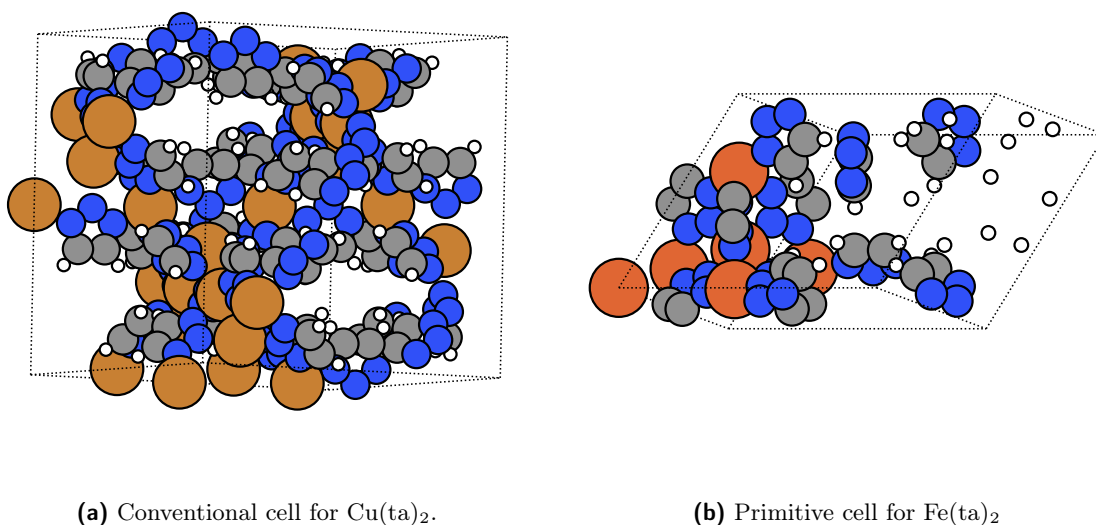


Figure 4.1: Crystal structures of cubic $\text{Cu}(\text{ta})_2$ and cubic $\text{Fe}(\text{ta})_2$.

4.1.2 Generation of the crystal structures

To obtain the different metal triazolate crystals, the metal centres in the corresponding cubic $\text{Cu}(\text{ta})_2$ structure are substituted. This base structure[79] is taken from the Cambridge Crystallographic Database (CSD) which has a well-defined subset of MOF structures.[80] All three crystals show face-centered cubic (FCC) space symmetry, so that the conventional cube-shaped unit cell is not the primitive cell. The conventional and the primitive cells are used in different contexts throughout the procedure, so both kinds of cells have to be optimized. For this purpose, the BFGS algorithm implemented in FHI-aims is used,[81] taking a trust radius of $0.01 \text{ eV } \text{\AA}^{-1}$ for the conventional and one of $0.001 \text{ eV } \text{\AA}^{-1}$ in case of the primitive cells.

4.1.3 Band structure calculations and the mean effective mass

Band structures are calculated using the reciprocal space paths connecting high symmetry points of the Brillouin zone. These paths are chosen following Setyawan and Curtarolo.[82] From the conventional band structures, the band extrema can be identified.

Next, consider the effective mass. Depending on the material, a description by a scalar (spherical band), a tensor (ellipsoidal band) or by an angular dependent function (warped band) has to be used.[46] The first case is just a special form of the second case, both of which are henceforth called a “well-behaved” band extremum in contrast to a warped one.

To evaluate the validity of the parabolic expansion around the band extremum and to find out which case—well-behaved or warped—applies, the state energies on an equally spaced grid centered on a band extremum are calculated, where the shape of the iso-energy

curves slightly above or below the respective extrema can thereby serve as a very rough criterion for the warping of the bands.

The increments of that grid are always chosen as $4.0 \times 10^{-3} a_0^{-1}$, reciprocal Bohr radii. This value was obtained due to its yielding numerically stable second finite difference quotients corresponding to the curvature at the band extremum. Diagonalization and inversion of the Hessian matrix at the extremum can be used to get the effective mass tensor in the case of a well-behaved extremum.

In the case of warped bands, one also needs to determine the angular dependencies of the effective masses $m^*(\vartheta, \varphi)$. To obtain these, one first interpolates the discrete calculated band energies, using the radial basis function interpolator of Scipy[74] and r^5 as radial basis functions. Next, using cubic splines, one interpolates in the directions $\hat{k}(\Omega_I)$ specified by a Lebedev grid $\Omega_I = (\vartheta_I, \varphi_I)$. [83] I enumerates the Lebedev grid points. Finally, calculating the second directional derivative at the band extremum, the values for $m^*(\Omega_I)$ are obtained.

In the simple Bardeen–Shockley model, only a scalar effective mass appears. Thus, it is necessary to calculate a mean value from either the effective mass tensor or the angular data. To achieve this, two different schemes are used: in case of a well-behaved band extremum, a harmonic mean

$$\bar{m}_\nu^*(k_o) = 3 \left(\sum_{i=1}^3 \frac{1}{m_{(i)}^*(k_o)} \right)^{-1} = \frac{3}{\text{tr } \epsilon_\nu''(k_o)}. \quad (4.1)$$

can be calculated. Here, $\epsilon_\nu''(k_o)$ denotes the Hessian matrix of the band energy surface at the extremum. The $m_{(i)}^*(k_o)$ are the principal values of the effective mass tensor.

In contrast to this, for a warped band, a Lebedev mean is calculated. This is defined by the Lebedev approximation[83] of the angular integral (2.185),

$$\bar{m}_\nu^*(k_o) = \frac{1}{4\pi} \iint m_\nu^*(k_o, \Omega) \sin \vartheta \, d\vartheta \, d\varphi, \quad (4.2)$$

$$\approx \sum_I w_I m_\nu^*(\Omega_I), \quad (4.3)$$

where Ω_I specifies a grid point and the constant coefficient cancels with the surface measure of the unit sphere. The w_I are the Lebedev integration weights. Note that the same notation for the harmonic mean average of the effective mass and for the Lebedev mean. This should be no problem as the former is only used in the case of well-behaved bands and the latter in the case of warped ones.

4.1.4 Elasticity and deformation potential tensors

Next to the effective mass, a solid's elastic properties are among the most important factors determining its electronic or hole conductivity. In section 2.4.2, the main quantities, i. e. the elasticity tensor, the strain tensor, and the stress tensor, were introduced.

Based thereupon, in the following section the focus lies on the question how one can determine the elasticity tensor and the bulk modulus in practice, when given some crystal structure. For the mobility, following Bardeen's and Shockley's motivation of a hydrostatically deformed solid, nevertheless only the bulk modulus is used.[24] However, rather than simply calculating the latter, the full elastic tensor is determined, enabling future studies using a generalization of the Bardeen–Shockley model which then uses the full tensorial or angular information for each descriptor (section 2.7.4).

As a notational peculiarity which is often used in elasticity theory, one introduces Voigt notation for symmetric, even-ranked tensors. The difference to common tensor notation expresses itself in several points. At first, the notational ones: the indices in Voigt notation, henceforth called Voigt indices, run from 1 to 6 and are defined by the mapping[22]

$$\begin{aligned} \alpha : (i, j) \in \{1, 2, 3\}^2 &\mapsto \{1, 2, 3, 4, 5, 6\}, \\ 11 &\mapsto 1 \quad 22 \mapsto 2 \quad 33 \mapsto 3 \\ 23 &\mapsto 4 \quad 13 \mapsto 5 \quad 12 \mapsto 6. \end{aligned} \tag{4.4}$$

Second, applied to symmetric even-ranked tensors Voigt indices denote a representation with half the number of indices. For example, symmetric rank-2 tensors A_{ij} have Voigt representations A_α which are denoted as a (6×1) -array,

$$\begin{pmatrix} A_{11} & A_{12} & A_{13} \\ & A_{22} & A_{23} \\ \text{sym} & & A_{33} \end{pmatrix} \sim \left(A_1 \quad A_2 \quad A_3 \quad A_4 \quad A_5 \quad A_6 \right)^T \iff A_{ij} \sim A_\alpha. \tag{4.5}$$

In the following, Voigt indices are distinguished from normal tensor indices by using lowercase Greek letters. Equivalently, a symmetric rank-4 tensor such as the elasticity tensor c_{ijrs} is representable by a 6×6 (symmetric) array $c_{\alpha\beta}$. Note, that a contraction of Voigt indices, $A_\alpha B_\alpha$, is equivalent to a two-index contraction, so that

$$\begin{aligned} A_\alpha B_\alpha := A_{ij} B_{ij} &= (A_{11} B_{11} + A_{22} B_{22} + A_{33} B_{33}) \\ &\quad + [2A_{23} B_{23} + 2A_{13} B_{13} + 2A_{12} B_{12}]. \end{aligned}$$

This is the main difference to conventional tensor notation and means that for a single Voigt index contraction products containing the off-diagonal elements need to be counted doubly. Here, the standard convention of elasticity theory is used, where e. g. for the strain tensor u elements $\alpha \geq 3$ are defined as $u_\alpha := 2u_{ij}$, where $ij \mapsto \alpha$, to account for this double counting. Thus tensor contractions formally reduce to a single index contraction. For example, using Voigt notation, Hooke's law becomes

$$s_\alpha = c_{\alpha\beta} u_\beta. \tag{4.6}$$

One wants to calculate the elements $c_{\alpha\beta}$ and by performing a DFT calculation, one can obtain the stress tensor. It follows that to determine the elasticity tensor, one has to choose a given form for the strain tensor and to find a way to invert Hooke's law. In the following, the method established by de Jong et al. to calculate the elastic properties is applied.[84] Therefore, the form chosen is the Green–Lagrange strain tensor

$$u(\gamma g) = \frac{1}{2} [F^\gamma(g)^T F^\gamma(g) - I] , \quad (4.7)$$

where the matrix $F^\gamma(g)$ is called a deformation gradient,[84] defined as

$$F^\gamma(g) = I + g(\hat{e}_a \otimes \hat{e}_b + \hat{e}_b \otimes \hat{e}_a), \quad (4.8)$$

$$= I + g\Lambda_S^\gamma. \quad (4.9)$$

Here, $\gamma \mapsto (a, b)$ is a Voigt index. g is a number denoting the magnitude of this deformation. In the following, a double index notation notation $G := \gamma g$ is used, with G running from e. g. 1 to $6N_g$, where N_g is the number of different values of g that are considered. The unit vectors \hat{e}_a denote the Euclidean basis vectors. It has to be stressed that in contrast to de Jong et al., here, a *symmetrized* deformation gradient is used. In their original formulation the term $\hat{e}_b \otimes \hat{e}_a$ is not present.[84] For equal values of g this effectively leads to larger deformations. Briefly*, this can be seen by realizing that the relation between the de Jong Λ -matrices, Λ_J^γ , and the symmetrized ones, Λ_S^γ , is

$$\Lambda_S^\gamma = 2(\Lambda_J^\gamma)_{\text{sym}}, \quad (4.10)$$

where sym denotes symmetrization. The Green–Lagrange strain tensor may, using the Λ -matrices, be written in the form

$$u_X(\gamma g) = g(\Lambda_X^\gamma)_{\text{sym}} + \frac{1}{2}g^2(\Lambda_X^\gamma)^T \Lambda_X^\gamma. \quad (4.11)$$

Then, using (4.10), and neglecting $\mathcal{O}(g^2)$ terms in the strain tensor, one finds an effective strain magnitude $2g$ in the symmetrized deformation gradient case, compared to the formulation of de Jong et al.

Through this procedure one has a strain tensor $u(G)$ for each value of G . Thus, one obtains a set of strain tensors which can be expressed in form of a $(6 \times 6N_g)$ -matrix \underline{u} using Voigt notation for each strain tensor,

$$\underline{u} = \begin{pmatrix} u_1(1, g_1) & u_1(1, g_2) & \cdots & u_1(1, g_N) & u_1(2, g_1) & \cdots & u_1(6, g_N) \\ u_2(2, g_1) & u_2(1, g_2) & \cdots & u_2(1, g_N) & u_2(2, g_1) & \cdots & u_2(6, g_N) \\ \vdots & \vdots & \vdots & \vdots & \vdots & \vdots & \vdots \\ u_6(1, g_1) & u_6(1, g_2) & \cdots & u_6(1, g_N) & u_6(2, g_1) & \cdots & u_6(6, g_N) \end{pmatrix}. \quad (4.12)$$

*A more thorough derivation is given in appendix III.

Subjecting the relaxed crystal unit cell to a deformation through $F^\gamma(g)$ and subsequently to a relaxation of the atomic positions under the constraint of a fixed unit cell, one further obtains a set of stress tensors $s(G)$ which are expressed similarly as \underline{s} . The Moore–Penrose pseudo-inverse

$$\underline{u}^+ := (\underline{u}^T \underline{u})^{-1} \underline{u}^T \quad (4.13)$$

of the strain tensor matrix then serves to solve the linear stress-strain relation, which is Hooke’s law, for the elastic tensor:

$$s_\alpha(G) = c_{\alpha\beta} u_\beta(G) \implies c_{\alpha\beta} = \sum_G s_\alpha(G) u_\beta^+(G). \quad (4.14)$$

At this point one can calculate basically any elastic property of the solid. However, for the Bardeen–Shockley model one is only interested in the scalar bulk modulus of the crystal. It is calculated from the elastic constants through the relation (2.73) given in section 2.4.3, which is also known as the Voigt average C_\circ^V ,

$$C_\circ^V := \frac{1}{9} c_{iirr} = \frac{c_{11} + c_{22} + c_{33} + 2(c_{23} + c_{13} + c_{12})}{9}. \quad (4.15)$$

Note that this is not the only way to calculate the average bulk modulus,[84, 85] but rather the most straightforward one. Here, however little difference in the mobilities between the different averages has been found.

Having established the main parameters describing the prevalence of acoustic phonons, the next important step is to determine the coupling of these phonons to the charge carrier dynamics. Yet, instead of calculating the coupling for each phonon separately, within Bardeen–Shockley theory only the coupling to the LA phonon is considered originally (sections 2.6.1 and 2.6.2). However, by using the macroscopically strained structures from which the elastic constants are determined, one expects that the deformation potential calculated represents more of an average influence of the all phonons onto the carriers in the form of the acoustic deformation potential D^{ac} , with a prevalence of the LA phonons.[25] Specifically, D^{ac} represents the influence of strain on the crystal’s electronic states.[45, 46]

Of particular interest is the shift of the band edge extremum energies as remarked in section 2.6.1, as only at the extremal points, the deformation potential only results from the effect of the macroscopic strain. Otherwise, there would be an intermixture with the group velocity of the charge carrier resulting from the band edge dispersion as stated by (2.111). It has to be repeated, that the band edge extremum energy is given with reference to some other energy changing with strain. Within a bulk crystal modeled by periodic boundary conditions this reference is the Fermi energy *under strain*, $\epsilon_F(u)$.

By neglecting terms $\mathcal{O}(u^2)$, one finds (2.105) which is written as a linear shift-strain relation

$$\Delta\delta\epsilon_\nu(u, k_\circ) = -D_{\nu ij}^{\text{ac}}(k_\circ)u_{ij}, \quad (4.16)$$

where $\Delta\delta\epsilon_\nu(u, k_\circ) := \delta\epsilon_\nu(u, k'_\circ) - \delta\epsilon_\nu(0, k_\circ)$ is the band shift at k_\circ under strain with respect to the unstrained band extremum.

From a technical point of view, this approach has the advantage that the determination of the deformation potential does not demand any further calculations beyond those necessary for the elasticity tensor, where one already gets a (γg) -set of band extremum shifts, $\Delta\delta\epsilon_\nu(G) := \Delta\delta\epsilon_\nu(u(G), k_\circ(G))$. Using again the pseudo-inverse \underline{u}^+ one can rewrite (4.16) as follows:

$$D_{\nu\alpha}^{\text{ac}}(k_\circ) = -\sum_G \Delta\delta\epsilon_\nu(G)u_\alpha^+(G). \quad (4.17)$$

However, the method has also a downside as the inversion of the equation relies heavily on the linearity of the shift-strain relation. If there are non-negligible quadratic terms, one can still apply this technique but introduces an error in the linear couplings, which depends on the magnitude of the induced strain and the magnitude of the quadratic couplings. One can compensate for this error by introducing a smart splitting of the strain matrix \underline{u} and the shift vector $\Delta\delta\epsilon$, given that the strain magnitudes one used are symmetric with respect to $g = 0$. This is described in section 6.1.

Several common definitions for deformation potential constants, for different positions and symmetries in the Brillouin zone, exist in the literature.[24, 45, 58] The Bardeen–Shockley deformation potential used here, is due to a hydrostatic compression of the crystal. Thus, we again use the decomposition of the strain tensor into a pure shear and a hydrostatic compression part (section 2.4.3 and eqs. 2.114 and 2.115). Concentrating on the hydrostatic compression part only, one finds the Bardeen–Shockley deformation potential, $D_\nu^{\text{BS}}(k_\circ) = D_{\nu ii}^{\text{ac}}(k_\circ)/33$, from a contraction of the underlying tensor elements.

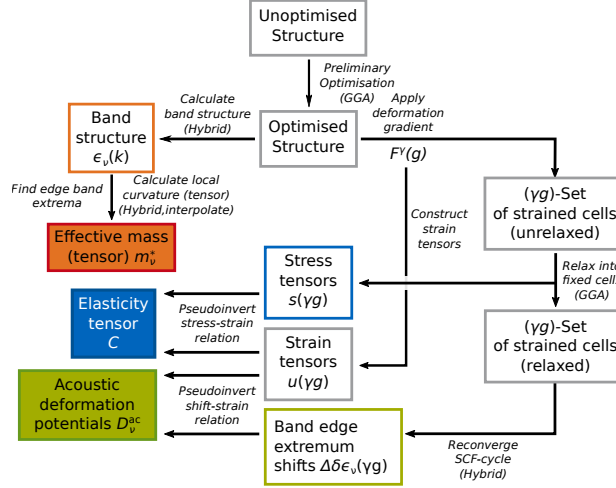


Figure 4.2: Basic workflow to obtain the quantities underlying the descriptors of the Bardeen–Shockley mobility. Reproduced with permission from ref. [1], © 2019 AIP Publishing.

4.2 Results and discussion

To obtain the elastic constants and the deformation potentials, several geometry optimizations on crystal structures with strained unit cells were performed (Figure 4.2). For each of these optimizations one has to be careful to use a sufficiently dense k -point grid as one breaks the symmetry of the unit cell through the straining of the base structure. The strained unit cells are generated using a deformation gradient as described in section 4.1.4. During the optimization process, the structures are relaxed within fixed strained cells and the analytical stress tensor[86] is calculated. Using the pseudo-inverse procedure of de Jong et al.[84] this, in turn, yields the elasticity tensor.

Comparing the increase in total energy $E(\gamma, g)$ of the various strained unit cells with relaxed atomic structure to the analytic behaviour one expects from elasticity theory, one gets a good agreement for the conventional unit cells (Figure 4.3). It shall be explicitly remarked here, that these results are not well reproduced using the primitive unit cells even for the comparably large cells of metal triazolate crystals. This behavior is also observed by de Jong et al. for many other materials.[84]

Using the relaxed structures in the strained cells, the self-consistent field (SCF) cycle is reconverged and one obtains the electronic structure of the strained crystal on the hybrid XC level. During each of these calculations, a band structure is generated as output. By means of the procedure described in section 4.1.4, the deformation potential tensors are computed.

The principal band gaps for all three $M(\text{ta})_2$ crystals are given in Table 4.1. For $\text{Fe}(\text{ta})_2$ and $\text{Zn}(\text{ta})_2$ band gaps of 4.11 eV and 5.96 eV are found, in accordance with the results of Sun et al.[26] The proposed $\text{Ru}(\text{ta})_2$ shows a slightly smaller band gap compared to $\text{Fe}(\text{ta})_2$. Nevertheless, the band gaps in all three pristine $M(\text{ta})_2$ compounds are far too large to

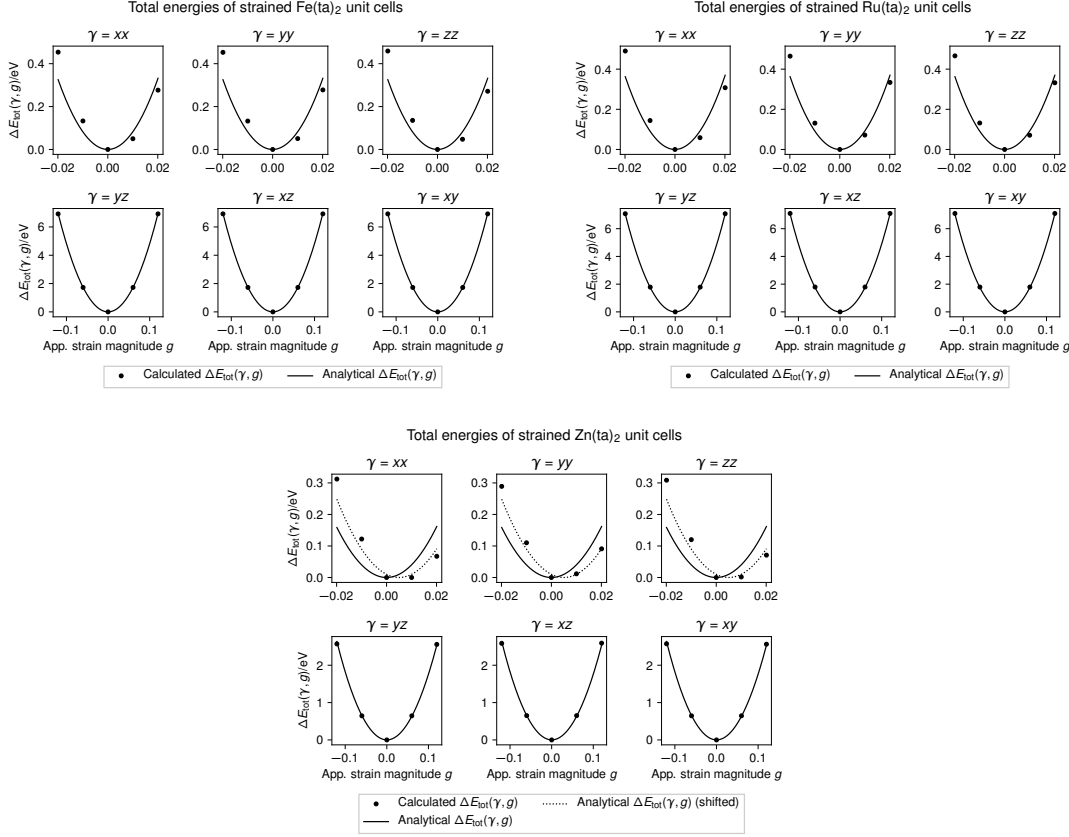
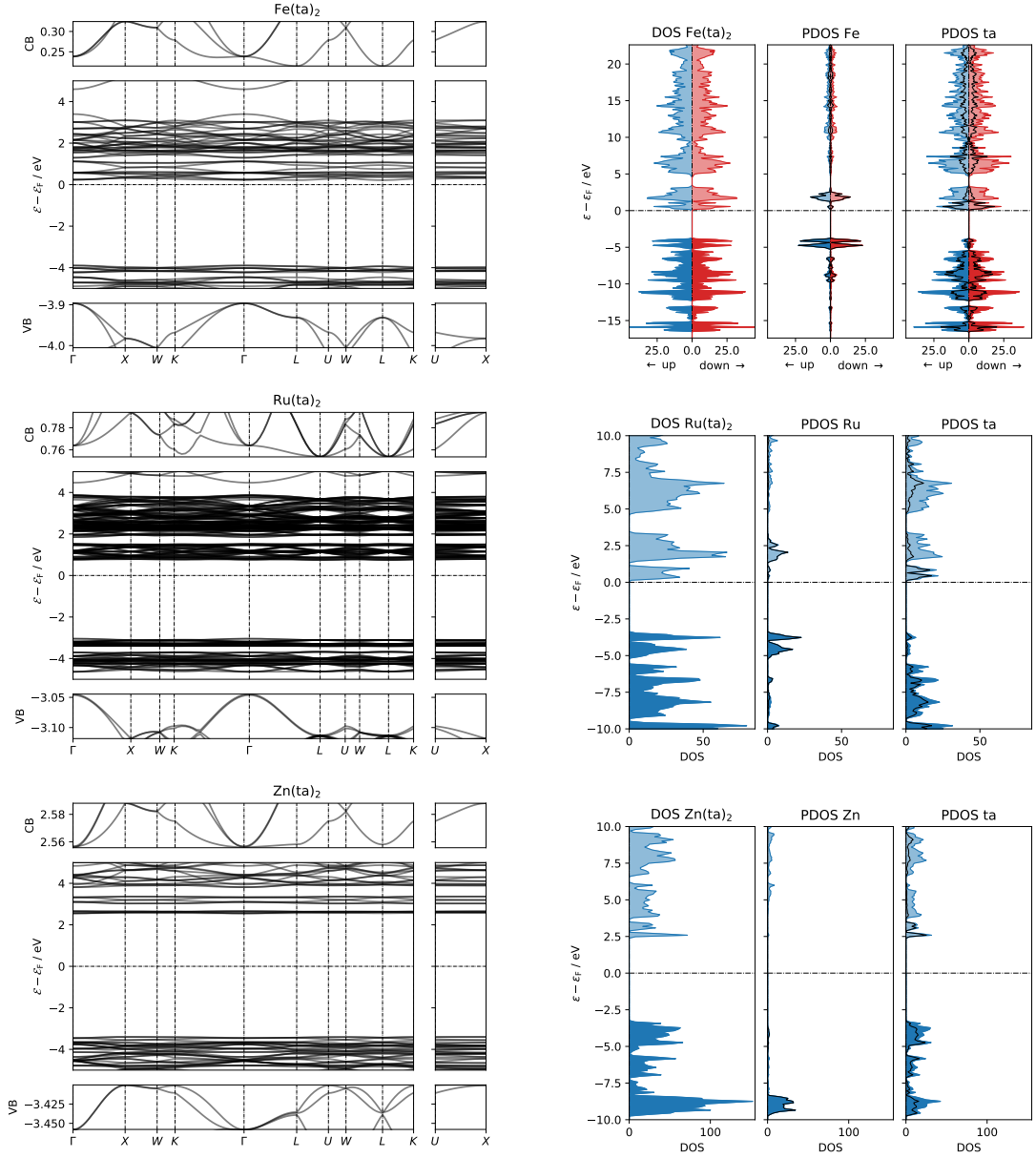


Figure 4.3: Dependence of the total energies for the various strains (index γ) on the magnitude of strain. The curvatures of the depicted parabolas are determined by the elastic constants c_{11} for $\gamma \in \{xx, yy, zz\}$ and to a good approximation (neglecting a term $\mathcal{O}(g^4)$) by c_{44} for the other values of γ . For $\text{Zn}(\text{ta})_2$ the initial relaxation did not relax completely into its local potential energy minimum leading to a slight shift of the parabolae which do, however, not influence the calculations of the curvatures. Reproduced with permission from ref. [1], © 2019 AIP Publishing.

allow for thermal excitation of charge carriers at reasonable temperature. As also theorized by Sun and co-workers,[26] non-vanishing carrier density could be achieved e. g. through doping, which is likely for the cases of $\text{Fe}(\text{ta})_2$ and $\text{Ru}(\text{ta})_2$ considering the position of their Fermi levels slightly below the conduction band edge, with 0.22 eV and 0.75 eV. Therefore, in the following, the conductivity argument is relayed to the mobilities of present charge carriers and the material properties influencing them.

It follows the discussion of all the different parameters and of the mobilities resulting from them. In the beginning, there shall be an overview of all results, followed by a descend to the individual discussions of each descriptor. The parameters and resulting mobilities which are found for the three MOFs are given in Table 4.2. The mobility in the valence band maximum (VBM) and in the conduction band minimum (CBM), that is for holes and electrons, increases from $\text{Zn}(\text{ta})_2$ to $\text{Fe}(\text{ta})_2$ to $\text{Ru}(\text{ta})_2$. While the main reasons for this are the declining effective masses, it is also found that there are non-negligible differences in the crystal stiffnesses and the deformation potential couplings.



(a) Band structures for the various metal(II) 1,2,3-triazolates. Clearly, the principal band gaps are large, with an order of magnitude of several 1 eV, and the width of the edge bands is small, with an order of magnitude of several 1 meV. The trend $Ru > Fe > Zn$ for the band width can be explained by the concept of Lewis acidity and the occupation of the *d* shell, where a Ru atom is a better electron donor than an Fe atom and thus the charge in the Ru-framework is delocalized better, resulting in a higher band width.

(b) Densities of states for the metal(II) 1,2,3-triazolates. The black lines indicate either the partial density of states of the Fe-*d* states or of the N-*p* states. All of them show symmetric spin channel data, as is illustrated for Fe(ta)₂, indicating the low spin configuration of the metal centers. Note, that the valence band edge is given by metal *d*-states and the conduction band edge by the N-*p*-states for the Fe and Ru species. For the Zn species, both band edges are built from N-*p* states, whereas the Zn-*d* states lie further away from the edges.

Figure 4.4: Band structures and densities of states for the various metal(II) 1,2,3-triazolates.

Table 4.1: Band gaps E_g and mean effective masses $\bar{m}_\nu^*(k_o)$ for the various band extrema.

	Fe(ta) ₂	Ru(ta) ₂	Zn(ta) ₂
E_g/eV	4.11	3.71	5.96
$\bar{m}_{\text{vbm}}^*/m_e$	4.45	2.75	9.96
$\bar{m}_{\text{cbm}}^*/m_e$	3.00	1.50	6.27

Table 4.2: Bardeen–Shockley parameters and mobilities.

	νk_o	$\frac{C_o}{\text{eV}\text{\AA}^{-3}}$	$\frac{D_\nu^{\text{BS}}(k_o)}{\text{eV}}$	$\frac{\bar{m}_\nu^*(k_o)}{m_e}$	$\frac{\mu_\nu^{\text{BS}}(k_o)}{\text{cm}^2\text{V}^{-1}\text{s}^{-1}}$
Fe(ta) ₂	vbm	0.18	1.75	4.43	13.77
	cbm		4.04	3.00	6.93
Ru(ta) ₂	vbm	0.17	−1.58	2.75	53.16
	cbm		3.08	1.50	63.66
Zn(ta) ₂	vbm	0.09	1.27	6.27	5.55
	cbm		2.02	9.96	0.69

4.2.1 Carrier effective masses in M(ta)₂

To understand the properties governing the carrier mobilities, at first, the effective masses of the different materials are discussed. As illustrated in Figure 4.5, the CBM of Fe(ta)₂ and Ru(ta)₂ is warped which necessitates a description via an angle-dependent effective mass (sections 2.5.3 and 4.1.3). The conduction band (CB) of Zn(ta)₂ is also warped, however as can be seen in Figure 4.6, the curvature is negligibly small in one* certain direction. For this reason, a meaningful depiction of an energy iso-surface was not possible. The data furthermore shows that the VBM of Fe(ta)₂ and the one of Ru(ta)₂ is almost spherically symmetric. This can also be seen from the range spanned by the values of $m_{\text{vbm}}^*(\Omega)$ (Figure 4.6). For both CBM and VBM the effective masses are lowered by substituting Fe by Ru in the MOF crystal structure. This is not surprising: by the concept of Lewis acidity, Ru atoms should be better electron donors than Fe atoms. This leads to generally more delocalized charges throughout the metal-organic network and thus to greater dispersion, i. e. to higher curvature of the bands and lower effective masses.

4.2.2 M(ta)₂ crystal stiffness

The other evident difference in the parameters shown in Table 4.2 is the bulk modulus of Zn(ta)₂ which is about half as large than for the Fe- or the Ru-MOF, where the latter two have very similar elastic behaviour. The reason for this is the different electronic structure

*The regions of high effective mass correspond to the regions of low curvature per definition. In the Figure, one can see those regions at $(\varphi, \vartheta) = (60^\circ, 30^\circ)$ and $(-120^\circ, -30^\circ)$. This means that these points lie opposite to each other on the sphere.

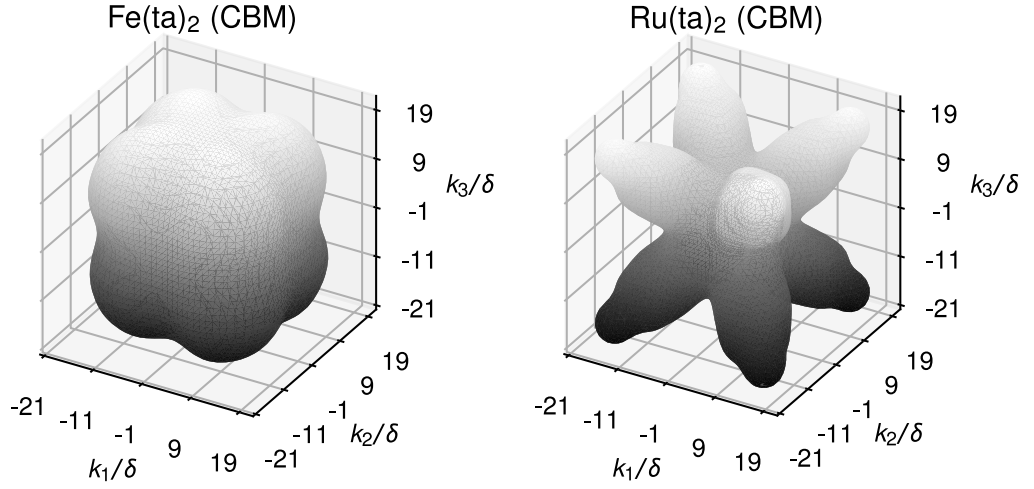


Figure 4.5: Iso-energy surfaces around the CBM. The value for the increment δ was, after interpolation, $\delta = 8 \times 10^{-4} a_0^{-1}$. The energy values for which the surfaces are depicted are 0.85 meV above the CBM of Fe(ta)₂ or Ru(ta)₂. Reproduced with permission from ref. [1], © 2019 AIP Publishing.

Table 4.3: Independent components $c_{\alpha\beta}$ of the elasticity tensors and bulk modulus C_o of Fe(ta)₂ and Ru(ta)₂. All values given in GPa.

	c_{11}	c_{12}	c_{44}	C_o
Fe(ta) ₂	57.2	15.3	33.5	29.3
Ru(ta) ₂	57.7	13.2	30.6	28.0
Zn(ta) ₂	22.7	12.2	9.9	15.7

of the Fe and Ru, and Zn triazolates as shown by the projected density of states (PDOS) of the metal and the linker of the three metal(II) triazolate crystals (Figure 4.4b). Clearly, the valence band (VB) edge of Fe and Ru triazolate is composed mainly of metal- d states, whereas the CB edge is constituted from N- p states. For Zn(ta)₂, the d -block lies lower in energy and both band edges are mainly due to the N- p states.

To set the elastic constants into context: the order of magnitude of the resulting elastic constants (Table 4.3) is comparable to the results given by Ortiz et al., who calculate the elastic constants of several MOFs of the MIL family, and of DMOF-1.[85] This, together with the correct symmetry of the elastic tensor, having all elements expected to be zero below a threshold of at best 1×10^{-3} GPa and at worst 0.1 GPa, increases the confidence in the results.

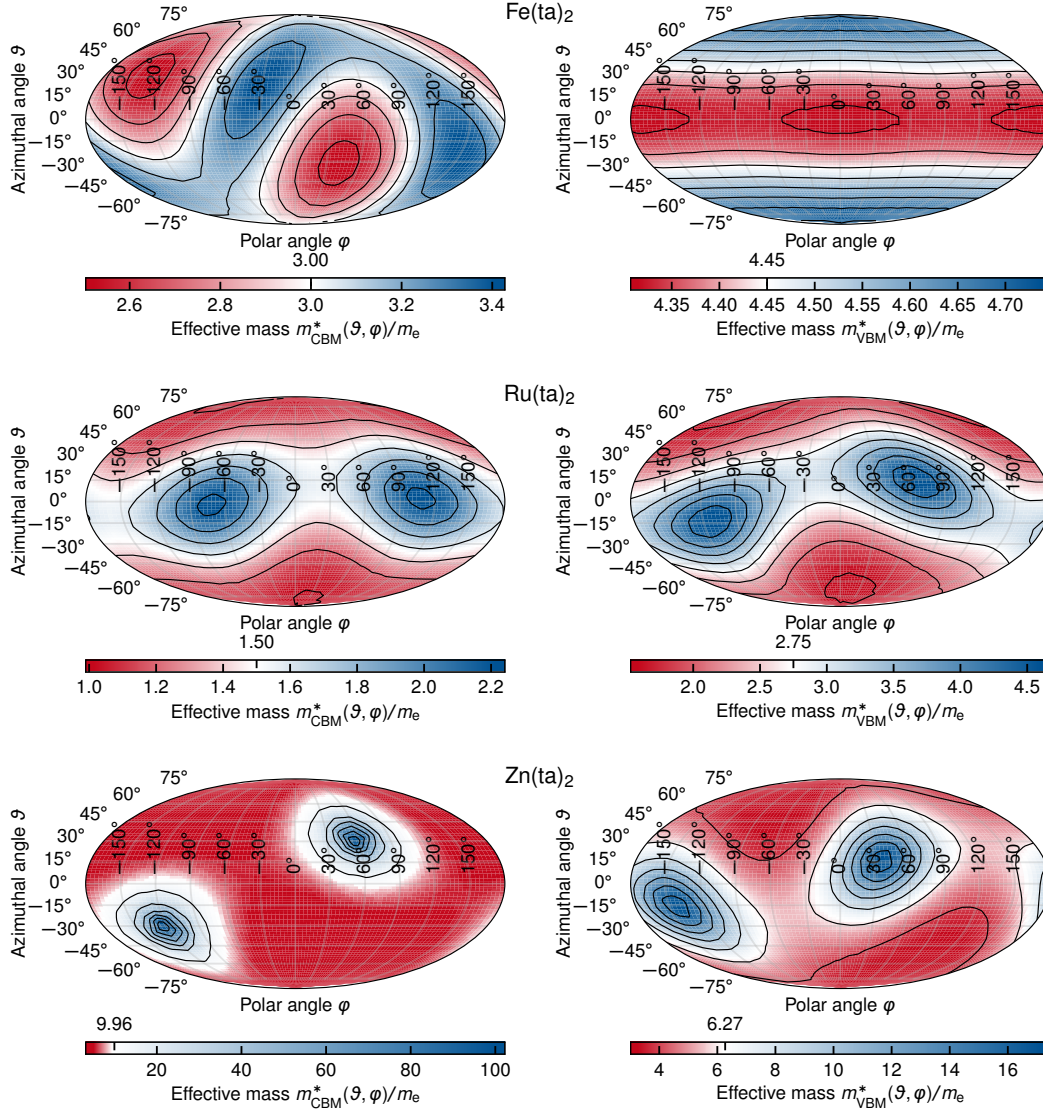


Figure 4.6: Mollweide projection plots of the angular effective masses of $\text{Fe}(\text{ta})_2$, $\text{Ru}(\text{ta})_2$, and $\text{Zn}(\text{ta})_2$. The value marked on the upper side of the color bar is the Lebedev mean $\bar{m}_{\nu k_0}^*$. In this plot, red shades depict low effective masses and thus high mobilities, while blue shaded areas show high masses/low mobilities.

Table 4.4: Components of the deformation potential tensors and the Bardeen–Shockley deformation potential $D_{\nu}^{\text{BS}}(k_{\circ})$. All values given in eV.

	νk_{\circ}	$D_{\nu\alpha}^{\text{ac}}(k_{\circ})$						$D_{\nu}^{\text{BS}}(k_{\circ})$
		1	2	3	4	5	6	
Fe(ta) ₂	vbm	1.75	1.74	1.77		— 0.0 —		1.75
	cbm	4.04	4.04	4.04		— 0.0 —		4.04
Ru(ta) ₂	vbm	-1.42	-1.79	-1.54		— 0.0 —		-1.58
	cbm	3.08	3.07	3.07		— 0.0 —		3.08
Zn(ta) ₂	vbm	1.30	1.24	1.28	0.04	-0.02	0.03	1.27
	cbm	2.02	2.02	2.02		— 0.0 —		2.02

4.2.3 Effective carrier-phonon coupling in M(ta)₂

Finally, the deformation potential constants of the three triazolates are discussed. Note, that whereas the elasticity of a solid and the effective mass of a charge carrier therein, can be interpreted in a rather descriptive way, this is not really true for the deformation potentials which is why they are just summarized in Table 4.4. They describe the response of the microscopic electronic structure of the MOF crystals to a macroscopic deformation or in other words an effective electron-phonon coupling. This may be compared to a simple particle in a box model for which the box size is altered. In both cases, the spacing between the eigenenergies becomes smaller the bigger the box becomes. This effect should also hold true for the band gap, i. e. $\Delta E_{\text{g}} := E_{\text{g}}(u) - E_{\text{g}}(0) < 0$, so that

$$E_{\text{g}}(u) = E_{\text{g}}(0) - \Delta D_{\alpha} u_{\alpha}. \quad (4.18)$$

Thus, it is required that for a dilatation of the crystal $\Delta D_{\alpha} := D_{\text{cbm}\alpha} - D_{\text{vbm}\alpha} > 0$ which is fulfilled for all triazolates investigated.

A summary of all resulting parameters needed to calculate a Bardeen-Shockley mobility together with the resulting mobilities is included in Table 4.2. Furthermore, recognizing the importance of graphical representations to identify potential handles for material optimization,[87] all results are presented graphically in a suitable polar diagram (Figure 4.7). There, the representation is chosen such that the mobilities of CBM or VBM carriers can be determined as a simple sum of their contributions. This highlights the importance of each contribution and e. g. shows that changes in the deformation potential play only a secondary role for the mobility, while differences in MOF elasticities and even more so in the effective masses critically determine μ_{ν}^{BS} . The sign on each axis is chosen in such a way that a semiconductor which is better than another will also occupy an area that appears visually larger in the plot.

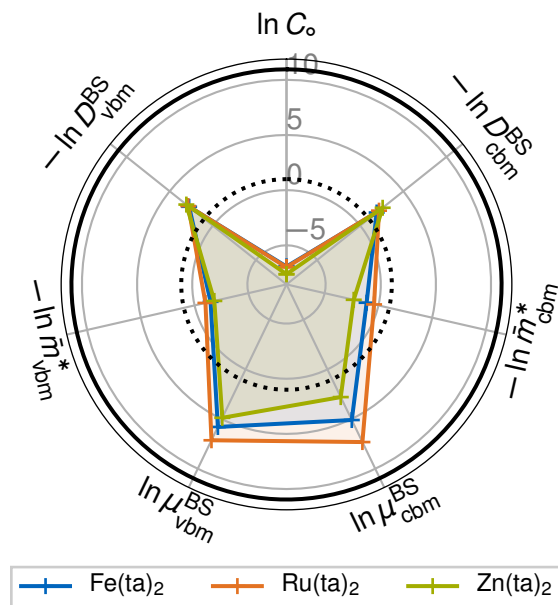


Figure 4.7: Representation of the Bardeen–Shockley parameters and mobilities in a certain polar or spider web plot. All values are given in atomic units and subsequently logarithmized. The black circle gives the value $\ln(\sqrt{8\pi}e\beta^{3/2}/3)$, the argument given in units of $eE_{\text{H}}^{-3/2}$ for a temperature of 300 K. The values for the mobility are also given at this temperature.

Figure 4.7 therefore demonstrates one handle available to the MOF designer in order to optimize charge carrier mobility in a material. Simple exchanges of employed metal ions already lead to large improvements in the carriers effective masses and smaller ones for the MOF’s elasticity, yet they seem to leave the deformation potential, and thus the electron-phonon coupling largely unchanged. Thus, it is a first independent control lever for a more general design paradigm of semi-conductive MOFs.

4.3 Conclusions

Based on (hybrid-) density functional theory, the different properties—such as band gap, carrier effective masses, elasticity, and (acoustic) electron-phonon coupling—of pristine metal organic frameworks contributing to their suitability as semiconductors were studied. Relying on the common Bardeen–Shockley band transport model, at first some of the peculiarities of the soft and porous MOFs studied here are discussed which necessitate more sophisticated approaches than generally applied. It is found, for example, that all of the MOFs studied here, show some form of warped bands, where the band curvature is a more or less complicated function of the reciprocal space angle. The result of this is a failure of the common tensorial description of the effective mass, which nevertheless can be remedied with more sophisticated angle-resolved methods.

Next, the results for three different metal-substituted triazolate MOFs, iron(II), zinc(II), and ruthenium(II) triazolate (Table 4.2) are presented, of which only the first two have been experimentally characterized. All three MOFs show too large band-gaps for non-negligible intrinsic carrier concentrations, which seems to be remedied in experiment through impurities and doping. This leaves the mobility as the major quantity for good conductivity, which is found for the ruthenium compound to be in excess of one of the to date best semi-conducting MOFs, iron triazolate. Both mobilities, though much smaller than e. g. that of silicon-based semiconductors, are with around $10 \text{ cm}^2 \text{ V}^{-1} \text{ s}^{-1}$ at least comparable to modern organic semiconducting materials.[88] We thus propose ruthenium(II) triazolate for future experimental characterization as a potential semi-conducting MOF.

The observed carrier mobilities of ruthenium and iron triazolate place them in a regime, where the applicability of a band transport model is very plausible.[23] Zinc triazolate, on the other hand, we find to have much smaller mobilities of $\lesssim 1 \text{ cm}^2 \text{ V}^{-1} \text{ s}^{-1}$, in accordance with earlier results by Sun and co-workers.[26] There, the accuracy of a band model is certainly debatable, yet experimental trends, at least, do seem to be well reproduced.

Considering the different contributions to the mobility according to the model of Bardeen and Shockley, the carrier effective mass, the MOF’s elasticity, and the acoustic deformation potential (i.e. the electron-phonon coupling), especially the former is found to be most strongly influenced by metal center substitution. Plotting all contributions in a polar graph where the sum over all contributions yields the (logarithmized) mobility one sees that indeed mostly changes in the band dispersion contribute to the observed trends in the mobilities. While the elasticity, and even less so the deformation potential, also do vary, these variations are too small to have a large impact on the carrier mobility. This implies that the choice of metal center, for a fixed MOF topology as a first independent handle for the quantitative design of semiconducting MOF materials in the future.

Yet, the study also shows, that the other contributing factors—that is, elasticity and electron-phonon coupling—so far seem to be under-utilized as a descriptor for MOF design. Given the vast chemical spaces of linkers and metal centers MOF designers can draw from it should certainly be possible to optimize these two parameters as well.

5 Influence of Gas Absorption on the Charge Mobility and its Descriptors in Iron Triazolate

The following chapter reproduces the theoretical studies from a manuscript*, resulting from a collaboration with groups at the University of Augsburg, which is in preparation at the moment.

In general, the conductivity of a material strongly depends on the mobility of its charge carriers—i. e. electrons or electron holes—which basically describes their average velocity on application of an electric field.[23]

One way of describing the mobility is through the Bardeen–Shockley (BS) deformation potential model[24] which has been introduced in section 2.7.3 and applied to pristine metal triazolate crystals in chapter 4, where it was possible to reproduce an experimental trend of conductivity given the premise of a constant charge carrier density.

The detailed discussion of the effects of metal center exchange there, involves three material dependent parameters: the bulk modulus C_o of the crystal, the deformation potential D^{BS} —measuring the electron-phonon coupling, and the mean effective mass \bar{m}^* at the band edge extremum. In the following, the same exposition is used to break down the effect on the charge carrier mobility under gas absorption into the pores of a MOF crystal, where $\text{Fe}(\text{ta})_2$ is used as an example.

However, through the large principal band gaps of pristine metal triazolate crystals[1] and of many other MOFs[26], one still cannot simply argue with the conductivity, as there cannot be any excited and thus mobile charge carriers in this case. Therefore, as in chapter 4, it is assumed that there are in fact mobile charge carriers in the MOF crystal by means of some sort of defect, and furthermore, that this density does not change with pore loading.

This second assumption restricts this study to gases which do not interact strongly with the MOF crystal, i. e. there must not be charge transfer from the absorbed gas particles onto the framework. In the following, the case of $\text{Fe}(\text{ta})_2$ as host crystal and argon, Ar, and carbon dioxide, CO_2 , as guests, i. e. as absorbed species, is studied exemplarily.

*C. Muschielok, A. Reiner, R. Röss-Ohlenroth, A. Kalytta-Mewas, D. Volkmer, A. Wixforth, and H. Oberhofer, (in preparation)

For weakly interacting guests, the ratio of the conductivity of the loaded MOF and the one of the empty MOF is then given by

$$\frac{\sigma(x)}{\sigma(0)} = \frac{qn(x)\mu(x)}{qn(0)\mu(0)} \approx \frac{\mu(x)}{\mu(0)}, \quad (5.1)$$

where n is the density of the mobile charge carriers with charge q . As long as this holds, one can concentrate on mobility arguments, for which again the Bardeen–Shockley expression 2.218 is used.

5.1 Methodology

In the following, among other things, another kind of method of how the bulk modulus and the deformation potential constants are calculated is introduced, which differs from the method used in ref. [1] in that it relies on a simple least squares fit instead of the pseudo-inverse. To avoid redundancy, the mean effective mass is not discussed here. The same method as detailed in chapter 4 is used.

5.1.1 Bulk modulus from hydrostatic deformations

Both the elastic properties (bulk modulus) and the deformation potential of a MOF can be computed from a series of deformations of the material’s unit cell along each of the principal axes[1], as presented in chapter 4. Yet, with a view on computational simplicity and focusing only on the trends induced by pore absorbates, one can use a much simpler procedure relying on hydrostatic expansions of the crystal only. These are expressed through the deformation gradient matrix

$$F^\circ(g) = \left(1 + \frac{g}{3}\right) I, \quad (5.2)$$

with a magnitude g and the 3×3 unit matrix I . Neglecting second-order terms, this deformation gradient leads to the hydrostatic Green–Lagrange strain tensor

$$u^\circ(g) = \frac{1}{2}[(F^\circ)^\top F^\circ - I] = \frac{g}{3}I. \quad (5.3)$$

To compute the bulk modulus, one expands the total energy $E(u^\circ)$ of the MOF in terms of this strain tensor up to second order, arriving at

$$\Delta E(g) = E(g) - E(0) = \frac{1}{2}C_\circ V g^2. \quad (5.4)$$

This means, C_\circ can be obtained by a simple least squares fit. To account for inaccuracies of the optimization, a general second order polynomial is used instead of the origin parabola suggested by 5.4.

5.1.2 First and second order deformation potentials from hydrostatic deformations

An analogous approach can be used for the deformation potentials $D_\nu^{\text{BS}}(k_\circ)$, where ν is the state label—denoting either the VB or the CB—and k_\circ denotes the extremal point of this state’s energy. In this case, the energy levels ϵ_ν at the corresponding band extrema k_\circ , measured with respect to the Fermi energy of the strained unit cell, are expanded in the hydrostatic strain tensor, which yields

$$\begin{aligned}\Delta\epsilon_\nu(k'_\circ, g) &= \epsilon_\nu(k'_\circ, u) - \epsilon_\nu(k_\circ, 0), \\ &= -\frac{1}{3}D_{\nu ii}g = -D_\nu^{\text{BS}}g.\end{aligned}\quad (5.5)$$

Here, k'_\circ denotes the reciprocal space point of the band extremum under strain and k_\circ the one in the relaxed structure. The reference for $\Delta\epsilon_\nu(k'_\circ, g)$ is the relaxed structure, so that $\Delta\epsilon_\nu(k_\circ, 0) = 0$. According to 5.5, the BS deformation potential can thus be obtained from a linear fit of the band edge extremum energy shifts under hydrostatic strain. For a cubic unit cell, where the deformation potential tensor has elements $D_{ij} = D^{\text{BS}}\delta_{ij}$, this means all elements of the full deformation potential tensor are known.

After a preliminary study of the band edge extremum shifts, one realizes, that this formulation has to be extended for MOFs by including a second order coupling K into the description of the band edge extremum shift. Retaining the second order g -terms in the strain tensor, one finds

$$\Delta\delta\epsilon_\nu(k'_\circ, g) = -D_\nu^{\text{BS}}g + \frac{1}{2}\left(K_\nu - \frac{1}{3}D_\nu^{\text{BS}}\right)g^2.\quad (5.6)$$

In general, the coupling constant $K_\nu(k_\circ)$ can be derived from the rank four tensor contraction $K_{\nu iirr}(k_\circ)/9$, similar to the bulk modulus. However, this tensor is not calculated, K_ν merely used as a fitted parameter. Note, that this behaviour can make the use of the pseudo-inverse method from chapter 4 problematic in terms of a systematic error.

5.1.3 Sampling the geometric pore structure of a MOF

In order to allow an unbiased sampling of the arrangement of adsorbates, potentially with a range of different orientations, one first needs to ascertain the geometric structure of the MOF’s pores. To this end, a generalization of the geometric method presented e. g. by Ongari et al.[90] was developed. Note, however, that this generalizes only the criterion by which a point is classified either as part of the pore volume or not. Effectively based on a sphere approximation, the original criterion is only applicable to atomic adsorbates like Ar or small two-atomic molecules like N_2 . The generalization extends the possible adsorbates to linear molecules, e. g. CO_2 , under the assumption of constant bond lengths and angles via a simple rotation of the whole molecule. What is used is what Ongari et al. call the

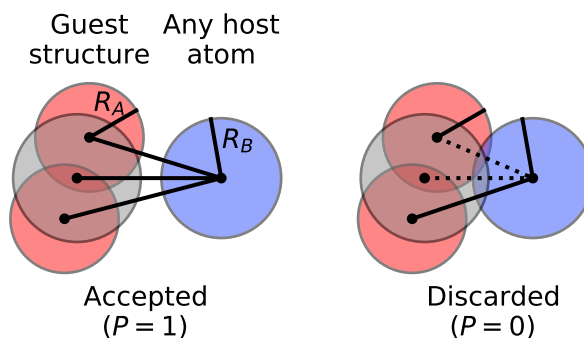


Figure 5.1: Illustration of the Boolean criterion in (5.7). If for any pair of atoms, one from the guest and one from the host structure, the interatomic distance is larger than the sum of their radii (solid lines), the position and rotation of the guest is accepted. If any distance is shorter (broken lines), the position and rotation is discarded.

geometric pore volume[90] as the interest here lies not in obtaining the true value of the void fraction of a MOF crystal. Instead, the points within the pore are good starting positions for DFT optimizations to study the arrangement of adsorbates in the pores, the main focus of this study. For the same reason a comparison with established codes specifically designed to calculate the (geometric) pore volume is omitted. One concentrates on a (periodic) adsorbent structure H and an adsorptive compound G , frequently also called host and guest structures. Here, the symbols H, G are to be understood as sets of the respective nuclear positions of the MOF crystal and the molecule.

In the following, a formal, mathematical introduction of the criterion, by which the volume of the unit cell into one occupied by the MOF and the one which is attributed to the pore, is given. This procedure can briefly be summarized as: first, take G and rotate it by a random rotation. Next, put its center of mass onto a random position within the unit cell of H and check if there is any (hard sphere) overlap with any atom of H . Accept the pair of rotation and position if there is no overlap or discard it if there is. By gathering all possible pairs, one obtains an understanding of the pore in terms of its probabilistic sampling.

Formally this criterion (illustrated in Figure 5.1) can be expressed as the following Boolean function

$$P(\xi = (X, q) | G, H) = \begin{cases} 1 & \text{if } \forall (A, B) \in G \times H : |q\bar{A} + \underline{X} - \underline{B}| > R_A + R_B, \\ 0 & \text{else.} \end{cases} \quad (5.7)$$

Here, A and B are atomic positions in G and H , respectively. X denotes the shift of the center of mass of the guest structure within the host cell. In the following, this is referred to as the shift vector. Thereby, $A, B, X \in [0; 1]^3$ are most conveniently handled in fractional coordinates of the unit cell vectors of H . In order to account for molecular rotations in an

unbiased fashion, $q \in \mathbb{H}_1$ is a unit quaternion (appendix IV). Thus, the tuple $\xi \in [0; 1]^3 \times \mathbb{H}_1$ completely defines position and orientation of an absorbate in space. R_A and R_B , are radii of host and guest atoms, here chosen to be their vdW radii[91].

Based on this rule, one can define a set of points ξ for which the vdW radii of host and guest do not overlap,

$$\mathcal{M}_1(G, H) = \{\xi : P(\xi|G, H) = 1\}. \quad (5.8)$$

Finally, $\mathcal{M}_1(G, H)$ can be projected into Euclidean 3-space

$$\mathcal{V}_1(G, H) = \{X : (X, q) \in \mathcal{M}_1(G, H), q \in \mathbb{H}_1\} \quad (5.9)$$

to yield the accessible static geometric pore of H as seen by G .

For mono-atomic guests, all rotational axes are degenerate and thus one may choose the simpler rule used e. g. by Ongari et al.[90] for P , that is

$$\forall (A, B) \in G \times H : A + X - B > R_A + R_B. \quad (5.10)$$

Note that the meaning of \mathcal{M}_1 and \mathcal{V}_1 is the same in this case.

Without an analytical representation of the MOF's vdW surfaces, the distribution $\mathcal{M}_1(G, H)$ of points in the pore is best sampled in a probabilistic way, where positions and rotations $\xi = (X, q)$ are generated randomly. Note, that the way the positions X are drawn is different from the way the rotations q are drawn. The former are triples taken from a uniform distribution over $[0, 1)$. The latter are quadruples q which are drawn from a standard normal distribution and normalized with respect to their Euclidean norm as described in appendix IV. By this, it is ensured that the translations and rotations are both uniformly distributed.

Consider a spherical guest of radius r . The likelihood of finding a good shift vector is clearly higher the smaller the value of r . This can be utilized to get a presampling of the shift vectors for larger guest structures. That is, one generates a set of shift vectors for a small absorbate which has a high probability of not having an overlap with the MOF and draws the shift vectors for a larger guest structure from this set instead of using the fully random approach.

5.1.4 Higher-order samplings of a pore

One considers the case that a pore can contain more than one guest molecule. This suggests another sampling of the pore volume, now including one representative of the guest species into the host structure. This forms a set $\mathcal{M}_2(G, G, H)$,

$$\mathcal{M}_2(G, G, H) = \{(\xi_1, \xi_2) : \xi_1, \xi_2 \in \mathcal{M}_1(G, H) \wedge P(\xi_2|G, H \cup G_{\xi_1}) = 1\}, \quad (5.11)$$

which is the set of (ξ_1, ξ_2) which individually yield host-guest pairs without overlap and which do not have overlap between the two guest structures. In principle this can be continued iteratively until a maximum number of guests is reached.

5.1.5 Density-Functional Theory

Density-functional theory calculations were performed using the all-electron NAO basis DFT code FHI-aims.[70] The standard “light” basis set of FHI-aims is used. For structural optimizations, the electronic exchange and correlation functional is treated within the GGA choosing the PBE[53] functional. Furthermore, the calculations of the band structure or density of states (DOS) are done using the revised HSE[71, 72] hybrid functional (HSE06) with standard parameters. Additionally, the Tkatchenko–Scheffler (TS) dispersion correction[tkatchenko2009vanderwaals] is employed to effectively account for vdW forces. Structures are relaxed, using the trust-radius method[81] implemented in FHI-aims, using a trust-radius of $10 \text{ meV } \text{\AA}^{-1}$. Bulk moduli are calculated from GGA data, effective masses and deformation potentials from hybrid functional data. The phonon calculations were done using the interface between FHI-aims and Phonopy[92].

5.1.6 Generation of the Absorbate Structures

Starting with the optimized structure[1] of $\text{Fe}(\text{ta})_2$, the pore structures as seen by monohydrogen H, Ar, and CO_2 respectively are sampled using the method described in section 5.1.3. Visualizations of $\mathcal{M}_1(G, \text{Fe}(\text{ta})_2)$ are shown in Figure 5.2 and discussed in more detail in section 5.2.1, below. Note, that while for an H atom guest the static pore takes on the form of a continuous channel network, this changes for the larger guest structures. There, the channels separate into large and small pores, which are sampled as large and small clusters of points in $\mathcal{V}_1(G, H)$. Their central positions are given in Table 5.2. They are labelled according to Figure 5.3.

Selecting these clusters individually, one may easily generate absorbate structures by randomly drawing position-rotation pairs from them. Here, it is assumed, that one of the large or small pores is filled if there is one guest species in it. Note, that this pore—especially if it is a large one—needs not to be completely occupied under this circumstance which suggests a further sampling (section 5.1.4). The absorbate structures are generated with the following procedure:

1. Choose a cluster \mathcal{C} which is not occupied.
2. Randomly draw a $\xi = (X, q)$ from \mathcal{C} .
3. Rotate a guest structure G centered at its center of mass by $q \implies G'$
4. Shift G' by the vector X .
5. Repeat the previous steps until the desired overall pore loading is reached.

Table 5.1: Values for the Bardeen–Shockley parameters of the various absorbate structures.

	C_o	E_g	\bar{m}_{vbm}^*	\bar{m}_{cbm}^*	$D_{\text{vbm}}^{\text{BS}}$	$D_{\text{cbm}}^{\text{BS}}$
	GPa	eV	m_e		eV	
Fe(ta) ₂	34.2	4.11	5.57	2.62	0.63	−0.003
Ar _{1/6} Fe(ta) ₂	34.5	4.07	4.62	2.91	−3.24	−3.96
Ar _{1/3} Fe(ta) ₂	34.6	4.04	4.28	2.79	−2.11	−2.86
Ar _{2/3} Fe(ta) ₂	36.6	4.05	4.03	2.65	−3.65	−4.37
ArFe(ta) ₂	37.1	4.05	6.30	2.07	−9.55	−10.12
(CO ₂) _{1/6} Fe(ta) ₂	32.3	4.11	3.56	3.52	−4.96	−4.79
(CO ₂) _{1/3} Fe(ta) ₂	33.6	4.10	4.86	3.39	−3.03	−3.97
(CO ₂) _{2/3} Fe(ta) ₂	39.6	4.08	5.21	2.50	0.55	0.002
Ar _{1/3} (CO ₂) _{2/3} Fe(ta) ₂	41.2	4.03	4.50	2.37	−7.41	−3.96

6. Then, pre-relax the so-obtained structure under the constraint of a fixed host structure and unit cell. This step may be skipped.
7. Optimize the absorbate structure lifting all constraints.

For the Ar guest, a structure with one atom in a large pore is studied (pore loading of $x = 1/6$ per formula unit of Fe(ta)₂). In the following, this structure is referred to as the low loading (LL) one. Furthermore, the following pore loading configurations (PLCs) are studied: both large pores occupied ($x = 1/3$), the four small pores occupied ($x = 2/3$), and all pores occupied ($x = 1$). The latter PLC is referred to as the high loading (HL) structure. Similar PLCs are generated and studied for CO₂. Finally, a mixed structure with two Ar atoms in the large pores and four CO₂ molecules in the small pores is also considered.

5.2 Results and discussion

5.2.1 Sampling of $\mathcal{M}_1(G, \text{Fe}(\text{ta})_2)$

From the samplings of the host-guest structure pairs one obtains the point distributions shown in Figure 5.2. One finds that for a hydrogen atom (Figure 5.2B) iron triazolate shows a fully connected pore network with nodes at relative positions (0.5, 0.5, 0.5) and (0.75, 0.75, 0.75). For larger absorbate radii, like for an argon atom (Figures 5.2C, 5.3a), the picture looks slightly different. There, two large pores are found with their centers at the node positions found for hydrogen. In between, there are four small pores which already at this simple level of model complexity suggests that argon atoms may move between the pores under only slight deformations of the framework.

Considering polyatomic guest structures like CO₂ (Figure 5.2D), one realises that at each accessible point in the pore the molecule has a more or less strongly preferred

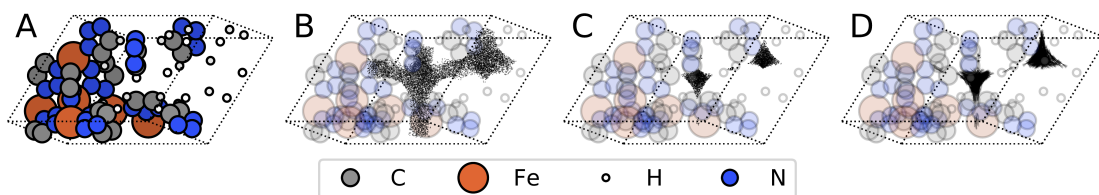
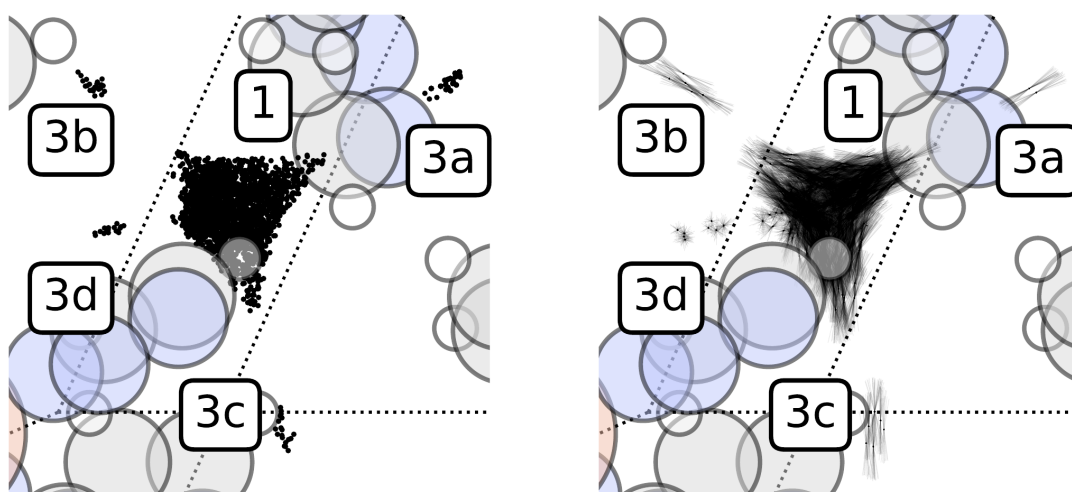


Figure 5.2: Depiction of the $\text{Fe}(\text{ta})_2$ unit cell (A) and the samplings of $\mathcal{V}_1(G, \text{Fe}(\text{ta})_2)$ for different host-guest structure pairs. An H atom would probe the continuous pore structure in B. For an Ar atom, the pore structure looks like the one in C, with two large pores per unit cell and four small pores. In these cases, only the position of guest atom is shown. For the molecular guest CO_2 (D), the distribution of accessible orientations of the molecular axis is shown additionally for each center of mass position.



(a) Zoom into the region around cluster 1 for the sampling of $\mathcal{M}_1(\text{Ar}, \text{Fe}(\text{ta})_2)$.

(b) Zoom into the region around cluster 1 for the sampling of $\mathcal{M}_1(\text{CO}_2, \text{Fe}(\text{ta})_2)$.

Figure 5.3: Identifying the different clusters. In both cases, cluster 2 is not shown as it looks like cluster 1 pointing upwards. It can be seen in Figure 5.2.

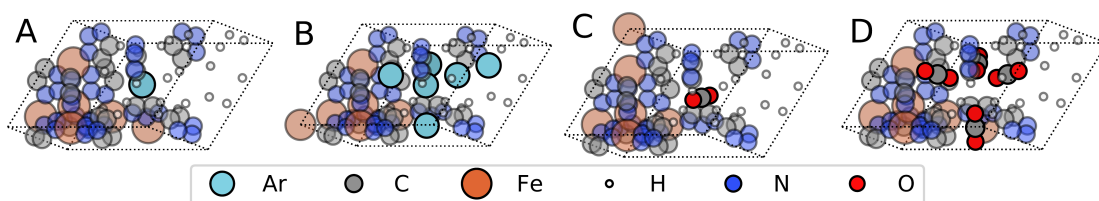


Figure 5.4: Some of the $\text{Fe}(\text{ta})_2$ adsorbate structures investigated in this study: $\text{Ar}_{1/6}\text{Fe}(\text{ta})_2$ (A), $\text{ArFe}(\text{ta})_2$ (B), $(\text{CO}_2)_{1/6}\text{Fe}(\text{ta})_2$ (C), $(\text{CO}_2)_{2/3}\text{Fe}(\text{ta})_2$ (D).

Table 5.2: Positions of the Ar atoms after optimization, starting from the center of mass for each cluster of $\mathcal{M}_1(\text{Ar}, \text{Fe}(\text{ta})_2)$.

Cluster/ Pore	Center of Mass X^a		
	X_1	X_2	X_3
1	0.5	0.5	0.5
2	0.75	0.75	0.75
3a	0.625	0.625	0.625
3b	0.125	0.625	0.625
3c	0.625	0.125	0.625
3d	0.625	0.625	0.125

^a In fractional coordinates.

Table 5.3: Absorption energies per pore for Ar and CO_2 into the large and small pores of $\text{Fe}(\text{ta})_2$. Values given in meV.

	large	small
Ar	-36	33
CO_2	-77	-155

orientation (Figure 5.3b). That is under the assumption of weak interaction with the host or physisorption.

5.2.2 Absorption energies of CO_2 and Ar in $\text{Fe}(\text{ta})_2$

To make the assumption of physisorption for CO_2 and Ar more plausible, in particular for CO_2 , the absorption energies $E_{\text{abs}}(G, \text{Fe}(\text{ta})_2)$ are calculated through

$$E_{\text{abs}}(G, \text{Fe}(\text{ta})_2) = E(G_x \text{Fe}(\text{ta})_2) - [E(\square_x \text{Fe}(\text{ta})_2) + x N_{\text{pores}} E(G)] , \quad (5.12)$$

where $N_{\text{pores}} = 6$ is the number of pores per unit cell in iron triazolate and $\square_x \text{Fe}(\text{ta})_2$ denotes the optimized absorbate structure without the guests.

For $\text{Fe}(\text{ta})_2$ one expects two values for the absorption energy as there are two distinguishable kinds of pores. The resulting values are gathered in Table 5.3. The absorption energies into the large pores were calculated from the $\text{Ar}_{1/3} \text{Fe}(\text{ta})_2$ and the $(\text{CO}_2)_{1/6} \text{Fe}(\text{ta})_2$ absorbates, the values for the small pores from the corresponding $x = 2/3$ absorbate structures. The absorption energies per pore are calculated by dividing the resulting absorption energy by the number of occupied large or small pores. Note, that entropic contributions are neglected here.

To exclude the possibility that the value of the absorption energy for CO_2 absorption into a large pore is underestimated by the positioning of the guest molecule in the pore, a heavily distorted CO_2 molecule, that is a CO_2 molecule in the geometry of a water molecule, was placed at (0.30, 0.30, 0.30) in the vicinity of the iron atom at (0.25, 0.25, 0.25); both fractional coordinates. The distorted geometry was chosen due to considerations regarding the behavior of CO_2 at transition metal carbide surfaces as discussed by Kunkel et al.[93] Then, the geometry was optimized (including the TS dispersion correction), constraining the whole host structure and its unit cell. This resulted in a movement of the distorted molecule

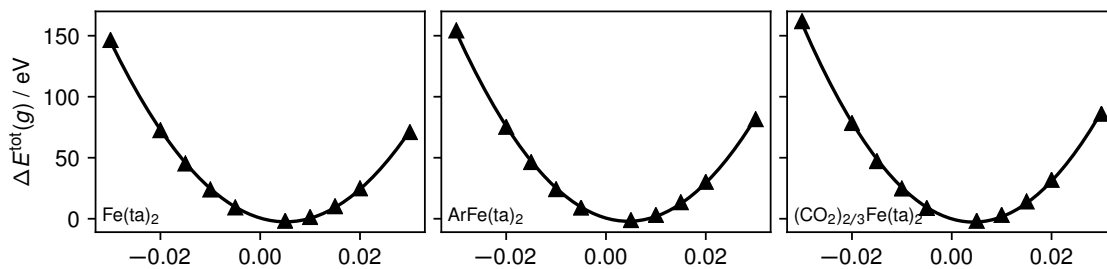


Figure 5.5: Total energies of the strained cell high load absorbate structures.

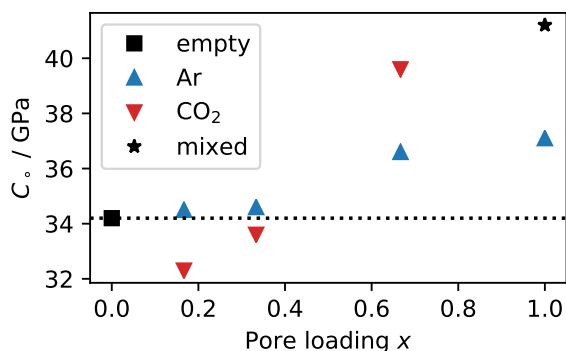


Figure 5.6: Pore loading effects on the bulk modulus.

towards the center of pore 1, accompanied by a stretching of the molecular geometry. The end result was a linear CO_2 molecule in the center of the pore. This behaviour could have been expected, by realizing that the valence of each iron atom is saturated with strongly binding triazolate ligands. It is thus justified, to assume physisorption for Ar and CO_2 when using iron triazolate as host crystal.

5.2.3 Absorbate influence on the elasticity

As exemplarily depicted for $\text{ArFe}(\text{ta})_2$ and $(\text{CO}_2)_{2/3}\text{Fe}(\text{ta})_2$ in Figure 5.7a, the absorption of some species into the MOF pore severely alters the phononic density of states, thus likely influencing the mean scattering rates between charge carriers and phonons which is further discussed in section 5.2.4. The absorption of gas particles into the MOF leads to a change in the mass density of the crystal and will also influence its sound velocity. This in turn must influence the elasticity, like a kind of bracing or rigging for the framework. A similar effect is reported for chemical modifications of the linkers.[94]

From Figure 5.6 and Table 5.1 it is clear, that there is a distinction between the effect due to absorption into the small pores compared to the effect from the large pores. For Ar absorption, the bulk modulus is always increased, where the effect is stronger when the gas atoms are absorbed into the small pores. Conversely, for CO_2 the absorption into the large pores first leads to a slight decrease of the bulk modulus. This should be related to the increase of the lattice constant through absorption of CO_2 into the large pores (Table 5.4).

Table 5.4: Calculated cell constant $a/\text{\AA}$ of the primitive cubic cell for different loadings x and, for convenience, the corresponding cell constant for a conventional cubic cell (scaled by factor of $\sqrt{2}$).

	primitive	conventional
Fe(ta) ₂	11.67	16.50
Ar _{1/6} Fe(ta) ₂	11.66	16.49
Ar _{1/3} Fe(ta) ₂	11.66	16.49
Ar _{2/3} Fe(ta) ₂	11.68	16.52
ArFe(ta) ₂	11.68	16.52
(CO ₂) _{1/6} Fe(ta) ₂	11.75	16.62
(CO ₂) _{1/3} Fe(ta) ₂	11.72	16.57
(CO ₂) _{2/3} Fe(ta) ₂	11.64	16.46

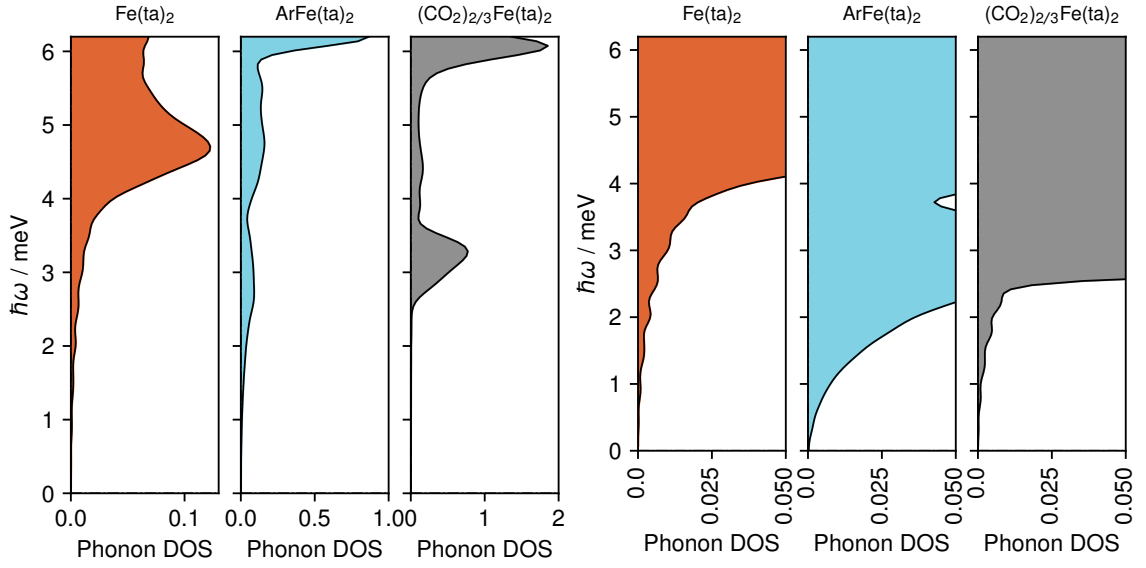
Table 5.5: First and second order deformation potential couplings.

	$D_{\text{vbm}}^{\text{BS}}$	$D_{\text{cbm}}^{\text{BS}}$	K_{cbm}	K_{cbm}
	eV		eV	
Fe(ta) ₂	0.63	-0.003	-10.34	0.06
Ar _{1/6} Fe(ta) ₂	-3.24	-3.96	-3.02	8.31
Ar _{1/3} Fe(ta) ₂	-2.11	-2.86	-34.88	-23.64
Ar _{2/3} Fe(ta) ₂	-3.65	-4.37	-75.20	-63.95
ArFe(ta) ₂	-9.55	-10.12	-54.05	-42.64
(CO ₂) _{1/6} Fe(ta) ₂	-4.96	-4.79	242.25	194.28
(CO ₂) _{1/3} Fe(ta) ₂	-3.03	-3.97	-7.89	2.48
(CO ₂) _{2/3} Fe(ta) ₂	0.55	0.002	-12.47	0.16
Ar _{1/3} (CO ₂) _{2/3} Fe(ta) ₂	-7.41	-3.96	-37.90	-46.81

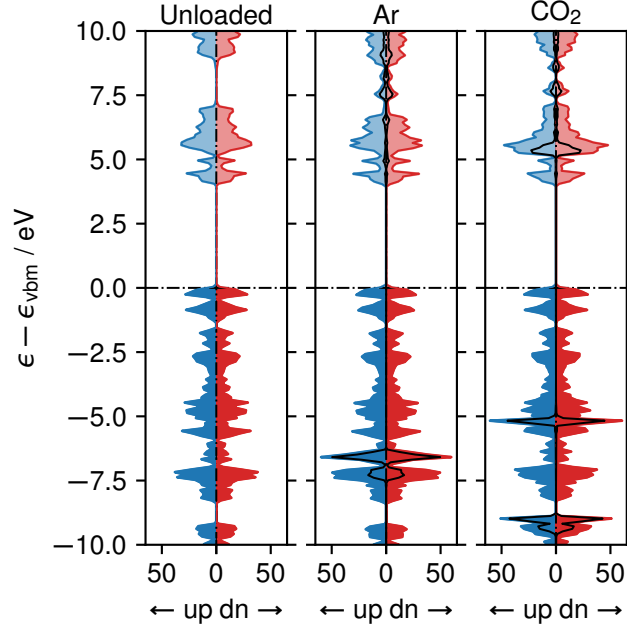
5.2.4 Densities of states and deformation potential

As discussed in chapter 4, the influence of the deformation potential on the BS mobility in a MOF is not the most important factor when the metal center is exchanged. Contrary to this, large changes are induced to the deformation potentials under gas absorption.

Note, that the values for the empty Fe(ta)₂ crystal are not directly comparable to the ones from chapter 4 obtained by using the pseudo-inverse method. This is for two reasons: first, the crystal structures are not comparable, mostly due to smaller cell constants (Table 5.4) which are the consequence of using the TS dispersion correction and second because of the error introduced by the second order deformation potential couplings which is not compensated in the pseudo-inverse method. The latter will be thoroughly discussed in section 6.1.



(a) Phononic densities of states for the unloaded $\text{Fe}(\text{ta})_2$, Ar HL, and CO_2 HL structures. Note the low-energy peak for the Ar HL structure with its tail reaching to zero. One can suspect that this tail in the low energy phonon DOS can lead to easier scattering between the acoustic phonons and the charge carriers by influencing the magnitude of the deformation potential. Also note, that this feature is missing for CO_2 HL, where the deformation potential is similar to the unloaded structure.



(b) Spin channel-resolved DOS for the unloaded $\text{Fe}(\text{ta})_2$ unit cell and the various HL structures. The channels are labelled with up (up) and down (dn). The black line in the plots for the HL structures the projected DOS of the guest atom or molecule respectively. Broadening was used when calculating the DOS. Therefore, the VBM energy of the DOS does not perfectly align with the one obtained from the band structure calculation which was taken as energy reference.

Figure 5.7: Electronic and phononic DOSs for various iron triazolate absorbate structures.

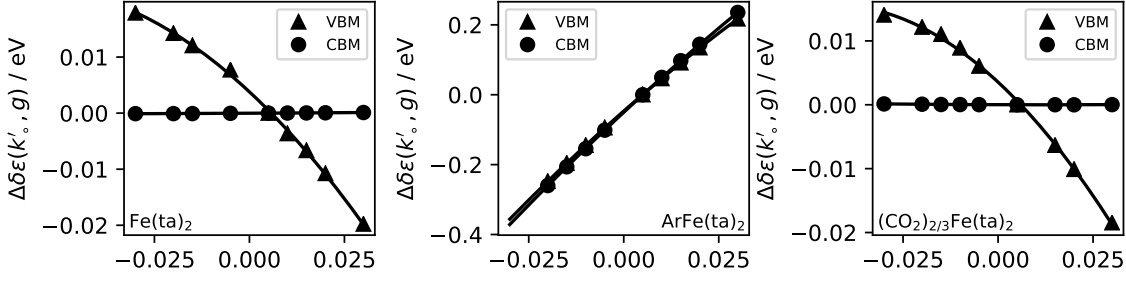


Figure 5.8: Energetic shifts of the band edge extrema for the unloaded and the two HL structures.

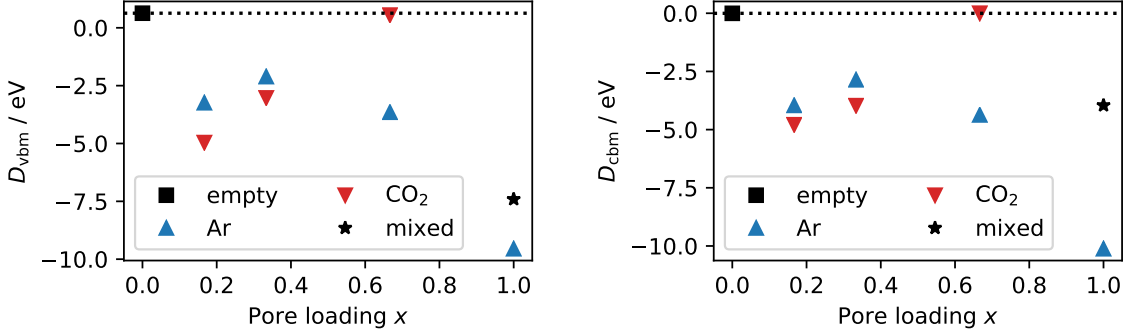


Figure 5.9: Deformation potential coupling for the absorbate structures.

From the electronic DOS plots in Figure 5.7b one can see that the PDOS of Ar or CO₂ lies far from the band edges. From this point of view alone, one could suppose that their influence on the deformation potentials is negligible. In contrast, note, that the phononic DOSs in Figure 5.7a show the significant influence of the Ar guest atoms on the low energy phonons in ArFe(ta)₂. Additionally, the cell constant and thus the volume of the unit cell changes (Table 5.4). This combination of effects leads to a change in the BS deformation potentials, D^{BS} , in the absorbate crystal structures. This change is by almost an order of magnitude with respect to the empty host crystal (Table 5.1) and has thus significant impact on the resulting mobility. A similar effect is predicted for the absorption of CO₂ into the large pores. For absorption into the small pores, however, the deformation potential does not change much compared to the empty MOF crystal. This can be explained by the much sharper onset of state density for CO₂ in the phononic DOS (Figure 5.7a).

Furthermore, it is shown that the second order coupling K_ν can be much larger than the first order deformation potential (Table 5.5). It is related to the so-called Debye–Waller self-energy term, for which at present no *ab initio* analysis is known.[25] Thus, in the following the focus will lie only on the first order (Bardeen–Shockley) deformation potentials.

For the Ar absorbate structures, the changes with respect to the empty Fe(ta)₂ crystal are all comparable in size, only for the structure with all pores filled by one Ar atom, significantly larger deformation potentials result. As a rough trend, the more Ar is absorbed, the larger the absolute value of the deformation potential.

Conversely, for the CO₂ absorbate structures, the trend turns around and one sees smaller

absolute values of the deformation potentials for larger pore loadings. Most interestingly, the values for CO₂ in the small pores are similar in magnitude as the ones for the empty cell.

The latter point can be explained by the alignment of the CO₂ molecules within the small pores and their higher stabilization in the small pores compared to Ar. The forces holding them in position are stronger, so that the scattering of the charge carriers will take place with the phonons of the iron triazolate lattices and not with the ones of the CO₂ sub-lattices.

5.2.5 Effective Masses

After absorption, the mean effective masses of the charge carriers change drastically. The result is that, irrespective of the guest structure, the mean effective mass of the holes, and thus their localization, increases. Conversely, the result for the electrons is a delocalization, that is their effective mass decreases. In both cases, depending on the absorbate, localization and delocalization seem to occur by approximately the same amount. Overall, the range of effective masses is smaller in the loaded cells than in the unloaded cell investigated in this study (Figure 5.10).

Note, that for the unloaded Fe(ta)₂ crystal without TS correction a warped CBM results[1] (Figure 4.5). However, e. g. for any of the absorbate structures and also for the empty structure when the TS correction is used, the warping of the extremum is lifted and one finds ellipsoidal energy isosurfaces in k space. Note furthermore, that all changes reported here should be of purely geometrical origin, as no states of the guest structure seem to mix into the states of the VB or CB edge, which also retain their species and angular momentum character (Figure 5.7b).

5.3 Conclusion and outlook

The hole mobilities which result from the the previously discussed parameters (for the VBM) are always smaller than the mobility which is predicted for the empty MOF crystal. For the electrons in the CB, the resulting mobilities almost vanish, however, this is due to the small value for the CBM deformation potential which is discussed further in chapter 6.

At this point, it is elucidating to imagine a typical experiment in which the voltage between two contacts at the MOF sample is measured for different applied pressures of gas, which is absorbed into the MOF. The current through the sample shall be a constant direct current (DC). Furthermore, the gas and the sample shall have a definite and constant temperature throughout each pressure sweep.

According to (5.1), the change of voltage, which is equivalent to the change in ohmic resistance under the assumption constant current, is equivalent to the (reciprocal) change of the charge carrier mobility. Pressure can be translated to pore loading using e. g. a

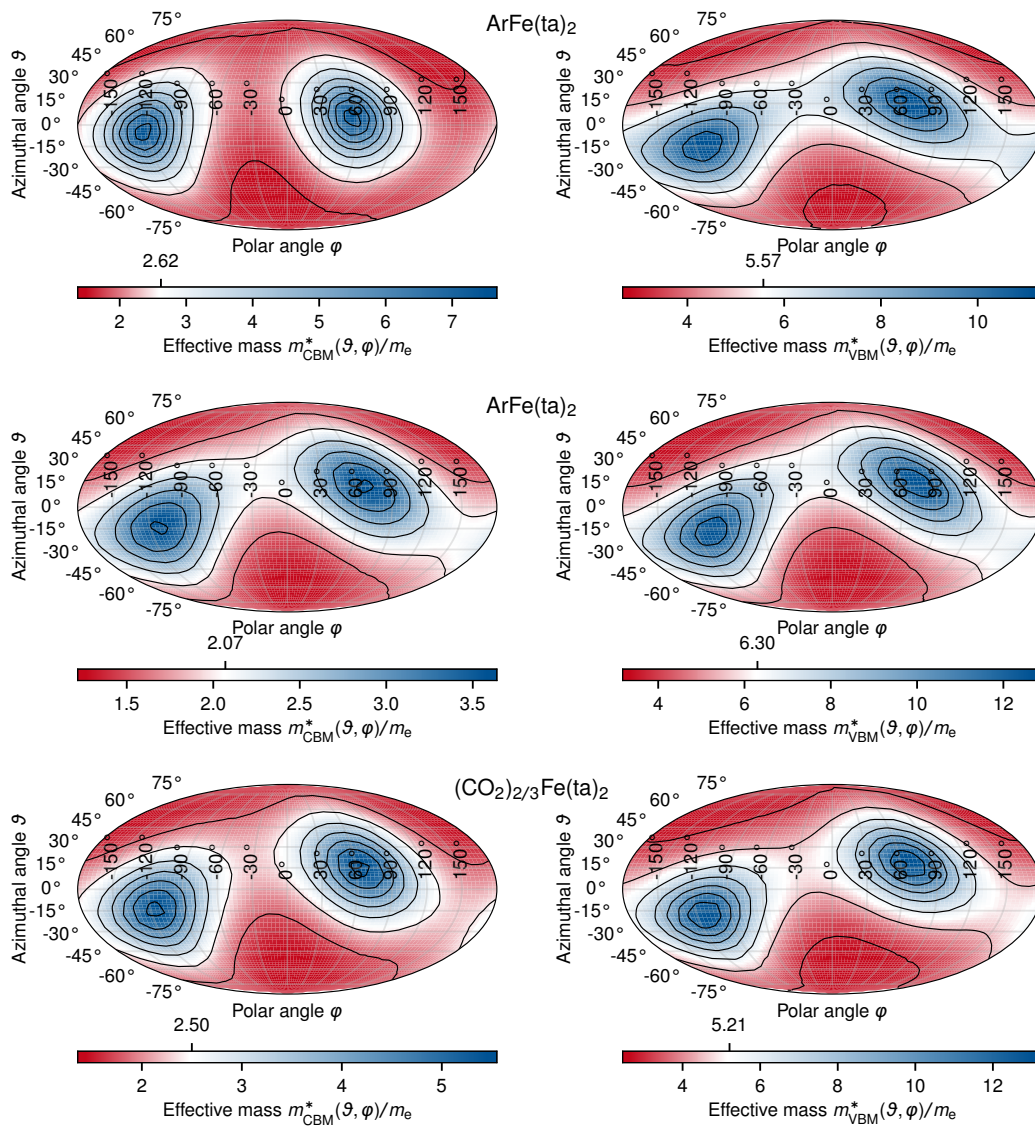


Figure 5.10: Mollweide projection plots[1] for the high load crystal structures and the empty Fe(ta)₂ structure (including the TS correction). The value marked atop of the colorbar is the mean effective mass \bar{m}^* , using Lebedew integration weights, for the VBM (right) or the CBM (left).

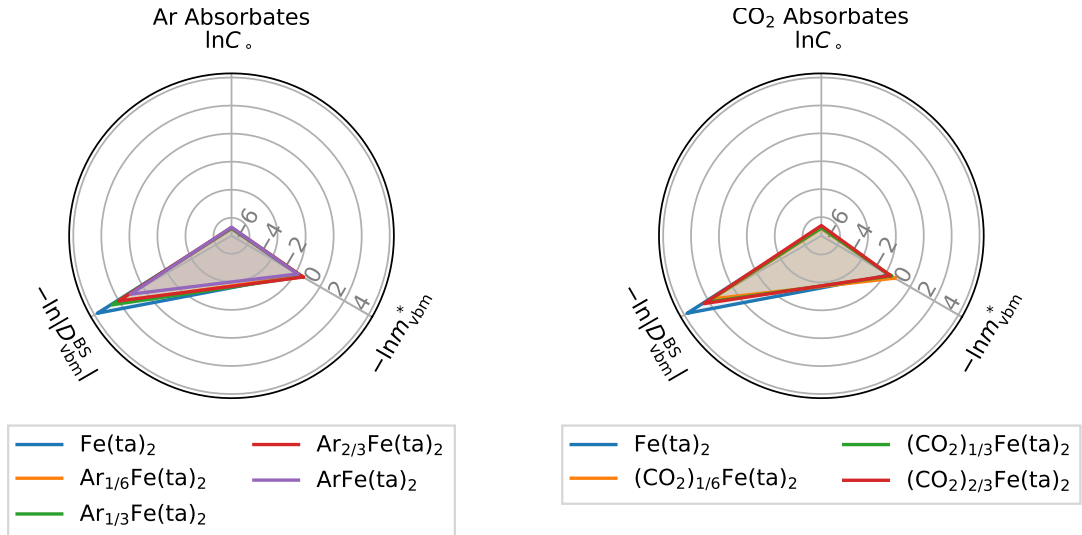


Figure 5.11: Radar plots of the Bardeen–Shockley descriptors for the various absorbate structures. One can clearly see, that the main influence of the guest structures is on the deformation potential. To obtain the logarithmic value of the mobility in AU at 300 K, add all values needed from the graph after weighting them with the power by which they appear in the mobility formula and finally add $\ln(\sqrt{8\pi}\beta^{3/2}/3) \approx 10.95$ (the argument of the logarithm has to be given in $eE_{\text{H}}^{-3/2}$).

Langmuir or Brunauer–Emmet–Teller (BET) isotherm, if the interaction between the gas and the framework is small, i. e. if the gas particles physisorb to the inner surface.

Despite elaborate purification processes after synthesis and again prior to measurement, one has to be assumed that the MOF sample will not be void of absorbents: solvent molecules or other agents left over from synthesis, atmospheric gases etc. Furthermore, it is only possible with great effort to record the voltage change *ab vacuo*. What this means, is that the initial state, taken as reference, which is measured during a pressure sweep, will not resemble the empty MOF crystal, but one with low gas loading. Therefore, when comparing the calculated mobilities with a measured signal, it can be advisable to take a MOF crystal with low gas loading as reference. The lowest loading which is achieved here, is $x = 1/6$, where one absorbent is placed into the pore of a primitive $\text{Fe}(\text{ta})_2$ unit cell. Lower values could be achieved already by using a conventional cell or even some supercell. Also, note that one could have placed the single guest atom or molecule in one of the small pores, which could yield a slightly different value for the reference mobility.

To make up for this ambiguity, a statistical approach is imaginable: a microstate can be defined by a PLC, i. e. a host-guest tuple (H, G_1, \dots, G_N) , which maps to some pore loading x which in turn can be regarded as the corresponding macrostate. The energy which goes with the microstate is its total energy.

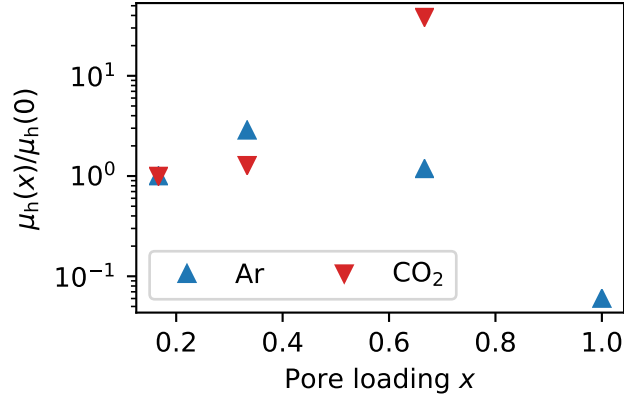


Figure 5.12: Hole mobilities under gas absorption into iron triazolate relative to a single loading of one of the large pores.

The canonical sum over states in this case is given by

$$Z(x) = \sum_{\text{PLC} \rightarrow x} e^{-\beta E(\text{PLC})}, \quad (5.13)$$

which can be used to define a mean mobility $\langle \mu(x) \rangle$ by

$$\langle \mu \rangle = \frac{1}{Z(x)} \sum_{\text{PLC} \rightarrow x} \mu(\text{PLC}) e^{-\beta E(\text{PLC})}. \quad (5.14)$$

This looks simple and elegant, however one must keep in mind, that x entails many PLCs. To get an accurate value for $\langle \mu \rangle$, one may not only use the primitive cell PLCs but has to include supercell PLCs into the description.

Supercell PLCs are not only needed to improve the statistics, but also if one wants to calculate lower values of x than what is dictated by the number of pores in the primitive cell. Overall, the process of determining $\langle \mu \rangle$ is expected to be costly in terms of both, labor and computation time. Therefore, it is necessary to make use of many different simulation techniques, allowing to reduce the costs where possible. For instance, the bulk modulus can be determined using a force field (FF), with the obvious trade-off that one has to fit the FF first to get accurate results. Second, one can use sophisticated tight-binding (TB) techniques to get estimates for the effective masses. So far, the more qualitative way of measuring the charge carrier mobility in units of their mobility in the LL absorbate. This yields the values shown in Figure 5.12 and Table 5.6.

In the following, only the hole mobilities are discussed further, as Sun et al. were able to show that Fe^{3+} defect states lie close to the VB edge and thus holes are suspected to be the mobile charge carriers in iron triazolate.

For Ar absorption, one sees an increase of the mobility for small pore loadings. After a certain pore loading between $x = 1/3$ and $x = 2/3$, the mobility will then decrease again for the high loadings. For CO_2 , no such extremal point seems to exist. There, the mobility

Table 5.6: Mobilities referenced to the values in the LL structure. Note, that the values for Fe(ta)₂ appear twice as the reference is different for Ar and CO₂ absorption. The large values for the electron mobility are due to the small apparent deformation potential for the corresponding (absorbate) structures.

	$\mu_h(x)/\mu_h(x_{\text{ref}})$	$\mu_e(x)/\mu_e(x_{\text{ref}})$
Fe(ta) ₂	28.80	2.24×10^6
Ar _{1/6} Fe(ta) ₂	1.00	1.00
Ar _{1/3} Fe(ta) ₂	2.86	2.14
Ar _{2/3} Fe(ta) ₂	1.18	1.10
ArFe(ta) ₂	0.06	0.39
Fe(ta) ₂	21.37	5.65×10^6
(CO ₂) _{1/6} Fe(ta) ₂	1.00	1.00
(CO ₂) _{1/3} Fe(ta) ₂	1.28	1.66
(CO ₂) _{2/3} Fe(ta) ₂	38.48	16.64×10^6

increases with increasing pore loading. As one can see from Figure 5.12, the change in the mobility seems to be non-linear. The first conclusion of this study is therefore, that the mobility of the charge carriers in an iron triazolate crystal changes for the different pore loadings and that different gases may be distinguished by either the change of mobility, for use in a chemical sensor.

As for the metal center exchange, it is fruitful to study the behavior of the underlying quantities, i. e. the bulk modulus, the effective mass, and the deformation potential. Interestingly, the main influence on the mobility in this case comes from the deformation potential, whereas for the metal center exchange the main changes were for the effective mass and the bulk modulus (Figure 5.11). Note, however, that the changes for the latter two are not small either. The phonon states of the guest atoms and molecules seem to lie much more convenient for the charge carriers considering scattering. This is the second conclusion: through gas absorption one will increase the magnitude of the deformation potential as the guest may open new carrier-phonon scattering channels which are accessible more easily.

6 Pseudo-inverse error cancellation and apparent coupling constants

6.1 Compensating for the quadratic coupling error in the pseudo-inverse method

In chapter 4, the method of choice to calculate the elastic and the deformation potential constants involved the usage of the Moore–Penrose pseudo-inverse of the strain tensor matrix. This gives values for the elastic constants which match the changes in the total energy, as illustrated in Figure 4.3.

However, in chapter 5, it has been shown, that for the deformation potentials one must consider the second order electron phonon couplings in the case of absorbate structures. A cross-check reveals that this behaviour shows also for the empty triazolate crystals. The band edge extremum shifts should be better described by a second order expansion in the elements of the strain tensor:

$$\Delta\delta\epsilon(k'_o, G) = -D_\alpha u_\alpha(G) + \frac{1}{2}K_{\alpha\beta}u_\alpha(G)u_\beta(G). \quad (6.1)$$

In matrix notation this becomes

$$\Delta\delta\epsilon(k_o) = -Du + \frac{1}{2}u^T K u. \quad (6.2)$$

By multiplying with the pseudo-inverse u^+ from the right and solving for the deformation potential,

$$D = -\Delta\delta\epsilon(k_o)u^+ + \frac{1}{2}u^T K, \quad (6.3)$$

one realizes what happens. Clearly, as soon as the second order couplings are not negligible, the usage of the pseudo-inverse inherently introduces an error to the deformation potential constants. In the following, a new method will be introduced by which this systematic error can be compensated by skillful distribution of the strain tensor matrix u and the shift vector $\Delta\delta\epsilon(k_o)$.

The subdivision is done by introducing

$$u_{L\alpha}(\gamma, g) = \begin{cases} u_\alpha(\gamma, g) & \text{if } g < 0, \\ 0 & \text{else} \end{cases}, \quad (6.4)$$

and

$$u_{R\alpha}(\gamma, g) = \begin{cases} u_\alpha(\gamma, g) & \text{if } g > 0, \\ 0 & \text{else,} \end{cases} \quad (6.5)$$

so that

$$u = u_L + u_R. \quad (6.6)$$

By similar means, one subdivides $\Delta\delta\epsilon$. This results in the following two equations, which are coupled by the deformation potential and second order coupling constant matrices D and K :

$$\Delta\delta\epsilon_L u_L^+ = -D + \frac{1}{2} u_L^T K, \quad (6.7a)$$

$$\Delta\delta\epsilon_R u_R^+ = -D + \frac{1}{2} u_R^T K. \quad (6.7b)$$

Addition of these equations yields

$$\Delta\delta\epsilon_L u_L^+ + \Delta\delta\epsilon_R u_R^+ = -2D + \frac{1}{2} (u_L + u_R)^T K. \quad (6.8)$$

Note, that for the definitions of the strain tensors used here, $u_R \approx -u_L$ applies, holds also for the pseudo-inverses. Using it, one finds

$$\Delta\delta\epsilon_L u_L^+ - \Delta\delta\epsilon_R u_R^+ = -2D. \quad (6.9)$$

Through this, the term containing the second order couplings is cancelled. The expression can be solved for D immediately:

$$D = -\frac{1}{2} (\Delta\delta\epsilon_L - \Delta\delta\epsilon_R) u_L^+. \quad (6.10)$$

To compensate for the small errors introduced by the approximation $u_L \approx -u_R$, one can write

$$u_L \approx -u_R \implies 2u_L \approx u_L - u_R \implies u_L \approx \frac{u_L - u_R}{2} =: u_{LR}. \quad (6.11)$$

Table 6.1: Deformation potentials from the pseudo-inverse method without second-order correction (PI) as shown in Table 4.4, with second-order correction (PI+C), and the equivalent values from a simple least squares fit (LS).

	D_{vbm}/eV			D_{cbm}/eV		
	PI	PI+C	LS	PI	PI+C	LS
Fe(ta) ₂	1.752	-1.511	-1.317	4.044	-0.061	-0.063
Ru(ta) ₂	-1.582	-1.252	-1.506	3.073	-0.027	-0.035
Zn(ta) ₂	1.271	0.027	0.000	2.023	0.000	0.000

With this, the expression for D is found to be

$$D = -\frac{1}{2}(\Delta\delta\epsilon_L - \Delta\delta\epsilon_R)u_{LR}^+. \quad (6.12)$$

As shown in Table 6.1, the values obtained with the correction consistently yields values which lie closer to the ones from a least squares fit (Figure 6.1). However, the deformation potentials of Zn(ta)₂ now seem to vanish. This behavior is puzzling at first and will be discussed in the following section.

6.2 Why some deformation potentials seem to be small

Looking at the values in Table 6.1 obtained from the least squares fit for the triazolate structures with different metal centers from chapter 4 or some of the absorbate structures from chapter 5, one realizes that there the deformation potential mostly in the CBM is either very small or even zero. Note especially, that this behavior is seen also in the VBM for a Zn(ta)₂ crystal.

What is common to all these structures is, that the CB edge is built from N- p states, with almost no intermixture of metal states, in particular of metal- d states. This means, that the CB edge in metal triazolate crystals consists almost purely of linker states. For Zn(ta)₂, this is also true for the VB edge. As the deformation potential measures the rate of energy change of the band edges under macroscopic strain of the crystal, one must ask the question what yields this shift microscopically. The answer to this question is a change of the potential of the electronic MB problem due to changes in the crystal structure. A large part of this potential change should come from two-body terms, that means through the changes of bond lengths in the crystal.

Therefore, one analyzes the distances of the nearest neighboring N-atoms around the metal centers M of the triazolate crystal and the distances of the two pairs of vicinal N atoms in each linker. One finds, that the M-N distance changes much stronger under macroscopic strain than the intralinker N-N distance (Figure 6.4).

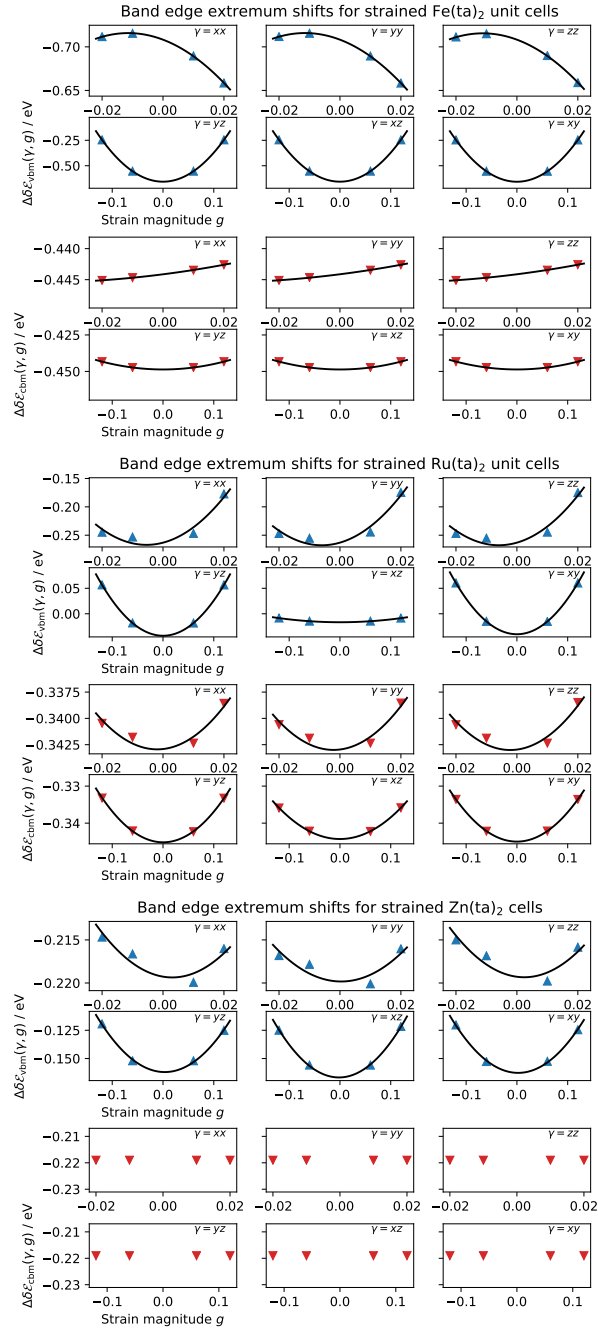


Figure 6.1: Band extremum shifts in the iron, ruthenium, and zinc triazolate crystal. Note, that the quadratic coupling is clearly non-zero, demanding for a correction of the first-order couplings, when using the pseudo-inverse method. Note furthermore, that the linear part of the band extremum shift is small or seem to vanish for the CB.

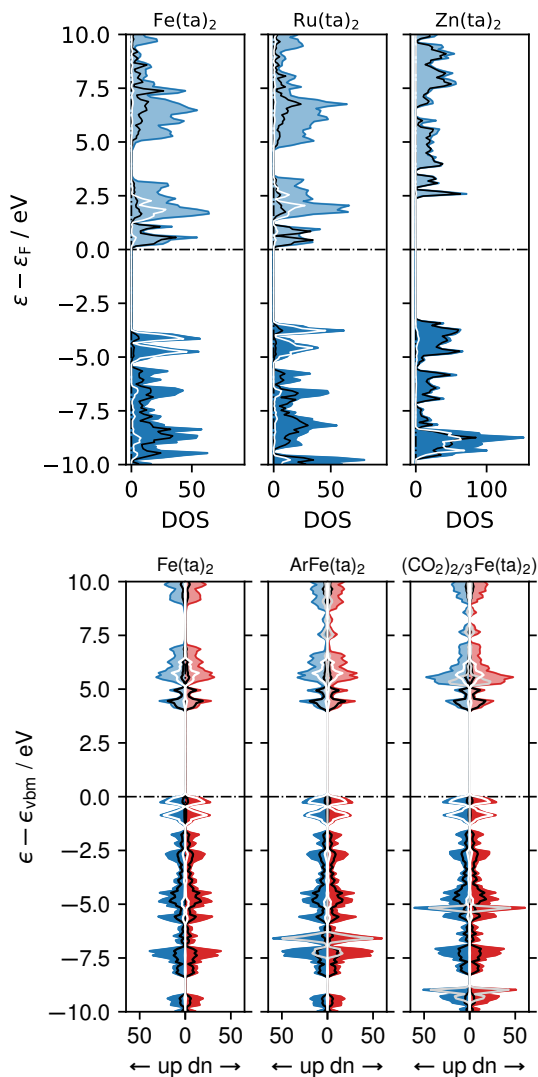


Figure 6.2: DOSs and PDOSs for the metal triazolate crystals from chapter 4 and the iron triazolate absorbates from chapter 5. One can see, that the CB edge consists almost purely of N- p states (black line), whereas the VB edge consists either of metal- d (white line) or also of N- p states ($\text{Zn}(\text{ta})_2$). State density from the absorbate are shown as a gray line.

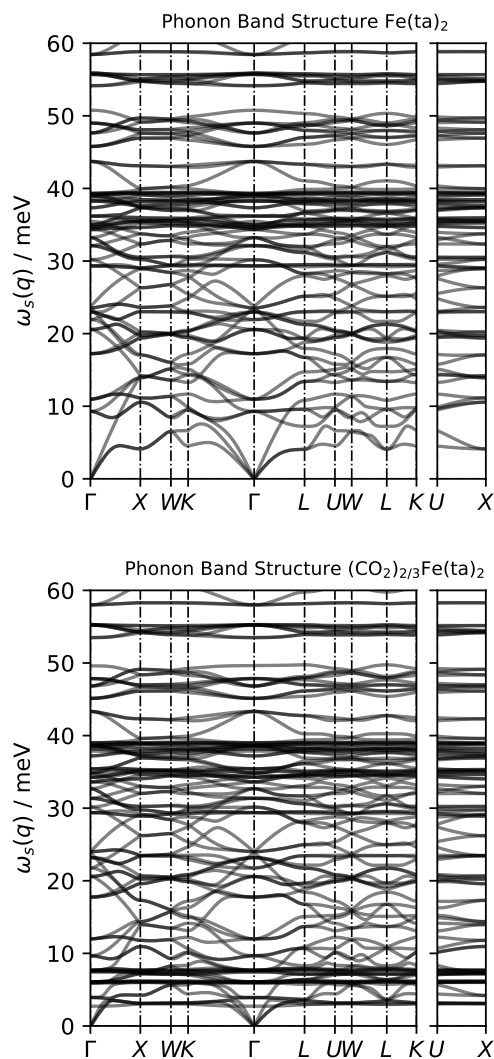


Figure 6.3: Phonon band structures for the iron triazolate crystal and its HL CO_2 absorbate structure. One can clearly see the low energy optical phonons introduced by the guest molecules.

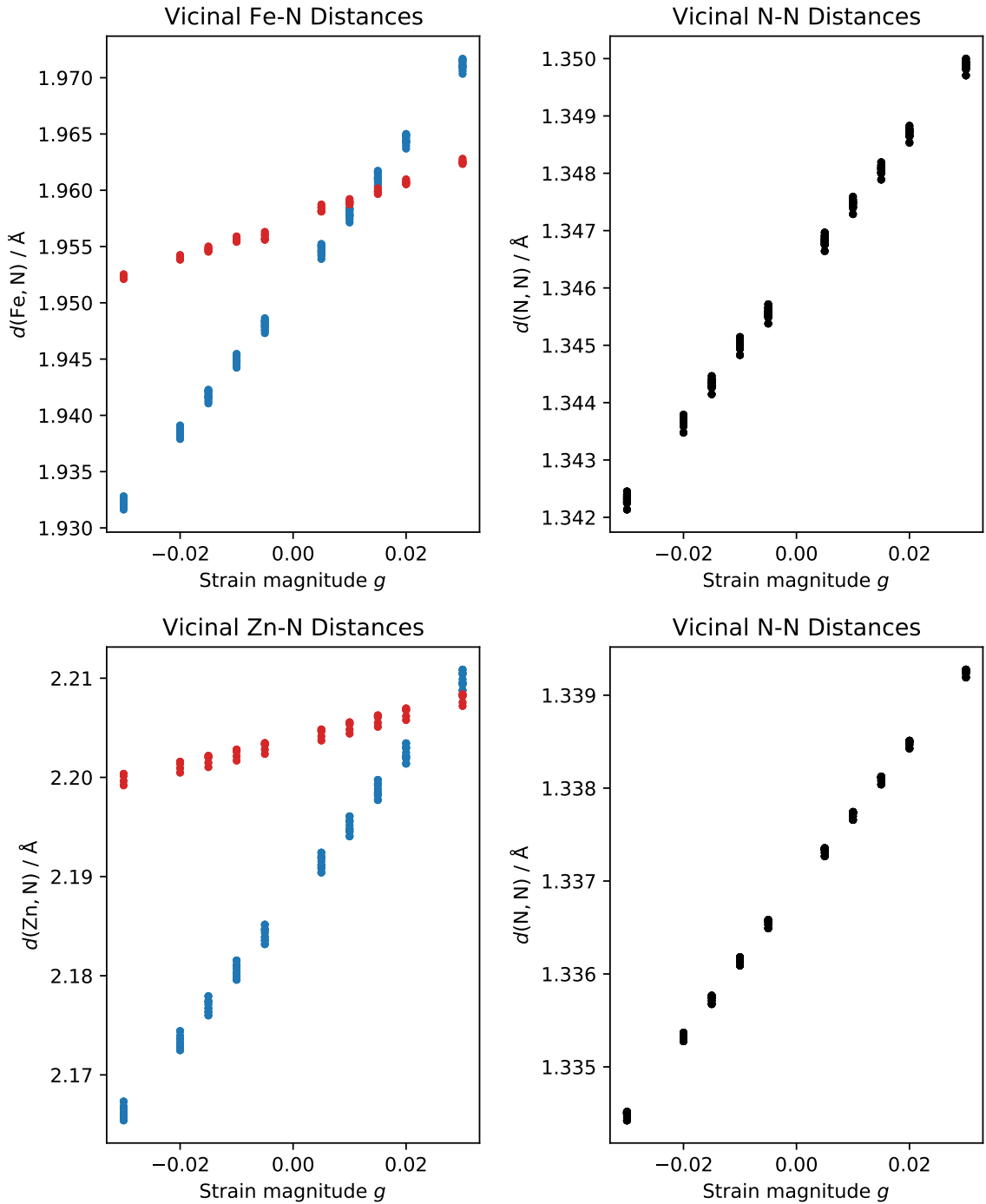


Figure 6.4: Distances between the Fe (top) or Zn (bottom) centers and directly neighboring N atoms, as well as the distances between vicinal N atoms of any linker in the unit cell. One can see that the N octahedra surrounding the metal centers are not ideal but prolate. The degree of compression varies with strain, at some point the prolate octahedra become oblate. Note that the change in the M–N distances is an order of magnitude larger than the one of the N–N distances.

Through this, one realizes that the small deformation potentials which are found by straining the crystal cell must be merely apparent values. One can think of this as an emergent feature of framework materials, which suggests the possibility of coarse-graining the crystal structure into metal centers and linkers and studying only this interaction.

Note, that this is related to the question of why the deformation potentials change under absorption of gas into the MOF crystal, which is discussed in chapter 5.2.4. Basically, this shows the two sides of the coin: one argument aims at the electronic DOS or the electronic band structure of the crystal, the other at the phononic DOS or the phonon band structure. There shouldn't be too large a difference among the different metal triazoles crystals investigated, considering the phononic attributes. Here the electronic DOS argument is more important. On the other hand, roughly the same features as for the empty crystal are observed for the electronic DOS of the Fe(ta)₂ absorbates. Here the low energy phononic DOS and band structure show the differences between the systems. As the deformation potential is a coupling between the charge carriers and the acoustic phonons it has always to be discussed from these two points of view.

6.3 Electron-phonon couplings from phonon displacement patterns—an outlook

Having seen, that the small deformation potentials are only of apparent nature, one must raise the question if there is a better method to calculate their values. This would either involve acoustic phonons of higher momentum or optical phonons*. [23, 46]

By calculating the phonon eigenvectors as described in chapter 2.4.1, for example using the Phonopy[92] package, one can then generate displacement patterns of varying amplitude. By calculating the electronic band structure for each of these displacement patterns, one may then extract an estimate of the coupling of the normal mode to the electronic structure. This could be the shift of certain bands as for the simple deformation potential. If the amplitude of the displacement pattern follows a dimensionless parameter g , then the mode coupling $D_\nu(s, q, k)$ could in this case be something like

$$D_\nu(k; s, q) = \left[\frac{\partial \delta \epsilon_\nu(k; s, q, g)}{\partial g} \right]_{g=0}, \quad (6.13)$$

where $\epsilon_\nu(k; s, q, g)$ means the electronic eigenvalue of band ν at point k for the displacement pattern generated by the mode s at point q with the amplitude according to g .

*The coupling of optical phonons to the charge carriers is not discussed in detail in this thesis. For simplicity, one may assume here a coupling mechanism formally equivalent to the one for the acoustic phonons. The keyword for this is Fröhlich coupling.

A mean coupling would result from a weighting process like

$$D_\nu(k; \beta) = \sum_{sq} f_s(q; \beta) D_\nu(k; s, q), \quad (6.14)$$

where $f_s(q; \beta)$ denotes the Bose–Einstein occupation of the for the phonon state at a temperature specified by β . The expectation is, that the inclusion of optical phonons will decrease the overall mobility, that is, however, under the premise that Matthiesen’s rule holds.

6.4 Conclusion

One realizes, that the macroscopic strain of a MOF crystal involves mostly changes of the distance between the metal centers and adjacent linker atoms. For triazolates these are N atoms. This behaviour can lead to small or even vanishing deformation potentials if a band edge originates from states coming purely from the linker, when strain does only weakly affect the corresponding atom pairs.

This emergent behaviour coming from the framework metastructure can either be circumvented by using more elaborate methods as suggested in section 6.3 or it can be used to better understand the coupling between chage carriers and phonons in MOFs: if to a large extent only properties of the metal-linker bonds are important for the deformation potential, then one can coarse grain the framework structure and study such a model or even descend to a simple model of a mononucleic metal complex.

7 Overall Conclusions

By using the Bardeen–Shockley expression for the charge carrier mobility in a semiconductor, the detailed reasons why MOFs often are bad electronic conductors are studied. The conductivity is thereby determined by two quantities: the mobile charge carrier density and the charge carrier mobility. The former are the electrons which are excited into the conduction band and the holes which remain in the valence band due to this process. This excitation should ideally be by thermal means to overcome a small band gap.

However, for pristine MOF crystals, the electronic band gap is large. Thus, one assumes that in the real material defect states near (one of) the band edges provide enough mobile charge carriers to achieve conductivity. The theoretical model can then deal with the mobility of the charge carriers in a pristine crystal, which nevertheless makes up large portions of the real MOF.

On the other hand, three material properties determine the charge carrier mobility: the effective mass, the bulk modulus, and the deformation potential. The effective mass characterizes the localization of the charge carrier wavepackets, the bulk modulus measures the stiffness of the crystal lattice through which the carriers move and the deformation potential how likely the particles will scatter. In general, the better the mobility the smaller the effective mass and the deformation potential and the larger the bulk modulus.

It has been shown that the substitution of the metal species in a cubic metal(II) triazolate crystal mainly influences the effective mass and the bulk modulus. The reason for this can be seen in the polarizability of the metal atom's electron density and its Lewis acidity which influences the effective mass through charge (de-)localization, on the one hand. On the other hand, the strength of the bonds between the metal centers and the linker N atoms, as well as the connectivity or topology of the network steers the bulk modulus, as indicated by the metal-nitrogen distance changes shown in chapter 6.

By changing the polarizability of the metal centers, one changes the electronic band structure. The phonon band structure stays mostly the same. Thus, the deformation potential does not change much in this case. Its importance is revealed when studying the influence of gas absorption into the pores of a MOF (chapter 5). By this, the phonon band structure changes drastically: low energy modes are introduced through the weakly bonded gas absorbates, leading to a strong increase of the deformation potential. This mechanism can be seen as a moderator for the charge carrier mobility. Note, that gas absorption can also influence the effective mass and the bulk modulus through structural changes of the crystal. However, those are not as dominant as the effects introduced by the deformation potential.

As the linker is only weakly deformed under macroscopic deformation of the MOF unit cell and only the metal-linker distance changes in a discernible way (chapter 6), one way to step towards a better charge carrier mobility in MOFs is to study the metal-linker bonding. Such studies can be done for simple proxy complexes of the metal center and the (saturated) linker. To decrease the effective mass, one would want a strong electronic coupling between the two. For the bulk modulus one would search for bonds with high stiffness. These are two handles by which one can develop future design strategies for MOFs with more mobile charge carriers.

For the deformation potential one can indeed discuss the influence of the electronic and phononic effects separately (chapters 5 and 6), however this dialectic appears artificial. A simple design principle as for the other two principal properties cannot be formulated at present, however it can be assumed that the long wavelength acoustic phonons which at most distort the metal-linker topology play a large role also in determining the deformation potential. Furthermore, the presence of weakly bound adsorbates, can eclipse this effect and increase the deformation potential, thereby decreasing the mobility.

I Highlights of density-functional theory

Exchange-correlation holes

The following synopsis is a standard way to introduce the concept of the XC hole and how it describes the electron-electron interaction in DFT. In the rest of this appendix, no further references are given. The only ones used are the books by Koch and Holthausen[32] and Jensen[31], and the review article by Hättig et al.[95].

The meaning of the XC hole is that for a pair of electrons, the (conditional) probability density of electron 2 being in the direct vicinity of electron 1 is diminished, due to the Coulomb and exchange terms contained in the electron-electron interaction term of the electronic MB Hamiltonian (cf. section 2.1). That is, the XC hole is an effect of the correlated movement of the two particles, caused by the electron-electron interaction \hat{V}^{ee} .

From a statistical point of view, the correlation of the movement of two particles, i. e. electrons in this case, is governed by the following two equations:

$$P_{12}(r_1, r_2) = P_1(r_1)P_2(r_2), \quad (\text{I.1})$$

where P_{12} is the pair probability density and the P_i are the probability densities for the individual particles, as well as

$$P_{12}(r_1|r_2) = \frac{P_{12}(r_1, r_2)}{P_2(r_2)} = P_1(r_1), \quad (\text{I.2})$$

$P_{12}(r_1|r_2)$ being the conditional probability density of electron 1 being at position r_1 if electron 2 is at r_2 . The two particles are statistically uncorrelated, if both equations, (I.1) and (I.2), hold. Otherwise they are said to be statistically correlated.

Given the electron density ρ , cf. (2.7) on p. 7, and the electron pair density ρ_{12} ,

$$\rho(r) = N \int \cdots \int |\Phi(\underline{x})|^2 ds_1 d^4x_2 d^4x_3 \cdots d^4x_N, \quad (\text{I.3})$$

repeating this definition here, for convenience, and

$$\rho_2(r_1, r_2) = N(N-1) \int \cdots \int |\Phi(\underline{x})|^2 ds_1 ds_2 d^4x_3 d^4x_4 \cdots d^4x_N, \quad (\text{I.4})$$

one can write down a relation between those and the corresponding probability densities:

$$P_1(r) = P_2(r) = \frac{1}{N} \rho(r), \quad (\text{I.5})$$

$$P_{12}(r_1, r_2) = \frac{1}{N(N-1)} \rho_2(r_1, r_2). \quad (\text{I.6})$$

Inserting (I.5) and (I.6) into (I.2) yields the condition that the electrons are statistically uncorrelated as

$$\rho_2(r_1, r_2) = \frac{N-1}{N} \rho(r_1) \rho(r_2) = \left[1 + \left(-\frac{1}{N} \right) \right] \rho(r_1) \rho(r_2). \quad (\text{I.7})$$

Going back to the beginning and considering the figurative description of a XC hole, one can define the associated density $\rho^{\text{xc}}(r_1, r_2)$ formally as the deviation of the density of electron 2 under the condition that electron 1 is at r_1 , $\rho(r_2|r_1) = (N-1)P_{12}(r_2|r_1)$ and the density of electron 2,

$$\rho^{\text{xc}}(r_1, r_2) = (N-1)P_{12}(r_2|r_1) - \rho(r_2). \quad (\text{I.8})$$

From this, one can use (I.2) and solve for $\rho_2(r_1, r_2)$,

$$\rho_2(r_1, r_2) = \left(1 + \frac{\rho^{\text{xc}}(r_1, r_2)}{\rho(r_2)} \right) \rho(r_1) \rho(r_2) = (1 + h(r_1, r_2)) \rho(r_1) \rho(r_2), \quad (\text{I.9})$$

where $h(r_1, r_2)$ is a pair correlation density.

As the exchange energy of the electrons is contained entirely within the electron-electron interaction $\langle V^{\text{ee}} \rangle$, one rewrites it in terms of the electron pair density ρ_2 ,

$$\langle V^{\text{ee}} \rangle = \langle \Phi_0 | \widehat{V}^{\text{ee}} | \Phi_0 \rangle = \frac{1}{2} \iint \frac{\rho_2(r_1, r_2)}{r_{12}} d^3 r_1 d^3 r_2. \quad (\text{I.10})$$

Using (I.9), one can dissect this in the usual way into a classical interaction of two uncorrelated electron densities and a non-classical contribution in which the two electron densities interact via the correlation density $h(r_1, r_2)$,

$$\langle V^{\text{ee}} \rangle = \frac{1}{2} \iint \frac{\rho(r_1) \rho(r_2)}{r_{12}} d^3 r_1 d^3 r_2 + \frac{1}{2} \iint \frac{\rho(r_1) h(r_1, r_2) \rho(r_2)}{r_{12}} d^3 r_1 d^3 r_2, \quad (\text{I.11})$$

$$= J[\rho] + \frac{1}{2} \iint \frac{\rho(r_1) h(r_1, r_2) \rho(r_2)}{r_{12}} d^3 r_1 d^3 r_2. \quad (\text{I.12})$$

Writing the integral over the position of electron 2 (including the coefficient of 1/2) as the exchange potential $v^{\text{x}}(r_1)$, one can rewrite this as

$$\langle V^{\text{ee}} \rangle = J[\rho] + \int \rho(r) v^{\text{x}}(r) d^3 r. \quad (\text{I.13})$$

The adiabatic connection formula

In the following, it is motivated why one uses the HF exchange energy as an admixture for the hybrid XC functionals of KS-DFT (cf. section 2.2.2). This account is predominantly influenced by the one given in the book by Jensen[31]. Therefore, no further references are given in this section.

One starts by introducing a modified electronic MB Hamiltonian with a continuous switching parameter λ which turns the electron-electron interaction on ($\lambda = 1$) or off ($\lambda = 0$),

$$\hat{H}^{\text{elec}}(\lambda) = \hat{T}^{\text{el}} + \hat{V}^{\text{eN}}(\lambda) + \lambda \hat{V}^{\text{ee}}. \quad (\text{I.14})$$

This switching is done under the constraint of a fixed electron density ρ , which is achieved by adapting the external potential operator $\hat{V}^{\text{eN}}(\lambda)$. For $\lambda = 1$ this yields the full interaction between electrons and nuclei.

Taking the total energy of this Hamiltonian in the KS picture ($F_\lambda[\rho]$ is the corresponding universal functional),

$$E_\lambda[\rho] = F_\lambda[\rho] + \langle V^{\text{eN}}(\lambda) \rangle, \quad (\text{I.15})$$

one can calculate the XC energy $E_\lambda^{\text{xc}}[\rho]$ from $F_\lambda[\rho]$ by subtracting the kinetic energy of the KS system and the classical Coulomb energy J ,

$$E_\lambda^{\text{xc}}[\rho] = F_\lambda[\rho] - T^{\text{s}}[\rho] - \lambda J[\rho]. \quad (\text{I.16})$$

Subdividing this into the exchange and the correlation energy, one has

$$E_\lambda^{\text{x}}[\rho] = \lambda \left(\langle \Phi_0 | \hat{V}^{\text{ee}} | \Phi_0 \rangle - J[\rho] \right) \quad (\text{I.17})$$

and

$$E_\lambda^{\text{c}}[\rho] = E_\lambda^{\text{xc}}[\rho] - E_\lambda^{\text{x}}[\rho]. \quad (\text{I.18})$$

Using the fundamental theorem of calculus, one has

$$E_\lambda^{\text{xc}}[\rho] = \int_0^\lambda \left[\frac{dE_{\lambda'}^{\text{x}}}{d\lambda'} \right]_{\lambda'} d\lambda' + E_\lambda^{\text{c}}[\rho] \quad (\text{I.19})$$

where the remaining derivative can be obtained using the Hellmann-Feynman theorem. This gives

$$E_\lambda^{\text{xc}}[\rho] = \int_0^\lambda \left\{ \langle \Phi_0(\lambda') | \hat{V}^{\text{ee}} | \Phi_0(\lambda') \rangle - J[\rho] \right\} d\lambda' + E_\lambda^{\text{c}}[\rho]. \quad (\text{I.20})$$

Using (I.13), from the section on the XC hole, one has

$$E_{\lambda}^{\text{xc}}[\rho] = \int \rho(r) \int_0^{\lambda} v_{\lambda'}^{\text{x}}(r) d\lambda' d^3r + E_{\lambda}^{\text{c}}[\rho]. \quad (\text{I.21})$$

The full XC energy is then obtained by setting $\lambda = 1$,

$$E^{\text{xc}}[\rho] = \int \rho \int_0^1 v_{\lambda'}^{\text{x}} d\lambda' d^3r + E^{\text{c}}[\rho]. \quad (\text{I.22})$$

Using the crudest trapezoidal approximation for the λ' -integral gives

$$\int_0^1 v_{\lambda'}^{\text{x}}(r) d\lambda' \approx \frac{1}{2} (v_1^{\text{x}}(r) + v_0^{\text{x}}(r)). \quad (\text{I.23})$$

Finally, substitution of this into (I.22) yields

$$E^{\text{xc}}[\rho] = \frac{1}{2} \int \rho v_1^{\text{x}} d^3r + \frac{1}{2} \langle \Phi_0 | \widehat{V}^{\text{x}} | \Phi_0 \rangle + E^{\text{c}}[\rho]. \quad (\text{I.24})$$

It is noteworthy, that in the $\lambda = 0$ case, there is no electron correlation as there is no electron-electron interaction. This is just described by the KS system with a single determinant. The exchange energy $\langle \Phi_0 | \widehat{V}^{\text{x}} | \Phi_0 \rangle$ is then just the HF exchange energy,

$$E^{\text{xc}}[\rho] = \frac{1}{2} \int \rho v_1^{\text{x}} d^3r + \frac{1}{2} E^{\text{x, HF}} + E^{\text{c}}[\rho]. \quad (\text{I.25})$$

Finally, the admixture of HF exchange energy is generalized as

$$E^{\text{xc}}[\rho] = (1 - \alpha) \int \rho v_1^{\text{x}} d^3r + \alpha E^{\text{x, HF}} + E^{\text{c}}[\rho]. \quad (\text{I.26})$$

II Wannier functions and the equivalent Schrödinger equation

Analogously to the ansatz one makes for the tight-binding approximation, one can define a function $a_n(r)$ for each band n , so that the exact Bloch function is reproduced by the unitary transformation[21]

$$\psi_{kn} = \frac{1}{\sqrt{\mathcal{N}}} \sum_{\underline{m}} e^{ik \cdot L_{\underline{m}}} a_n(r - L_{\underline{m}}). \quad (\text{II.1})$$

The functions a_n are called Wannier functions. If one assumes the Bloch functions ψ_{kn} to be orthogonal, this is also valid for the a_n . Those are furthermore orthogonal with respect to different lattice vectors, so that overall

$$\int a_n^*(r - L_{\underline{m}}) a_{n'}(r - L_{\underline{m}'}) d^3r = \delta_{nn'} \delta_{\underline{m}\underline{m}'}. \quad (\text{II.2})$$

One can easily express the Wannier states in terms of the Bloch states by inverting (II.1):

$$a_n(r - L_{\underline{m}}) = \frac{1}{\sqrt{\mathcal{N}}} \sum_k e^{-ik \cdot L_{\underline{m}}} \psi_{kn}(r). \quad (\text{II.3})$$

Wannier representation of the Schrödinger equation

For studies of the electron dynamics, a time-dependent state $\psi(t, r)$ is constructed as

$$\psi(t, r) = \sum_{n, \underline{m}} f_{n\underline{m}}(t) a_n(r - L_{\underline{m}}), \quad (\text{II.4})$$

where $f_{n\underline{m}}(t)$ are the envelopes of the Wannier functions in the vicinity of the lattice point $L_{\underline{m}}$. [21]

Let H_o be the one-electron Hamiltonian and U some interaction. Then, following Ziman, one rewrites the integral

$$\int a_{n'}^*(r - L_{\underline{m}'}) (H_o + U) \psi(t, r) d^3r = i \int a_{n'}^*(r - L_{\underline{m}'}) \frac{\partial \psi(t, r)}{\partial t} d^3r \quad (\text{II.5})$$

of the SE using (II.4) and (II.3). The first substitution yields

$$\begin{aligned} \sum_{n,\underline{m}} \int a_{n'}^*(r - L_{\underline{m}'}) H_{\circ} a_n(r - L_{\underline{m}}) d^3r f_n(t, L_{\underline{m}}) \\ + \sum_{n,\underline{m}} \underbrace{\langle a_{n'} | t^{\dagger}(L_{\underline{m}'}) U t(L_{\underline{m}}) | a_n \rangle}_{U_{n'n}(L_{\underline{m}'}, L_{\underline{m}})} f_n(t, L_{\underline{m}}) \\ = \sum_{n\bar{m}} \langle a_{n'} | t^{\dagger}(L_{\underline{m}'}) t(L_{\underline{m}}) | a_n \rangle \frac{\partial f_n(t, L_{\underline{m}})}{\partial t}, \quad (\text{II.6}) \end{aligned}$$

where the $t(x)$ are translation operators which shift the argument of the Wannier functions in the position basis by the vector x . Note, that

$$\langle a_{n'} | t^{\dagger}(L_{\underline{m}'}) t(L_{\underline{m}}) | a_n \rangle = \delta_{n'n} \delta_{\underline{m}'\underline{m}}. \quad (\text{II.7})$$

Then, expanding the Wannier state $a_n(r - L_{\underline{m}})$ in (II.6) in terms of Bloch states, gives

$$\begin{aligned} \sum_{n,\underline{m}} \langle a_{n'} | t^{\dagger}(L_{\underline{m}'}) \frac{1}{\mathcal{N}} \sum_k e^{-ik \cdot L_{\underline{m}}} \epsilon_n(k) | \psi_{n,k} \rangle f_n(L_{\underline{m}}) \\ + \sum_{n\bar{m}} U_{n'n}(L'_{\underline{m}}, L_{\underline{m}}) f_n(t, L_{\underline{m}}) \\ = i \frac{\partial f_{n'}(t, L_{\underline{m}'})}{\partial t}. \quad (\text{II.8}) \end{aligned}$$

Using (II.1) to reexpress the Bloch states again through Wannier states and defining

$$\epsilon_{n,\underline{m}} = \frac{1}{\mathcal{N}} \sum_k e^{-ik \cdot L_{\underline{m}}} \epsilon_n(k) \quad (\text{II.9})$$

yields

$$\begin{aligned} \sum_{n,\underline{m},\underline{m}''} \epsilon_{n,\underline{m}-\underline{m}''} \langle a_{n'} | t^{\dagger}(L_{\underline{m}'}) t(L''_{\underline{m}}) | a_n \rangle f_n(L_{\underline{m}}) \\ + \sum_{n\bar{m}} U_{n'n}(L'_{\underline{m}}, L_{\underline{m}}) f_n(t, L_{\underline{m}}) \\ = i \frac{\partial f_{n'}(t, L_{\underline{m}'})}{\partial t}. \quad (\text{II.10}) \end{aligned}$$

Finally, one has the result

$$\sum_{\underline{m}} \epsilon_{n',\underline{m}-\underline{m}'} f_{n'}(L_{\underline{m}}) + \sum_{n\bar{m}} U_{n'n}(L'_{\underline{m}}, L_{\underline{m}}) f_n(t, L_{\underline{m}}) = i \frac{\partial f_{n'}(t, L_{\underline{m}'})}{\partial t}. \quad (\text{II.11})$$

Using, that the operator $\epsilon_n(-i\nabla)$, which is obtained by taking the expression for the

one-electron energy and substituting the crystal momentum by an effective momentum operator $-i\nabla$, acting upon a function $f(r)$ gives

$$\epsilon_n(-i\nabla)f(r) = \sum_{\underline{m}} \epsilon_{n,\underline{m}}f(r + L_{\underline{m}}), \quad (\text{II.12})$$

and inverting this expression, gives the reformulated SE

$$\left[\epsilon_n(-i\nabla) - i\frac{\partial}{\partial t} \right] f_n(t, r) + \sum_{\underline{nm}} U_{n'n}(L'_{\underline{m}}, L_{\underline{m}})f_n(t, L_{\underline{m}}) = 0. \quad (\text{II.13})$$

The envelope $f_n(t, r)$ acts now as an effective wavefunction defined throughout the crystal and not only at the lattice points. The operator $\epsilon_n(-i\nabla)$ is called the equivalent Hamiltonian, with respect to H_o .

III Notes on strain tensors and elasticity

Differences introduced through the deformation gradient

In ref. [84] by de Jong et al., the Green–Lagrange strain tensors $u(\gamma, g)$ are given by

$$u(\gamma, g) = \frac{1}{2} [(F^\gamma(g))^T F^\gamma(g) - I] , \quad (\text{III.1})$$

where I is the unit matrix and $F^\gamma(g)$ a deformation gradient matrix,

$$F^\gamma(g) = I + g\Lambda^\gamma . \quad (\text{III.2})$$

The matrix $\Lambda^\gamma = \Lambda^{ab}$ is defined to be $\hat{e}_a \otimes \hat{e}_b$ in ref. [84]. When the symmetrized version of the Λ -matrices is used (section 4.1.4), one has

$$\Lambda_J^\gamma = \hat{e}_a \otimes \hat{e}_b , \quad (\text{III.3})$$

$$\Lambda_S^\gamma = \hat{e}_a \otimes \hat{e}_b + \hat{e}_b \otimes \hat{e}_a = 2(\Lambda_J^\gamma)_{\text{sym}} , \quad (\text{III.4})$$

where sym denotes symmetrization. Inserted into the strain tensor yields

$$u_X(\gamma, g) = g(\Lambda_X^\gamma)_{\text{sym}} + \frac{1}{2}g^2(\Lambda_X^\gamma)^T \Lambda_X^\gamma . \quad (\text{III.5})$$

It shall be emphasized, that this form is still independent on the exact form of the Λ matrix used. Explicitly, for the form used by de Jong et al., one finds

$$u_J(\gamma, g) = g(\Lambda_J^{ab})_{\text{sym}} + \frac{1}{2}g^2 \Lambda_J^{bb} . \quad (\text{III.6})$$

In contrast, for the symmetrized matrix one finds in the end

$$u_S(\gamma, g) = 2 \left(g + \frac{1}{2}g^2 \delta_{ab} \right) (\Lambda_J^{ab})_{\text{sym}} + \frac{1}{2}g^2 (\Lambda_J^{aa} + \Lambda_J^{bb}) . \quad (\text{III.7})$$

For $\gamma < 3$, these expressions yield

$$u_J(aa, g) = \left(g + \frac{1}{2}g^2 \right) \Lambda_J^{aa} =: g_{\text{eff},J} \Lambda_J^{aa} , \quad (\text{III.8})$$

and

$$u_S(aa, g) = 2 \left(g_{\text{eff},J} + \frac{1}{2}g^2 \right) \Lambda_J^{aa} = g_{\text{eff},S} \Lambda_J^{aa}. \quad (\text{III.9})$$

For the values of g which are used in practice, it is possible to neglect the $O(g^2)$ terms. Then, the expressions simplify to

$$u_J(\gamma, g) = g \Lambda_J^{ab}, \quad (\text{III.10})$$

and

$$u_S(\gamma, g) = 2g \Lambda_J^{ab}. \quad (\text{III.11})$$

The gist of this is, that when using the symmetrized Λ matrices, the magnitude of the strain is effectively doubly as large as if one uses the original matrices of de Jong et al..

Total energy changes in cubic crystals

For any crystal one can write down Hooke's law

$$\Delta E(u) = \frac{1}{2} V_{UC} c_{\alpha\beta} u_\alpha u_\beta. \quad (\text{III.12})$$

Explicitly, for a cubic crystal, this gives

$$\Delta E(u) = \frac{1}{2} V_{UC} [c_{11}(u_1^2 + u_2^2 + u_3^2) + 2c_{12}(u_1u_2 + u_2u_3 + u_1u_3) + c_{44}(u_4^2 + u_5^2 + u_6^2)]. \quad (\text{III.13})$$

Together with the explicit expressions (III.10), one has

$$\Delta E(aa, g) = \frac{1}{2} V_{UC} c_{11} g^2, \quad (\text{III.14})$$

$$\Delta E(ab, g) = \frac{1}{2} V_{UC} \left(\frac{1}{2} c_{11} g^4 + c_{44} g^2 \right) \approx \frac{1}{2} V_{UC} c_{44} g^2. \quad (\text{III.15})$$

If one uses the symmetrized Λ matrices, one has to substitute the value of g in these equations by $2g$.

IV Introduction to quaternions

It is very convenient to express rotations of molecular absorptates in terms of unit quaternions. In the following a brief review of the theoretical background relevant for this work is given.

Consider Euclidean 4-space \mathbb{R}^4 with elements $q = (q_0, q_1, q_2, q_3)$. One introduces three so-called hypercomplex elements[96] i , j , and k , so one can write

$$q = q_0 + q_1i + q_2j + q_3k. \quad (\text{IV.1})$$

Using the Hamiltonian rules of multiplication,[96]

$$i^2 = j^2 = k^2 = -1, \quad (\text{IV.2})$$

$$ij = k = -ji, \quad (\text{IV.3})$$

$$jk = i = -kj, \quad (\text{IV.4})$$

$$ki = j = -ik, \quad (\text{IV.5})$$

one can define a non-commutative multiplication $a \cdot b$ of two quaternions which is still associative.[96] The multiplication dot will be left away if not needed for clarity. For each quaternion $q \neq 0$ there exists a multiplicative inverse $q^{-1} = \bar{q}/\|q\|_2^2$, where $\bar{q} = q_0 - q_1i - q_2j - q_3k$ is the conjugate quaternion to q and $\|q\|_2$ is the Euclidean 2-norm of q . Note, that for unit quaternions this inverse is just the conjugate. Finally, the Euclidean vector space $(\mathbb{R}^4, +)$ together with quaternion multiplication constitutes a division ring or *Schiefkörper* \mathbb{H} .

In the following, the set of unit quaternions is denoted by $\mathbb{H}_1 = \{q \in \mathbb{H} : \|q\|_2 = 1\}$ and the set of the so-called pure quaternions by $\mathbb{H}_0 = \{q \in \mathbb{H} : q_0 = 0\}$. For pure quaternions, the notation \underline{q} is used. With this, a general quaternion may be written as

$$q = q_0 + \underline{q}. \quad (\text{IV.6})$$

Note, that a point and thus any vector X in 3-space can be regarded as a pure quaternion $\underline{X} = (0, X_1, X_2, X_3) = (0, X) \in \mathbb{H}_0$. With this notation, a rotation $X' = R(a, \theta)X$ of a point X around an axis a by an angle θ can then be expressed by the multiplication[96]

$$\underline{X}' = q_{a,\theta} \underline{X} \bar{q}_{a,\theta}, \quad (\text{IV.7})$$

where the unit quaternion $q_{a,\theta}$ is easily defined in terms of the axis and the angle as[96]

$$q_{a,\theta} = \cos\left(\frac{\theta}{2}\right) + \sin\left(\frac{\theta}{2}\right) \underline{a}. \quad (\text{IV.8})$$

One can generate a random uniform distribution of points on a d -sphere S^d by drawing each coordinate from a standard normal distribution which is inherently rotationally invariant and normalizing the resulting vector.[97] For the unit 4-sphere this means, that one can generate a set of random points q which can be interpreted as a set of unit quaternions. As each q can be interpreted as a three-dimensional rotation, this is a way to uniformly sample rotations.

Bibliography

- [1] C. Muschiellok and H. Oberhofer, *J. Chem. Phys.* **151**, 015102 (2019) (cit. on pp. iii, 22, 26, 45, 52, 53, 56, 61, 62, 66, 74, 75).
- [2] M. P. Suh, H. J. Park, T. K. Prasad, and D.-W. Lim, *Chemical Reviews* **112**, PMID: 22191516, 782 (2012) (cit. on p. 1).
- [3] H. Wu, Q. Gong, D. H. Olson, and J. Li, *Chemical Reviews* **112**, PMID: 22257090, 836 (2012) (cit. on p. 1).
- [4] K. Sumida, D. L. Rogow, J. A. Mason, T. M. McDonald, E. D. Bloch, Z. R. Herm, T.-H. Bae, and J. R. Long, *Chemical Reviews* **112**, PMID: 22204561, 724 (2012) (cit. on p. 1).
- [5] S. R. Batten, N. R. Champness, X.-M. Chen, J. Garcia-Martinez, S. Kitagawa, L. Öhrström, M. O’Keeffe, M. P. Suh, and J. Reedijk, *Pure and Applied Chemistry* **85**, 1715 (2013) (cit. on pp. 1, 41).
- [6] H. Furukawa, K. E. Cordova, M. O’Keeffe, and O. M. Yaghi, *Science* **341** (2013) (cit. on pp. 1, 41).
- [7] D. D. Medina, A. Mähringer, and T. Bein, *Isr. J. Chem.* **58**, 1 (2018) (cit. on p. 1).
- [8] C. Janiak, *Angew. Chem. Int. Ed. Engl.* **36**, 1431 (1997) (cit. on pp. 1, 41).
- [9] P. Ramaswamy, N. E. Wong, and G. K. H. Shimizu, *Chem. Soc. Rev.* **43**, 5913 (2014) (cit. on pp. 1, 41).
- [10] X. Meng, H.-N. Wang, S.-Y. Song, and H.-J. Zhang, *Chem. Soc. Rev.* **46**, 464 (2017) (cit. on pp. 1, 41).
- [11] J. Lee, O. K. Farha, J. Roberts, K. A. Scheidt, S. T. Nguyen, and J. T. Hupp, *Chem. Soc. Rev.* **38**, 1450 (2009) (cit. on pp. 1, 41).
- [12] D. Denysenko, M. Grzywa, J. Jelic, K. Reuter, and D. Volkmer, *Angew. Chem. Int. Ed.* **53**, 5832 (2014) (cit. on pp. 1, 41).
- [13] P. Kumar, A. Deep, and K.-H. Kim, *Trends Anal Chem* **73**, 39 (2015) (cit. on p. 1).
- [14] L. E. Kreno, K. Leong, O. K. Farha, M. Allendorf, R. P. Van Duyne, and J. T. Hupp, *Chemical Reviews* **112**, PMID: 22070233, 1105 (2012) (cit. on pp. 1, 41).
- [15] F.-G. Bănică, *Chemical sensors and biosensors: fundamentals and applications* (Wiley, Hoboken, 2012) (cit. on pp. 1, 42).

- [16] S. Takaishi, M. Hosoda, T. Kajiwara, H. Miyasaka, M. Yamashita, Y. Nakanishi, Y. Kitagawa, K. Yamaguchi, A. Kobayashi, and H. Kitagawa, *Inorg. Chem.* **48**, 9048 (2009) (cit. on p. 1).
- [17] Y. Kobayashi, B. Jacobs, M. D. Allendorf, and J. R. Long, *Chem. Mater.* (2010) (cit. on p. 1).
- [18] C. H. Hendon, D. Tiana, and A. Walsh, *Phys. Chem. Chem. Phys.* **14**, 13120 (2012) (cit. on p. 1).
- [19] L. S. Xie, G. Skorupskii, and M. Dincă, *Chemical Reviews*, PMID: 32275412 (Article ASAP) (cit. on pp. 1, 3, 43).
- [20] C. Kittel, *Einführung in die Festkörperphysik*, 15th edition (Wiley, 2014) (cit. on pp. 1, 5, 10).
- [21] J. M. Ziman, *Prinzipien der Festkörpertheorie*, 2nd edition (Verlag Harri Deutsch, Thun Frankfurt am Main, 1992) (cit. on pp. 1, 5, 15, 20, 21, 29–31, 93).
- [22] N. W. Ashcroft and N. D. Mermin, *Solid State Physics* (Saunders College Publishing, 1976) (cit. on pp. 1, 5, 10, 27, 48).
- [23] H. Oberhofer, K. Reuter, and J. Blumberger, *Chem. Rev.* **117**, 10319 (2017) (cit. on pp. 1, 2, 37, 60, 61, 85).
- [24] J. Bardeen and W. Shockley, *Phys. Rev.* **80**, 72 (1950) (cit. on pp. 2, 24, 25, 31, 39, 48, 51, 61).
- [25] F. Giustino, *Rev. Mod. Phys.* **89**, 015003 (2017) (cit. on pp. 2, 50, 73).
- [26] L. Sun, C. H. Hendon, S. S. Park, Y. Tulchinsky, W. Ruomeng, W. Fang, A. Walsh, and M. Dincă, *Chem. Sci.* **8**, 4450 (2017) (cit. on pp. 2, 42, 43, 45, 52, 53, 60, 61, 77).
- [27] C. H. Hendon, A. J. Rieth, M. D. Korzyński, and M. Dincă, *ACS Cent. Sci.* **3**, 554 (2017) (cit. on p. 2).
- [28] A. Szabo and N. S. Ostlund, *Modern Quantum Chemistry – Introduction to Advanced Electronic Structure Theory*, 1st edition (McGraw-Hill, New York, 1989) (cit. on p. 5).
- [29] I. N. Levine, *Quantum chemistry*, 7th edition (Pearson, Boston, 2014) (cit. on pp. 5, 7).
- [30] C. Cohen-Tannoudji, B. Diu, and F. Laloë, *Quantenmechanik – Band 1*, 1st edition (de Gruyter, Berlin, 1997) (cit. on pp. 5, 19, 20).
- [31] F. Jensen, *Introduction to computational chemistry*, 3rd edition (John Wiley & Sons, Ltd, Chichester, 2017) (cit. on pp. 5, 8–10, 89, 91).
- [32] W. Koch and M. C. Holthausen, *A chemist’s guide to density functional theory*, 2nd edition (Wiley, Weinheim, Germany, 2001) (cit. on pp. 5, 7–9, 89).
- [33] U. Roessler, *Solid State Theory: An Introduction*, 2nd edition (Springer, Dordrecht Heidelberg London New York, 2009) (cit. on pp. 5, 15).

- [34] C. Kittel, *Quantum Theory of Solids*, 2nd edition (Wiley, 1987) (cit. on pp. 5, 23, 25).
- [35] S. Elliot, *The Physics and Chemistry of Solids* (Wiley, 2000) (cit. on pp. 5, 21, 37).
- [36] H. Haken, *Quantenfeldtheorie des Festkörpers*, 2nd edition (Teubner, Stuttgart, 1993) (cit. on pp. 5, 30, 31, 36).
- [37] T. Lancaster and S. J. Blundell, *Quantum field theory for the gifted amateur*, 1st edition, corrected reprint (Oxford University Press, Oxford, UK, 2015) (cit. on pp. 5, 19, 20).
- [38] J. M. Ziman, *Electrons and Phonons* (Oxford, 1967) (cit. on p. 5).
- [39] A. Altland and B. Simons, *Condensed Matter Field Theory*, 2nd edition (Cambridge University Press, Cambridge, UK, 2010) (cit. on pp. 5, 29).
- [40] P. M. Chaikin and T. C. Lubensky, *Principles of condensed matter physics*, 7th printing (Cambridge University Press, Cambridge, UK, 2013) (cit. on p. 5).
- [41] E. C. Marino, *Quantum field theory approach to condensed matter physics*, 1st edition (Cambridge University Press, Cambridge, UK, 2017) (cit. on pp. 5, 10).
- [42] F. Schwabl, *Statistische Mechanik*, 2nd edition (Springer, Berlin, 2004) (cit. on pp. 5, 29).
- [43] L. Landau and E. M. Lifshitz, *Theory of Elasticity*, 2nd edition, Course of Theoretical Physics (Pergamon Press, Oxford, U. K., 1970) (cit. on pp. 5, 18).
- [44] M. Born and K. Huang, *Dynamical Theory of Crystal Lattices*, 1st edition (Oxford University Press, Oxford, UK, 1954) (cit. on pp. 5, 6, 17, 18).
- [45] P. Y. Yu and M. Cardona, *Fundamentals of Semiconductors*, 3rd edition (Springer, Berlin Heidelberg Dordrecht London New York, 2005) (cit. on pp. 5, 50, 51).
- [46] C. Jacoboni, *Theory of Electron Transport in Semiconductors*, Springer Series in Solid State Sciences 165 (Springer, Heidelberg, 2010) (cit. on pp. 5, 22, 28, 29, 31, 32, 46, 50, 85).
- [47] A. Jünger, *Transport Equations for Semiconductors*, Lecture Notes in Physics 773 773 (Springer, Berlin Heidelberg, 2009) (cit. on pp. 5, 31).
- [48] R. Maurer, “First-principles description of the isomerization dynamics of surface-adsorbed molecular switches”, PhD thesis (Technische Universität München, 2014) (cit. on pp. 6, 13).
- [49] S. P. Rittmeyer, “Non-adiabatic effects in gas-surface dynamics”, PhD thesis (Technische Universität München, 2017) (cit. on p. 6).
- [50] P. Hohenberg and W. Kohn, Phys. Rev. **136**, B864 (1964) (cit. on p. 7).

- [51] E. Engel and R. M. Dreizler, *Density functional theory*, edited by W. Beiglböck, P. Chrusciel, J.-P. Eckmann, H. Grosse, A. Kupiainen, H. Löwen, M. Loss, N. A. Nekrasov, M. Salmhofer, S. Smirnov, L. Takhtajan, and J. Yngvason, *Theoretical and Mathematical Physics (TMP)* (Springer, Heidelberg Dordrecht London New York, 2011) (cit. on p. 7).
- [52] W. Kohn and L. J. Sham, *Phys. Rev.* **140**, A1133 (1965) (cit. on p. 7).
- [53] J. P. Perdew, K. Burke, and M. Ernzerhof, *Phys. Rev. Lett.* **77**, 3865 (1996) (cit. on pp. 9, 45, 66).
- [54] J. P. Perdew and A. Zunger, *Phys. Rev. B* **23**, 5048 (1981) (cit. on p. 10).
- [55] G. S. Michelitsch, “Ab initio simulation of core-level spectroscopies and correlated materials”, PhD thesis (Technische Universität München, 2019) (cit. on p. 10).
- [56] A. J. Cohen, P. Mori-Sánchez, and W. Yang, *Chem. Rev.* **112**, 289 (2012) (cit. on p. 10).
- [57] N. A. Mecholsky, L. Resca, I. L. Pegg, and M. Fornari, *Phys. Rev. B* **89**, 155131 (2014) (cit. on pp. 22, 23).
- [58] C. Herring and E. Vogt, *Phys. Rev.* **101**, 944 (1956) (cit. on pp. 24, 33, 51).
- [59] F. S. Khan and P. B. Allen, *Phys. Rev. B* **29** (1984) (cit. on p. 24).
- [60] C. Jacoboni and L. Reggiani, *Rev. Mod. Phys.* **55**, 645 (1983) (cit. on p. 31).
- [61] J. L. C. Rowsell and O. M. Yaghi, *Microporous Mesoporous Mat.* **73**, 3 (2004) (cit. on p. 41).
- [62] S. Kitagawa, R. Kitaura, and S.-i. Noro, *Angew. Chem. Int. Ed.* **43**, 2334 (2004) (cit. on p. 41).
- [63] J. R. Long and O. M. Yaghi, *Chem. Soc. Rev.* **38**, 1213 (2009) (cit. on p. 41).
- [64] O. M. Yaghi, *Journal of the American Chemical Society* **138**, PMID: 27934016, 15507 (2016) (cit. on p. 41).
- [65] R. A. Fischer and C. Wöll, *Angew. Chem. Int. Ed.* **48**, 6205 (2009) (cit. on p. 41).
- [66] D. Denysenko, J. Jelic, K. Reuter, and D. Volkmer, *Chem. - Eur. J.* **21**, 8188 (2015) (cit. on p. 41).
- [67] A. A. Kassie, P. Duan, E. T. McClure, K. Schmidt-Rohr, P. M. Woodward, and C. R. Wade, *Inorg. Chem.* **58**, 3227 (2019) (cit. on p. 41).
- [68] M. E. DMello, N. G. Sundaram, A. Singh, A. K. Singh, and S. B. Kalidindi, *Chem. Commun.* **55**, 349 (2019) (cit. on p. 41).
- [69] L. Sun, C. H. Hendon, M. A. Minier, A. Walsh, and M. Dincă, *J. Am. Chem. Soc.* **137**, 6164 (2015) (cit. on p. 43).
- [70] V. Blum, R. Gehrke, F. Hanke, P. Havu, V. Havu, X. Ren, K. Reuter, and M. Scheffler, *Comput. Phys. Commun.* **180**, 2175 (2009) (cit. on pp. 45, 66).

- [71] J. Heyd, G. E. Scuseria, and M. Ernzerhof, *J. Chem. Phys.* **118**, 8207 (2003) (cit. on pp. 45, 66).
- [72] A. V. Krugau, O. A. Vydrov, A. F. Izmaylov, and G. E. Scuseria, *J. Chem. Phys.* **125**, 224106 (2006) (cit. on pp. 45, 66).
- [73] S. van der Walt, S. C. Colbert, and G. Varoquaux, *Comput. Sci. Eng.* **13**, 22 (2011) (cit. on p. 45).
- [74] E. Jones, T. Oliphant, P. Peterson, et al., *SciPy: open source scientific tools for Python*, [Online; accessed 2019-04-18], 2001 (cit. on pp. 45, 47).
- [75] J. D. Hunter, *Comput. Sci. Eng.* **9**, 90 (2007) (cit. on p. 45).
- [76] A. H. Larsen, J. J. Mortensen, J. Blomqvist, I. E. Castelli, R. Christensen, M. Dułak, J. Friis, M. N. Groves, B. Hammer, C. Hargus, E. D. Hermes, P. C. Jennings, P. B. Jensen, J. Kermode, J. R. Kitchin, E. L. Kolsbjerg, J. Kubal, K. Kaasbjerg, S. Lysgaard, J. B. Maronsson, T. Maxson, T. Olsen, L. Pastewka, A. Peterson, C. Rostgaard, J. Schiøtz, O. Schütt, M. Strange, K. S. Thygesen, T. Vegge, L. Vilhelmsen, M. Walter, Z. Zeng, and K. W. Jacobsen, *J. Phys. Condens. Matter* **29**, 273002 (2017) (cit. on p. 45).
- [77] N. Schlömer and coworkers, *Quadpy*, [Online; accessed 2019-04-30] (cit. on p. 45).
- [78] S. P. Ong, W. D. Richards, A. Jain, G. Hautier, M. Kocher, S. Cholia, D. Gunter, V. L. Chevrier, K. A. Persson, and G. Ceder, *Comput. Mater. Sci.* **68**, 314 (2013) (cit. on p. 45).
- [79] M. Grzywa, D. Denysenko, J. Hanss, E.-W. Scheidt, W. Scherer, M. Weil, and D. Volkmer, *Dalton Trans.* **41**, 4239 (2012) (cit. on p. 46).
- [80] P. Z. Moghadam, A. Li, S. B. Wiggin, A. Tao, A. G. P. Maloney, P. A. Wood, S. C. Ward, and D. Fairen-Jimenez, *Chem. Mater.* **29**, 2618 (2017) (cit. on p. 46).
- [81] J. Nocedal and S. J. Wright, *Numerical optimization*, 2nd edition (Springer, 2006) (cit. on pp. 46, 66).
- [82] W. Setyawan and S. Curtarolo, *Comp. Mat. Sc.* **299** (2010) (cit. on p. 46).
- [83] V. Lebedev, *USSR Comput. Math. & Math. Phys.* **16**, 10 (1976) (cit. on p. 47).
- [84] M. de Jong, W. Chen, T. Angsten, A. Jain, R. Notestine, A. Gamst, M. Sluiter, C. Krishna Ande, S. van der Zwaag, J. J. Plata, C. Toher, S. Curtarolo, G. Ceder, K. A. Persson, and M. Asta, *Sci. Data* **2**, 150009 (2015) (cit. on pp. 49, 50, 52, 97, 98).
- [85] A. U. Ortiz, A. Boutin, A. H. Fuchs, and C. F.-X., *Phys. Rev. Lett.* **109**, 195502–1–195502 (2012) (cit. on pp. 50, 56).
- [86] F. Knuth, V. Carbogno C.and Atalla, V. Blum, and M. Scheffler, *Comp. Phys. Commun.* **190**, 33 (2015) (cit. on p. 52).

- [87] C. Kunkel, C. Schober, H. Oberhofer, and K. Reuter, *J. Mol. Model.* **25**, 87 (2019) (cit. on p. 58).
- [88] I. Yavuz, *Phys. Chem. Chem. Phys.* **19**, 25819 (2017) (cit. on p. 60).
- [89] C. Muschiok, A. Reiner, R. Röss-Ohlenroth, A. Kalytta-Mewas, D. Volkmer, A. Wixforth, and H. Oberhofer, (in preparation) (cit. on p. 61).
- [90] D. Ongari, P. G. Boyd, S. Barthel, M. Witman, M. Haranczyk, and B. Smit, *Langmuir* **33**, PMID: 28636815, 14529 (2017) (cit. on pp. 63–65).
- [91] S. Alvarez, *Dalton Trans.* **42**, 8617 (2013) (cit. on p. 65).
- [92] A. Togo and I. Tanaka, *Scr. Mater.* **108**, 1 (2015) (cit. on pp. 66, 85).
- [93] C. Kunkel, F. Viñes, and F. Illas, *Energy Environ. Sci.* **9**, 141 (2016) (cit. on p. 69).
- [94] S. M. Moosavi, P. G. Boyd, L. Sarkisov, and B. Smit, *ACS Central Science* **4**, 832 (2018) (cit. on p. 70).
- [95] C. Hättig, W. Klopper, A. Köhn, and D. P. Tew, *Chem. Rev.* **112**, PMID: 22206503, 4 (2012) (cit. on p. 89).
- [96] I. N. Bronstein, K. A. Semendjajew, G. Musiol, and H. Mühlig, *Taschenbuch der Mathematik*, 7th ed. (Verlag Harri Deutsch, Frankfurt am Main, 2008) (cit. on pp. 99, 100).
- [97] A. Yershova, S. Jain, S. M. LaValle, and J. C. Mitchell, *I. J. Robot. Res.* **29**, 801 (2010) (cit. on p. 100).

List of publications

Publications directly related to this thesis:

- C. Muschielok and H. Oberhofer, *J. Chem. Phys.* **151**, 015102 (2019)
- C. Muschielok, A. Reiner, R. Röss-Ohlenroth, A. Kalytta-Mewas, D. Volkmer, A. Wixforth, and H. Oberhofer, (in preparation)

Publications not directly related to this thesis:

- M. Grzywa, R. Röß-Ohlenroth, C. Muschielok, H. Oberhofer, A. Błachowski, J. Żukrowski, D. Vieweg, H.-A. Krug von Nidda, and D. Volkmer, *Inorg. Chem.* (submitted)

Acknowledgements

Finally, I want to thank all the people who supported and helped me, so that this work was possible at all. First of all, I want to thank my doctoral advisor Harald Oberhofer for his continuing support considering all kinds of problems which arose throughout the time I have been working on this project. Second, I want to thank Karsten Reuter who hosted my work at his group at TUM.

Second, a big thanks to Ruth Mösch and Christoph Scheurer who can perform minor miracles. Who must also not be forgotten are Simon Wengert and Martin Deimel for IT administration and hardware support, you rock! Also a big thank you to my dearest office mates! In average matutinal order: Georg “Mitch” Michelitsch, Sina Stegmaier, David Egger, and Matthias Kick. At some point I had to change into this office from where I often heard loud laughter in the afternoon. I never regretted the decision. Furthermore, I want to thank my fellow “charge transporters” Christian Kunkel and Simiam Ghan for the many questions and discussions. I think I learned quite a bit. All of the group: thank you for the great time at the numerous group workshops all over Europe and other activities like the international food evenings or karaoke!

Also a big thanks to my collaborators in the groups of Dirk Volkmer and Achim Wixforth in Augsburg. The many discussions helped me understand quite a bit about MOFs and that they sometimes work in mysterious ways. A special thanks goes to Richard Röß-Ohlenroth and Alex Reiner.

Last but not least, I want to thank my friends, my family and my relatives who always supported me on this lengthy and arduous adventure. Thank you Vroni for your love and support. When I was burried under work, you simply pulled me up onto another wonderful mountain!